



PONTIFICIA
**UNIVERSIDAD
CATÓLICA**
DEL PERÚ

th
TECHNISCHE UNIVERSITÄT
ILMENAU

FEM simulation of residual stresses of thin films for applications in MEMS

Master Thesis

submitted for the degree of Master of Science in Mechatronics

by

B. Sc. José Carlos Macavilca Román

Supervising Professor at TU Ilmenau: AOR PD Dr.-Ing. Tom Ströhla
Supervising Professor at PUCP: Dr. Francisco Rumiche
Practical Advisors: Dr.-Ing. Rolf Grieseler
PD Dr.-Ing. habil. Valter Böhm

Ilmenau/Lima, May 2017



Zusammenfassung

In MEMS-Sensoren, wie z. B. Resonatoren basierend auf Cantilevern und doppelt gespannten Balken, können innere Spannungen in den Schichten ihre mechanischen Eigenschaften oder Eigenfrequenzen beeinflussen und kann in einigen Fällen die Struktur sogar zerstören. Diese Masterarbeit hat zum Ziel, die innere Spannung in Schichten zu simulieren, die auf einem Substrat abgeschieden wurden. Die Simulationen wurden mit ANSYS Workbench R17.2, eine Finite-Elemente-Methode Software, durchgeführt.

Der Ansatz besteht aus statischen Simulationen mit einer einschichtigen Wafergeometrie, weil es sich um einen ersten Versuch zur Simulation von inneren Spannungen handelt. Mit dem Ziel, diese darzustellen, wurden drei Simulationstypen durchgeführt. Die Simulation Nr. 1 verwendete für die thermischen Belastungen Heiz- und Kühlschnitte auf einem Einquadrantenmodell. Simulation Nr. 2 fügte dem Modell die "birth and death" Technik hinzu, um die Abscheidung der Schicht abzubilden. Außerdem wurde es unter dem geometrischen Modell als flacher achsensymmetrischer Abschnitt, gekrümmter achsensymmetrischer Abschnitt, d.h. mit der Anfangskrümmung des Wafers und einem gekrümmten Quadrantenmodell, aufgeteilt. In Simulation Nr. 3 wurde die Restspannungen durch die Aktivierung des Kontaktes zwischen der Schicht und der Siliziumdioxidschicht, die als Diffusionsbarriere verwendet wurde, abgebildet.

Die Simulationsergebnisse wurden mit den berechneten Werten aus Messungen verglichen, die durch die Methoden der Wafer-Krümmung und der Röntgenbeugung analysiert wurden. Der Vergleich zeigte, dass das gekrümmte Quadrantenmodell erlaubt, Restspannungen und Ablenkungen näher zu den gemessenen zu erhalten. Darüber hinaus erlaubten die gekrümmten achsensymmetrischen Modelle die Verteilung der Restspannungen in den Schichten und dem Substrat visuell abzubilden. So war die "birth and death" Technik eine nützliche Technik, um die Abscheidung der Schicht zu simulieren. Die in dieser Arbeit beschriebenen Überlegungen können als Ausgangsdaten für komplexere Simulationen verwendet werden, die auf echten MEMS-Strukturen basieren.

Abstract

In MEMS sensors, such as resonators based on cantilever and doubly-clamped beams, the presence of residual stresses in the thin films disrupt their mechanical properties or eigenfrequencies and, in some cases, can destroy the structure. This thesis aims to simulate the residual stresses in wafers composed of thin films deposited over a substrate. The simulations were conducted with ANSYS Workbench R17.2, a finite-element-method software.

This work considered static simulations with a single-layer wafer geometry, since it is a first approach to the simulation of residual stresses. With the purpose of achieving that, three simulation types were performed. Simulation 1 applied the thermal loads as heating and cooling steps to a quadrant model. Simulation 2 added the birth and death technique with the purpose of representing the deposition of the thin film. Besides, it was split under the geometric model as flat axisymmetric section, curved axisymmetric section, i.e. with the initial curvature of the wafer, and curved quadrant model. On the other hand, simulation 3 generated the residual stresses by the activation of the contact between the thin film and the silicon dioxide layer, used as diffusive barrier.

The simulation results were compared to calculated values from measurements performed by the methods of wafer curvature and X-ray diffraction. The comparison showed that the curved quadrant model allowed obtaining residual stresses and deflections closer to the calculated ones. In addition, the curved axisymmetric models allowed visualizing the residual stresses distribution in the layers and the substrate. Thus, the birth and death technique was useful to simulate the deposition of the thin film. The considerations described in this work can be used as input data for more complex simulations based on MEMS structures.

Resumen

En sensores tipo MEMS, tales como resonadores basados en vigas en voladizo y vigas doblemente apoyadas, la presencia de esfuerzos residuales en las películas delgadas distorsionan sus propiedades mecánicas o frecuencias propias y, en algunos casos, pueden llegar a destruir la estructura. Esta tesis tiene como objetivo simular los esfuerzos residuales en obleas (wafers) compuestas de películas delgadas depositadas sobre un sustrato. Las simulaciones se realizaron con ANSYS Workbench R17.2, un software basado en el método de elementos finitos.

Debido a que este trabajo es una primera aproximación a la simulación de esfuerzos residuales, se consideraron tres tipos de simulaciones estáticas con una oblea de una sola capa como modelo geométrico. La primera simulación aplicó las cargas térmicas como pasos de calentamiento y enfriamiento a un modelo de cuadrante; es decir, la cuarta parte de la oblea. En cambio, la segunda simulación incluyó la técnica de nacimiento y muerte, disponible en ANSYS, con el fin de representar la deposición de la película delgada. Esta simulación abarcó tres diferentes modelos geométricos: una sección axisimétrica plana, una sección axisimétrica curvada, que incluye la curvatura inicial de la oblea, y un cuadrante curvo, generado por la revolución de la sección anterior. Por otra parte, la tercera simulación generó las tensiones residuales mediante la activación del contacto entre la película delgada y la capa de dióxido de silicio utilizada como barrera difusiva.

Los resultados de la simulación se compararon con valores calculados a partir de mediciones realizadas por los métodos de curvatura de la oblea y difracción de rayos X. La comparación mostró que el modelo geométrico de cuadrante curvo permitió obtener valores de esfuerzos residuales y deflexiones más cercanas a las calculadas. Además, los modelos axisimétricos curvos permitieron visualizar la distribución de los esfuerzos residuales en las capas y el sustrato. De esta manera, la técnica de nacimiento y muerte mostró su utilidad para representar la deposición de la película delgada. Por otro lado, las consideraciones descritas en este trabajo pueden utilizarse como referencia para simulaciones más complejas basadas en estructuras tipo MEMS.

Acknowledgements

First, I would like to thank my family for all the encouraging support and unconditional love. All the time and effort on this work is entirely dedicated to them.

I want to express my gratitude to my supervisor Dr.-Ing. Rolf Grieseler for his availability, useful comments and continuous guide. I also thank Dr.-Ing. Valter Böhm for his valuable recommendations in this thesis. Besides, I appreciate Dr. Rumiche for his willingness to accept this work. Likewise, I thank Dr.-Ing. Tom Ströhla for his academic support to all the Peruvian students.

During the last year in Germany, I spent enjoyable moments with my friends, whom I thank for making this distant country a homeland.

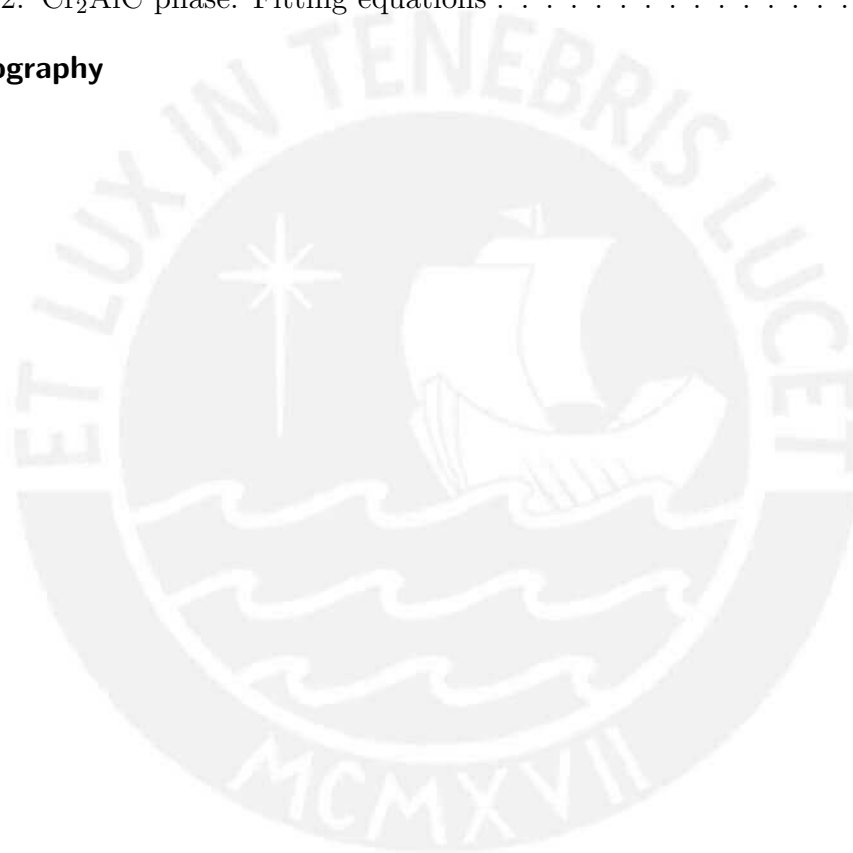
Finally, my deeply thanks to CONCYTEC for granting me a scholarship during this two-year studies.

Contents

List of Tables	x
List of Figures	xi
List of Abbreviation	xviii
1. Introduction	1
1.1. Motivation	1
1.2. Objectives	2
1.3. Overview	2
2. State of the art	4
2.1. MAX phases	4
2.1.1. Crystal structure	4
2.1.2. Elastic properties	5
2.1.3. Mechanical properties	7
2.1.4. Parameters of Cr ₂ AlC phase	8
2.2. Nitride semiconductors	9
2.2.1. Crystal structure	9
2.2.2. Main applications	10
2.2.3. Parameters of aluminum nitride	10
2.3. Microelectromechanical systems	11
2.3.1. Classification	11
2.3.2. Thin films	12
2.3.3. Manufacturing processes	12
2.3.3.1. Photolithography	12
2.3.3.2. Sputtering	13
2.3.3.3. Etching	13
2.3.3.4. Evaporation	14
2.3.3.5. Chemical vapor deposition	14

2.4.	Resonant MEMS	15
2.4.1.	Operational modes	16
2.4.2.	Theory of cantilever and beams	17
2.5.	Residual stress	19
2.5.1.	Residual stress formula	19
2.5.1.1.	Stoney equation	19
2.5.1.2.	Stoney equation for multilayer structures	20
2.5.1.3.	Freund equation	21
2.5.1.4.	Hsueh equation	21
2.5.1.5.	General thermal stress	23
2.5.2.	Residual stress characterization	23
2.5.2.1.	Wafer curvature measurement	23
2.5.2.2.	Nondestructive measurement	23
2.5.2.3.	MEMS structures	25
2.6.	Finite Element Method	26
2.6.1.	Steps of FEM	26
2.6.2.	Software packages	28
3.	Simulation of residual stresses	30
3.1.	MEMS structures	30
3.2.	Preparation processes	31
3.3.	Dimensions of the wafer	32
3.4.	Types of simulation	34
3.5.	Simulation 1 - Static load to quadrant	35
3.5.1.	Mesh	36
3.5.2.	Simulation	38
3.5.3.	Comparison with theoretical stresses	40
3.6.	Simulation 2 - Static load by using birth and death technique	42
3.6.1.	Axisymmetric simulation	44
3.6.1.1.	Mesh	44
3.6.1.2.	Simulation	46
3.6.1.3.	Results	47
3.6.2.	Axisymmetric simulation with initial curvature	51
3.6.2.1.	Mesh	52
3.6.2.2.	Simulation	53
3.6.2.3.	Results	54
3.6.3.	Quadrant simulation with initial curvature	56
3.6.3.1.	Mesh	56
3.6.3.2.	Simulation	57
3.6.3.3.	Results	57
3.7.	Simulation 3 - Detection of the contact between SiO ₂ and thin film	58
3.7.1.	Mesh	60
3.7.2.	Simulation	60
3.7.3.	Results	61
3.8.	Observations	62
3.8.1.	Killing contact	62
3.8.2.	Simulation 3	64

4. Comparison with experimental values	67
4.1. Wafer curvature measurements	67
4.2. XRD measurements	72
4.3. Discussion	73
4.3.1. Residual stresses	73
4.3.2. Deflection of the wafer	74
5. Conclusions and Future Work	77
5.1. Conclusions	77
5.2. Future work	78
A. Aluminum nitride: Scans with altered data	79
B. Fitting equations	81
B.1. Aluminum nitride: Fitting equations	81
B.2. Cr ₂ AlC phase: Fitting equations	84
Bibliography	87



List of Tables

2.1.	Elastic constant in GPa of some MAX phases. Adapted from [10]. . . .	6
2.2.	Mechanical and thermal parameters of Cr_2AlC (TEC is the Thermal Expansion Coefficient).	8
2.3.	Mechanical and thermal parameters of wurtzite AlN.	11
2.4.	Some elements used to discretize. Table extracted from [60].	28
3.1.	Dimensions of the wafer considered in the simulation.	32
3.2.	Mechanical and thermal parameters of anisotropic silicon. Data extracted from Ansys software.	34
3.3.	Meshing parameters of the AlN and Cr_2AlC bilayer quadrants.	38
3.4.	Contact type characteristics available in ANSYS. Table based on [70]. .	38
3.5.	Meshing parameters of the AlN and Cr_2AlC axisymmetric sections. . .	46
3.6.	Meshing parameters of the AlN and Cr_2AlC axisymmetric sections with initial curvature.	53
3.7.	Meshing parameters of the AlN and Cr_2AlC quadrant models with initial curvature.	57
3.8.	Meshing parameters of the AlN circular plate.	60
3.9.	Boundary conditions in Simulation 3: Supports applied step by step. .	60
3.10.	Supports applied step by step.	65
4.1.	Mechanical properties obtained by the Voigt relations.	70

List of Figures

1.1. Effect of the residual stresses on MEMS structures: (a) Disruption of the Young's modulus (ΔE) for different lengths of Cr_2AlC cantilevers, (b) Destroyed thin film due to high residual stresses. Figures extracted from [4].	2
2.1. MAX phases: (a) Location of $\text{M}_{n+1}\text{AX}_n$ elements in periodic table. Figure extracted from [9], (b) MAX hexagonal cell units: (a) 211 ($n = 1$), (b) 312 ($n = 2$), (c) 413 ($n = 3$). Figure extracted from [7].	5
2.2. Strain-stress loops of Ti_2AlC_2 performed with: (a) Porous in 10% volume, (b) Fully dense. Figure extracted from [15].	6
2.3. Formation of kink boundaries: (a) Elliptic subcritical kink bands with dimensions 2α and 2β , (b) Elliptic kink bands with mobile dislocation walls, (c) Typical hysteresis loop caused by the creation and growth during loading and the elimination of IKBs during the unloading (W_d is the dissipated energy per unit volume per cycle), whereas ε_{LE} and ε_{NL} are the linear elastic and nonelastic components of the strain [15]), (d) IKB within a grain (at this stage the IKB is reversible), (e) At higher stresses or temperatures, the IKB can deteriorate and generate mobile dislocation walls (in point marks), (f) Kink bands generated by the formation of mobile dislocation walls (note that the grain size is reduced) [7, 10]. Figure extracted from [7].	7
2.4. Kink formation: Under a compression load, an elastic buckling occur and thus shear forces are generated. In areas, where maximum shears occur, pairs of dislocation walls move in opposite directions until the formation of kink bands and kink boundaries. This cause the typical stovepipe form. Figure extracted from [7].	8
2.5. Thermal properties of Cr_2AlC respect to temperature (T): (a) Heat capacity and (b) Thermal conductivity (λ) (Figures extracted from [21]); (c) TECs α_a and α_c (Figure based on data from [20]).	9

2.6.	Main structures of nitrides and their laterality of the fourth interatomic bond: (a) Wurtzite to the right (R), (b) Zinc blende to the left (L). Figures adapted from [24].	10
2.7.	Variation of the thermal expansion coefficients α_a and α_c of AlN. Figure based on data from [33].	11
2.8.	Basic manufacturing process of micromachining: layers are deposited, then a pattern is applied to the photoresist through lithography, which is used as a guide for the etching process. Figure redrawn from [34]. . .	12
2.9.	Representation of the direct-current diode sputtering method. Figure extracted from [36].	13
2.10.	Etching process according to the attack direction: (a) Isotropic, (b) Anisotropic, (c) Partially anisotropic. Figures redrawn from [36].	13
2.11.	Steps developed during a CVD. Figure redrawn from [36].	14
2.12.	Schematic view of the production by MOCVD of AlGaAs. The organometallic compounds are sent to the reaction chamber, where the deposition occurs. Later, its volatile products are discharged by the H_2 to the exhaust. Figure redrawn from [37].	15
2.13.	Basic mechanical structures of resonant MEMS: (a) Cantilever, (b) Doubly-clamped beam, both figures extracted from [41]; and (c) Diaphragm, figure redrawn from [42].	16
2.14.	Operational modes of resonant MEMS: (a) Dynamic mode, (b) Heat mode, (c) and (d) Static mode under compressive and tensile surface stresses respectively. Figures redrawn from [43].	16
2.15.	Dimensions of the cantilever: (a) Cross section of w and h , (b) Cantilever length is equal to l and is under a distributed load $q(x)$. Redrawn from [45].	17
2.16.	Single thin film on top of a single thick substrate. Note that R is the radius of the sample; t_s , the substrate thickness and f , the residual force per length unit along the interface. Figure redrawn from [53].	20
2.17.	Schematic view of a multilayer system on a substrate. Redrawn from [55].	22
2.18.	Representation of Raman spectroscopy: incident radiation (continuous line) impact on a sample, in this case silicon, and thus, the scattered radiation (dashed-dot line) contains the Raman signal. Figure redrawn from [56].	25
2.19.	Deflection h generated in a thin film window by a pressure p . Parameter a is in this case the radius of the membrane. Figure redrawn from [56].	25
2.20.	Schematic view of a strain gauge structure. Figure redrawn from [56]. .	26
2.21.	Discretization of an element: (a) Continuous element, (b) Discretized element by finite elements, where boundary conditions and loads are applied. Figures extracted from [62].	27
2.22.	Aspect ratio for triangular and rectangular elements: (a) Aspect ratio of 1 and 20 for triangular element, (b) Aspect ratio of 1 and 20 for rectangular element. Figures redrawn from [63].	27
2.23.	Stress distribution, calculated by the FEM, to be analysed by the user. Figure extracted from [62].	29

3.1. Schematic section view of two multilayer deposition of Cr_2AlC : left side with layers of 10 nm, 5 nm and 6 nm of chromium, carbon and aluminum respectively; whereas on the right side with layers of 4 nm, 2 nm and 2 nm of chromium, carbon and aluminum respectively. Figure redrawn from [41].	31
3.2. Dimensions of the doubly-clamped beam structure. l_b represents the beam length and varies from 20 μm to 150 μm [4].	31
3.3. Temperature curve of the preparation processes of AlN and Cr_2AlC films. Data enclosed by the sparse-line rectangles were considered as single steps each one.	32
3.4. Parameters of SiO_2 : (a) Young's module (E) and Poisson's ratio (ν), (b) TEC, (c) Thermal conductivity, (d) Specific heat. Figures based on data from [66].	33
3.5. Thermal expansion coefficient of anisotropic silicon. Figure based on data from ANSYS software.	33
3.6. Types of analysis performed to simulate the residual stresses.	35
3.7. Schematic representation of the quadrant: the wafer (on the left side) where the quadrant solid comes from (on the right side).	35
3.8. Steps of simulation 1 - static load to quadrant.	36
3.9. Simulation 1 - Mesh process: (a) Cyclic symmetric operation applied to the quadrant. Regions Low and High denote the orientation of the revolution respect to the cylindrical coordinate system in the center, (b) Mesh of the quadrant model.	37
3.10. 3D structural element types: (a) SOLID185, (b) SOLID186. Figures extracted from [67].	37
3.11. Boundary conditions of the quadrant: (a) Thermal load applied to the substrate and SiO_2 layer, (b) Circular arc of the substrate (marked in yellow) limited to a zero displacement in y-axis.	39
3.12. Simulation 1 - Equivalent stresses (von Misses) in MPa generated at the deposition temperature: (a) AlN, (b) Cr_2AlC	39
3.13. Simulation 1 - Deformation (in μm) along y axis at the deposition temperature: (a) AlN, (b) Cr_2AlC	40
3.14. Simulation 1 - Deformation (in μm) along x axis at the deposition temperature: (a) AlN, (b) Cr_2AlC	40
3.15. Deformed circular plate characterized by a radius of curvature ρ and deformations δ_x and δ_y . Note that due to their thinner thickness, the thin film and SiO_2 layer were not graphed.	41
3.16. Stresses at the deposition temperature estimated by theoretical formulations and simulations for AlN (in red) and Cr_2AlC (in blue).	41
3.17. Simulation 1 - Equivalent stresses (von Misses) in MPa generated after the cooling process: (a) AlN, (b) Cr_2AlC	42
3.18. Simulation 2 flowchart.	43
3.19. Schematic view of the transversal section: the 3D three-layered wafer (on the left side) where the 2D area comes from (on the right side). Figure based on [74].	44

3.20. Element features available in ANSYS: (a) Plane elements employed in axisymmetric models, (b) Changes in displacement obtained with different interpolation function, note that ξ and η are the centroidal coordinates of the 2D element [75]. Figures of (a) extracted from [67] and of (b) extracted from [75].	45
3.21. Boundary conditions of the axisymmetric section: (a) Left edge fixed in x axis ($u_x = 0$ noted as A) and right vertex fixed in y axis ($u_y = 0$ noted as B), (b) Thermal load applied step by step.	46
3.22. Variation of residual stress with regard to the element size.	46
3.23. Deformation along y axis (in μm) of the AlN axisymmetric model by changing the temperature reference with APDL command.	47
3.24. Deformation along y axis (in μm) of the AlN axisymmetric model by changing the temperature reference with ANSYS Workbench interface.	48
3.25. Deflection scans along the x axis of the AlN wafer after the AlN layer deposition (red marks).	48
3.26. Distribution of equivalent stresses (von Misses) in MPa generated in the AlN axisymmetric model from the left to the right side of the model.	49
3.27. Distribution of normal stresses oriented in x axis in MPa generated in the AlN axisymmetric model from the left to the right side of the model.	49
3.28. Buckling delamination caused by the normal stresses in x axis (σ_{xx}) in the AlN section. Large-scale view to visualize the delamination.	49
3.29. Deformation along y axis (in μm) of the Cr_2AlC axisymmetric model by changing the temperature reference with APDL command.	50
3.30. Distribution of equivalent stresses (von Misses) in MPa generated in the Cr_2AlC axisymmetric model from the left to the right side of the model.	50
3.31. Distribution of normal stresses oriented in x axis in MPa generated in the Cr_2AlC axisymmetric model from the left to the right side of the model.	51
3.32. Buckling delamination caused by the normal stresses in x axis (σ_{xx}) in the Cr_2AlC section. Buckling plotted on a larger scale to visualize it.	51
3.33. Initial deflections of the aluminum nitride (dark cyan line) and Cr_2AlC (orange line) wafers. Data enclosed by the sparse-line rectangle were included to the geometry model.	52
3.34. Mesh of the axisymmetric section with initial curvature: (a) 6-node triangular variant of PLANE183 element type, Figure extracted from [67]; (b) Zoomed view of the triangular elements in the SiO_2 and thin film layers.	53
3.35. Deformation along y axis (in μm) of the AlN axisymmetric model with initial curvature.	54
3.36. Distribution of equivalent stresses (von Misses) in MPa generated in the AlN axisymmetric model, with initial curvature, from the left to the right side of the model.	54
3.37. Distribution of normal stresses oriented in x-axis in MPa generated in the AlN axisymmetric model, with initial curvature, from the left to the right side of the model.	55
3.38. Deformation along y axis (in μm) of the Cr_2AlC axisymmetric model with initial curvature.	55

3.39. Distribution of equivalent stresses (von Misses) in MPa generated in the Cr_2AlC axisymmetric model, with initial curvature, from the left to the right side of the model.	56
3.40. Distribution of normal stresses oriented in x-axis in MPa generated in the Cr_2AlC axisymmetric model, with initial curvature, from the left to the right side of the model.	56
3.41. Simulation 2 - Deformation in y-axis in μm : a) AlN, (b) Cr_2AlC	58
3.42. Simulation 2 - Equivalent stresses (von Misses) in MPa: a) AlN, (b) Cr_2AlC	58
3.43. Schematic representation of the contact detection: (a) At the beginning the bodies, i.e. thin film on the one hand and substrate- SiO_2 (marked in blue) body on the other, are separated, (b) By bringing the thin film together to the other body, the contact is detected because the SiO_2 layer is inside the pinball region (marked in red).	59
3.44. Schematic view of the pinball radius. The contact is activated by the software if the target body is located inside the pinball region. Figure redrawn from [76].	59
3.45. Boundary conditions in Simulation 3: (a) Faces of the bilayer solid fixed on x and z axes, (b) Step-by-step detail.	61
3.46. Simulation 3 results: (a) Deformations along the y-axis, (b) Residual stresses at room temperature.	61
3.47. Simulation 3 - Deformations along the y-axis of the substrate- SiO_2 body. Note that the plot scale was increased to visualize the deformation of the bottom surface.	62
3.48. Residual stresses generated when the contact between the thin film and SiO_2 layer was born. Zoomed view of the delamination zone.	63
3.49. Deformation in y-axis generated when the contact between the thin film and SiO_2 layer was born. Zoomed view of the delamination zone.	63
3.50. Deformation in y-axis: (a) At step 2, i.e. with a non-active contact between SiO_2 and thin film, (b) At step 4.	64
3.51. Deformation along y-axis of the bilayer body after reaching the deposition temperature at 1190°C . Since the support was applied only to the perimeter edge of the bilayer body, a high deformation of $8713.7\mu\text{m}$ was obtained.	64
3.52. Boundary conditions: (a) Faces fixed in the bilayer solid, (b) Temperature curve applied step by step.	65
4.1. Deflection scans of the AlN wafer with only the substrate (Si) layer, after the SiO_2 layer deposition (green marks) and after the AlN layer deposition (red marks): (a) Along the x-axis, (b) Along the z-axis.	67
4.2. Deflection scans of the Cr_2AlC wafer after the SiO_2 deposition (blue marks), after the Cr_2AlC layer deposition (green marks) and after the heat treatment (red marks): (a) Along the x-axis, (b) Along the z-axis.	68
4.3. Deflection scans with wrong data measured on the left and right, enclosed by two meshed rectangles. Data taken after AlN layer deposition: (a) Along x-axis, (b) Along z-axis.	68

4.4.	Data scan along x-axis after the AlN layer deposition (red line) and fourth order fitting polynomial (black dash-line). Polynomial parameters, R-squared and residual sum of squares shown in embedded table.	70
4.5.	Data scan along x-axis after the heat treatment once the Cr ₂ AlC was deposited (red line) and fourth order fitting polynomial (black dash-line). Polynomial parameters, R-squared and residual sum of squares shown in embedded table.	70
4.6.	Residual stress (black marks) and curvature radius (red marks) after each fabrication step for the AlN wafer. Note that the lines are not values, but are connecting lines among values.	71
4.7.	Residual stress (black marks) and curvature radius (blue marks) after each fabrication step for the Cr ₂ AlC wafer. Note that the lines are not values, but are connecting lines among values.	71
4.8.	Measured diffractogram of the AlN wafer. The average residual stress ($\sigma_0 = 714.8$ MPa) is calculated from the measured curve (black marks), Rietveld fitting curve (red marks) and theoretical position (blue marks).	72
4.9.	Measured diffractogram of the Cr ₂ AlC wafer. The average residual stress ($\sigma_0 = 1004.5$ MPa) is calculated from the measured curve (black marks), Rietveld fitting curve (red marks) and theoretical position (blue marks).	72
4.10.	Equivalent residual stresses obtained by simulations (blue and red columns), i.e. Axisymmetric (Axi.), Axisymmetric with initial curvature (Axi. w/-curv), Quadrant with initial curvature (Quad. w/curv) compared with experimental results (pale blue and red columns), i.e. Stoney equation, according to Guo et al. [54], and XRD measurements.	73
4.11.	Deflections in y-axis of the AlN wafers: (a) Measured data, (b) Simulated data.	75
4.12.	Deflections in y-axis of the Cr ₂ AlC wafers: (a) Measured data, (b) Simulated data.	75
5.1.	Variation of the first modal frequency with regard to the doubly-clamped beam lengths. Green marks represent the results for stress-free beams, i.e. without residual stresses, while the red ones show the values for beams with residual stresses. The material of the beams were Cr ₂ AlC.	78
A.1.	Deflection scans with wrong data. Data taken along x axis after AlN layer deposition.	79
A.2.	Deflection scans with wrong data. Data taken along z axis after AlN layer deposition.	80
B.1.	Data scan along x axis on the silicon substrate (blue line) and fourth order fitting polynomial (light blue dash-line). Polynomial parameters, R-squared and residual sum of squares shown in embedded table.	81
B.2.	Data scan along x axis after the SiO ₂ deposition (green line) and fourth order fitting polynomial (light blue dash-line). Polynomial parameters, R-squared and residual sum of squares shown in embedded table.	82

B.3. Data scan along z axis on the silicon substrate (blue line) and fourth order fitting polynomial (light blue dash-line). Polynomial parameters, R-squared and residual sum of squares shown in embedded table.	82
B.4. Data scan along z axis after the SiO ₂ deposition (green line) and fourth order fitting polynomial (light blue dash-line). Polynomial parameters, R-squared and residual sum of squares shown in embedded table.	83
B.5. Data scan along z axis after the AlN deposition (red line) and fourth order fitting polynomial (black dash-line). Polynomial parameters, R-squared and residual sum of squares shown in embedded table.	83
B.6. Data scan along x axis after the SiO ₂ layer (blue line) and fourth order fitting polynomial (light blue dash-line). Polynomial parameters, R-squared and residual sum of squares shown in embedded table.	84
B.7. Data scan along x axis after the Cr ₂ AlC layer deposition (green line) and fourth order fitting polynomial (green blue dash-line). Polynomial parameters, R-squared and residual sum of squares shown in embedded table.	84
B.8. Data scan along z axis after the SiO ₂ layer (blue line) and fourth order fitting polynomial (light blue dash-line). Polynomial parameters, R-squared and residual sum of squares shown in embedded table.	85
B.9. Data scan along z axis after the Cr ₂ AlC layer deposition (green line) and fourth order fitting polynomial (green blue dash-line). Polynomial parameters, R-squared and residual sum of squares shown in embedded table.	85
B.10. Data scan along z axis after the heat treatment once the Cr ₂ AlC layer was deposited (red line) and fourth order fitting polynomial (black dash-line). Polynomial parameters, R-squared and residual sum of squares shown in embedded table.	86

List of Abbreviation

APCVD	Atmospheric-pressure Chemical Vapor Deposition
APDL	Ansys Parametric Design Language
BTP	“Brittle to Plastic” Transition
CVD	Chemical Vapor Deposition
DFT	Density Functional Theory
FEM	Finite Elements Method
FWHM	Full Width at Half Maximum
IKB	Incipient Kink Bands
KB	Kink Bands
LPCVD	Low-Pressure Chemical Vapor Deposition
MAX	$M_{n+1}AX_n$ phase
MEMS	Microelectromechanical Systems
MOCVD	Metal Organic Chemical Vapor Deposition
PECVD	Plasma-Enhanced Chemical Vapor Deposition
PVD	Physical Vapor Deposition
TEC	Thermal Expansion Coefficient
UV	Ultraviolet
XRD	X-ray Diffraction

Introduction

1.1. Motivation

The emergence of Microelectromechanical Systems (MEMS) changed the fabrication and application of products in different fields since it combines microelectronics, mainly based on silicon, and the micromachining technology [1]. Apart from that integration, the relevance of MEMS technology lies on the possibility to employ different materials (as thin films) in order to design components such as pressure sensors, resonator sensors, electro-thermal actuators among others [2]. Typical structures are beams or cantilevers which are used to provide the respective signals to detect e.g. changes in flows or adsorption onto the sensors.

Residual stresses, generated during the fabrication processes, change the properties of microelectromechanical systems drastically, e.g. modify the resonance frequency and the mechanical response [3]. As an example, Figure 1.1a shows the variation of the Young's modulus for different cantilevers lengths made of Cr_2AlC MAX phase, where a no constant value is observed [4]. This behavior occurs due to the influence of the residual stresses generated during the annealing of the material at 600°C especially for shorter length cantilevers ($6\ \mu\text{m}$ to $12\ \mu\text{m}$). Since they have a higher rigidity because of their shorter lengths, the relaxation mechanism of the residual stresses, shown as a bending, is reduced leading to an apparent alteration of Young's modulus. In other cases, the residuals stresses can destroy the MEMS structure (see Figure 1.1b) due to an extreme deformation or microstructural changes [5]. For that reason, the measurement and simulation of residual stresses play a substantive role to determine the effect of the fabrication processes on MEMS structures.

Hence, the aim of this thesis is the simulation of the residual stresses in Cr_2AlC and AlN wafers, materials employed to produce resonant beams and piezoelectric actuators.

In order to achieve that, the geometrical models of the single-film wafers will be generated and thus, the manufacturing processes will be simulated to obtain the residual stresses. The simulations will be done using the Finite Elements Method (FEM) software ANSYS Workbench R17.2 and certain key experiments showing the congruence between simulation and experiment.

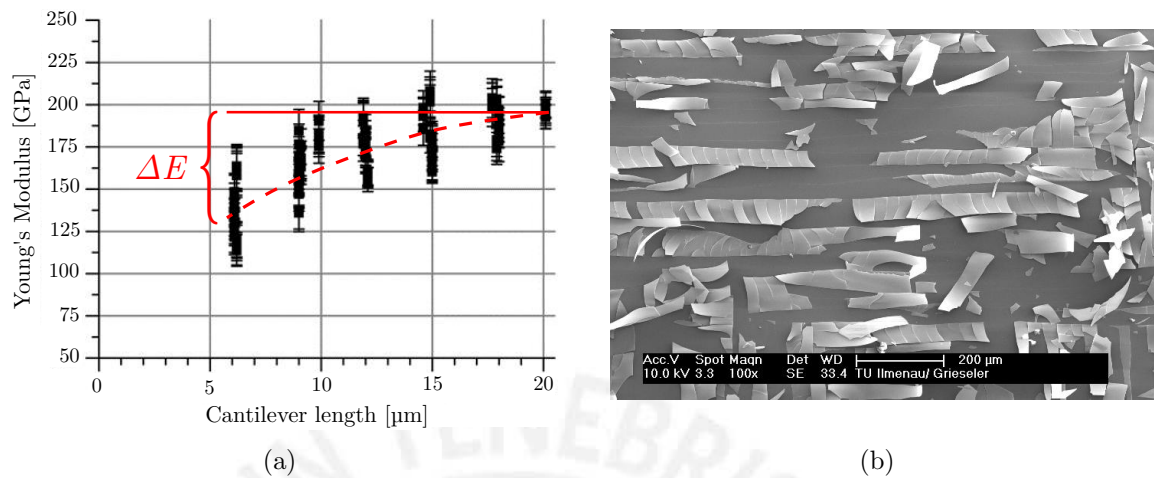


Figure 1.1.: Effect of the residual stresses on MEMS structures: (a) Disruption of the Young's modulus (ΔE) for different lengths of Cr_2AlC cantilevers, (b) Destroyed thin film due to high residual stresses. Figures extracted from [4].

1.2. Objectives

This master thesis has as main objective to simulate the residual stresses using the method of finite elements for Cr_2AlC and AlN thin films for applications in microelectromechanical systems.

Moreover, the secondary objectives are to review the state of the art of MEMS structures, their material parameters and residual stresses equations, to generate the geometrical models of the layered wafers, to apply the thermal loads of the preparation processes to the models and to verify the results of the simulation with experimental data.

1.3. Overview

The content presented in this thesis is organised as follows:

- Chapter 2 details the state of the art of the aluminum nitride and the Cr_2AlC phase, which were the materials of the thin films to be considered in the simulation. Besides, this chapter depicts the main manufacturing processes of MEMS,

an introduction of resonant MEMS as well as formulas and characterization methods of residual stresses. Additionally, it presents a brief description of the method of finite elements.

- Chapter 3 indicates the considerations of the simulations performed in this thesis, describes the features of each one and the results obtained by them. In addition, this chapter displays the observations of the simulations.
- Chapter 4 shows the calculated residual stress from measurements performed by the methods of wafer curvature and X-ray diffraction. Moreover, it compares the simulated with the calculated results.
- Chapter 5 concludes this thesis with a summary of the main results and presents the outlook for possible future work.

Furthermore, Appendices A and B present additional information required by this thesis.



State of the art

2.1. MAX phases

This type of phases, which are carbides or nitrides, have outstanding properties: as other carbides or nitrides, MAX phases have excellent thermal and electrical properties, are elastically stiff with great machinability and resistant to chemical attacks, inter alia [6, 7]. Besides, some MAX phases have low friction coefficient, whereas others, such as Ti_2AlC and Ti_3AlC , show self-healing properties [8]. Hence, MAX phases are used as protective coatings, sensors, electrical contacts, in microelectromechanical structures among others.

2.1.1. Crystal structure

MAX phases receive this designation due to their general formula $\text{M}_{n+1}\text{AX}_n$ ($n = 1, 2$ or 3), where M is an early transition metal; A, an A-group element; whereas X, C or N (see Figure 2.1a) [7]. In Figure 2.1b, the hexagonal MAX unit cells of 211, 312 and 413 phases are shown, where M_6X octahedral interspersed with A layers form the unit cells. Note that the difference between those lies on the quantity of M layers that separate the A layers, i.e. for 211 phases there are two layers; for 312 phases, three and in 413 phases, four [6].

Moreover, 312 and 413 phases have two different M sites, one contiguous to A and other not, which are noted as M_I and M_II respectively (see Figure 2.1b). On the other hand, there are two nonequivalent X sites X_I and X_II in 413 phases. Phases MAX and MX are similar since M_6X octahedral building blocks is the same for both [6].

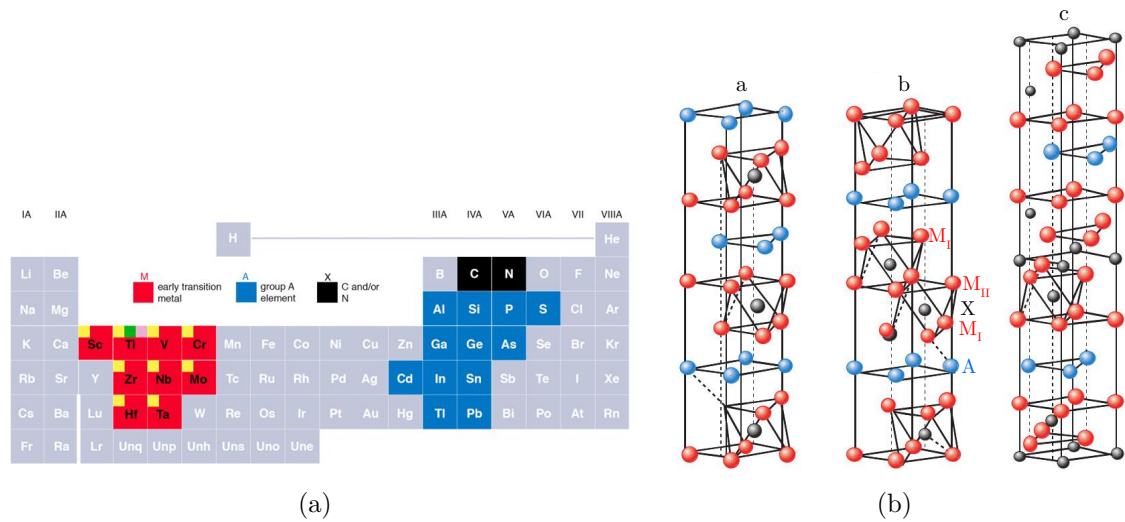


Figure 2.1.: MAX phases: (a) Location of $M_{n+1}AX_n$ elements in periodic table. Figure extracted from [9], (b) MAX hexagonal cell units: (a) 211 ($n = 1$), (b) 312 ($n = 2$), (c) 413 ($n = 3$). Figure extracted from [7].

2.1.2. Elastic properties

Since MAX phases have a hexagonal structure, they have five independent elastic constants (c_{11} , c_{12} , c_{13} , c_{33} and c_{44}) and one dependent elastic constant ($c_{66} = (c_{11} - c_{12}) / 2$) [10,11]. Table 2.1 shows the elastic constants of some MAX phases, which are *ab initio* or Density Functional Theory (DFT) calculations, where the Young's (E_V) and Shear modulus (G_V) and the Poisson's ratio are calculated with the Voigt relations (see Equations 2.1, 2.2 and 2.3) [10].

$$G_V = \frac{1}{15} (2c_{11} + c_{33} - c_{12} - 2c_{13}) + \frac{1}{5} \left(2c_{44} + \frac{1}{2}(c_{11} - c_{12}) \right) \quad (2.1)$$

$$E_V = \frac{9G_V B_V}{3B_V + G_V} \quad (2.2)$$

$$\nu = \frac{3B_v - 2G_v}{2(3B_v + G_v)} \quad (2.3)$$

In Equation 2.2, B_V is the bulk modulus and represents the resistance of a material to hydrostatic pressure [10]. It is calculated with Equation 2.4.

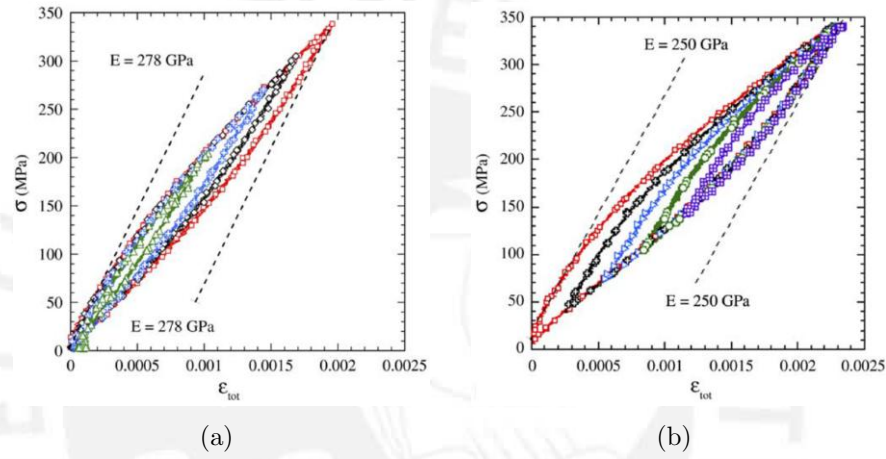
$$B_V = \frac{2}{9} \left(c_{11} + c_{12} + 2c_{13} + \frac{c_{33}}{2} \right) \quad (2.4)$$

Nevertheless, the elastic behavior of MAX phases is nonlinear and hysteretic [7]. This characteristic can be seen in Figure 2.2, where the cyclic compressive stress-strain behavior is graphed for porous in 10% volume (Figure 2.2a) and fully dense Ti_2AlC_2

Table 2.1.: Elastic constant in GPa of some MAX phases. Adapted from [10].

	c_{11}	c_{12}	c_{13}	c_{33}	c_{44}	E_V	G_V	Reference
211 Phases								
Ti ₂ AlN	304	68	91	290	135	288	121	[12]
Mo ₂ GaC	294	98	160	289	127	257	101	[13]
Nb ₂ SnC	286	91	127	288	100	237	93	[11]
Cr ₂ AlC	384	79	107	382	147	351	146	[14]

(Figure 2.2b) [15]. Comparing both graphics, the stress-strain loop of the fully dense Ti₂AlC₂ involves a greater area than that of the 10% volume and thus the fully dense phase dissipates per cycle more energy per unit volume. This outcome is explained by the model of the formation, growth and elimination of Incipient Kink Bands (IKB).

**Figure 2.2.:** Strain-stress loops of Ti₂AlC₂ performed with: (a) Porous in 10% volume, (b) Fully dense. Figure extracted from [15].

The model is based on the investigations made by Frank and Stroh [16]. They considered an elliptic subcritical kink band (KB), whose measurements are 2α and 2β ($\alpha > \beta$) [7]. The formation of the kink boundaries and the interaction of IKB and Kink Bands (KB) are shown in Figure 2.3. The shear stress needed (τ_c) to contribute the spontaneously growth is calculated with Equation 2.5.

$$\tau_c \approx \sqrt{\frac{4G^2 b \gamma_c}{\pi^2 2\alpha} \ln \frac{b}{w \gamma_c}} \quad (2.5)$$

where G is the shear modulus; b , the Burgers vector (it indicates the magnitude and direction of dislocations [17]); w , the dislocation core widths; whereas γ_c , the critical kinking angle obtained with Equation 2.6 [10].

$$\gamma_c = \frac{b}{D} \approx \frac{3\sqrt{3}(1-\nu)\tau_{loc}}{2G} \approx \frac{3\sqrt{3}(1-\nu)}{2 \cdot 8\pi e} \left(\frac{b}{w}\right) \quad (2.6)$$

where ν is the Poisson's ratio; D , the distance between dislocation loops (see Figure 2.3a) and τ_{loc} , the local shear required to nucleate a dislocation pair. Equation 2.5 can be modified by taking into account the remote axial stress (σ_t):

$$\tau_t \approx \frac{\sigma_t}{M} = \sqrt{\frac{4G^2 b \gamma_c}{\pi^2 2\alpha} \ln \frac{b}{w \gamma_c}} \quad (2.7)$$

where M is the Taylor factor that relates τ_t at the single-crystal level to σ_t at the polycrystalline level [10].

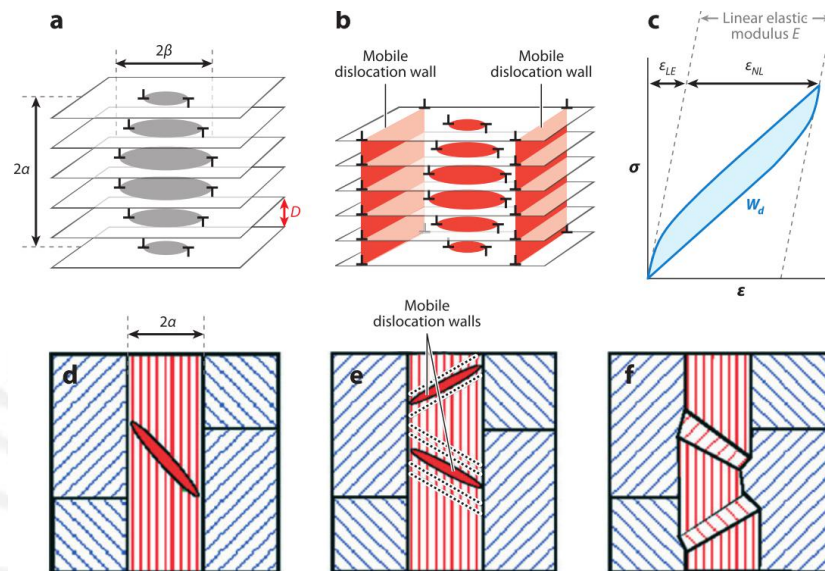


Figure 2.3.: Formation of kink boundaries: (a) Elliptic subcritical kink bands with dimensions 2α and 2β , (b) Elliptic kink bands with mobile dislocation walls, (c) Typical hysteresis loop caused by the creation and growth during loading and the elimination of IKBs during the unloading (W_d is the dissipated energy per unit volume per cycle), whereas ε_{LE} and ε_{NL} are the linear elastic and nonelastic components of the strain [15]), (d) IKB within a grain (at this stage the IKB is reversible), (e) At higher stresses or temperatures, the IKB can deteriorate and generate mobile dislocation walls (in point marks), (f) Kink bands generated by the formation of mobile dislocation walls (note that the grain size is reduced) [7, 10]. Figure extracted from [7].

2.1.3. Mechanical properties

MAX phases tend to have an unequal state of stress when a load is applied on a polycrystalline sample, because these phases lack the five independent slip systems required to ductility and are plastically anisotropic. Therefore, during a loading process, the basal dislocation planes move in favourable oriented or soft grains, which cause the presence of internal stresses [18].

Kink bands play an important role in the mechanical deformation of a MAX phase. As can be seen in Figure 2.4, the formation of kink bands as well as kink boundaries generate the typical stovepipe form. On the other hand, all MAX phases go to a “Brittle to Plastic” Transition (BTP) and unlike other crystal solids, when a MAX phase is exposed to a temperature higher than this transition, the fracture toughness (K_{1C}) decreases [7]. Hereafter, the behavior of MAX phases respect to low and high temperatures will be explained.

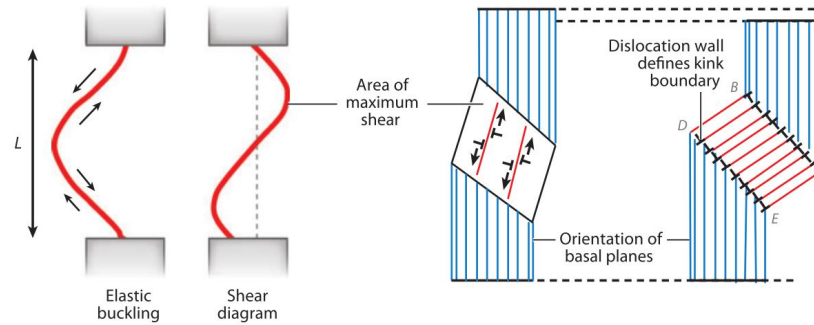


Figure 2.4.: Kink formation: Under a compression load, an elastic buckling occur and thus shear forces are generated. In areas, where maximum shears occur, pairs of dislocation walls move in opposite directions until the formation of kink bands and kink boundaries. This cause the typical stovepipe form. Figure extracted from [7].

2.1.4. Parameters of Cr_2AlC phase

The mechanical and thermal parameters used in next chapter are shown in Table 2.2.

Table 2.2.: Mechanical and thermal parameters of Cr_2AlC (TEC is the Thermal Expansion Coefficient).

	Parameter	Magnitude	Reference
	Density (kg/m^3)	5229	[19]
Elastic constants	c_{11} (GPa)	384	[14]
	c_{12} (GPa)	79	[14]
	c_{13} (GPa)	107	[14]
	c_{33} (GPa)	382	[14]
	c_{44} (GPa)	147	[14]
TEC	α_a, α_c (K^{-1})	see Figure 2.5a	[20]
	Heat capacity ($\text{Jkg}^{-1}\text{K}^{-1}$)	See Figure 2.5b	[21]
	Thermal conductivity ($\text{Wm}^{-1}\text{K}^{-1}$)	See Figure 2.5c	[21]

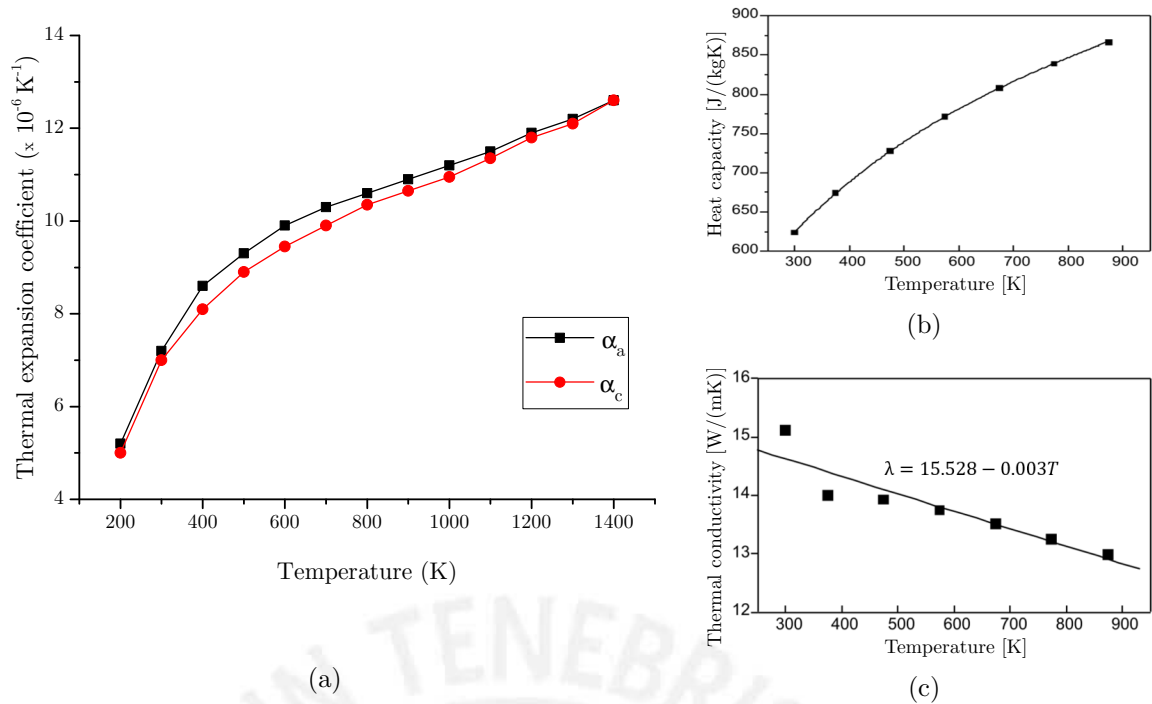


Figure 2.5.: Thermal properties of Cr₂AlC respect to temperature (T): (a) Heat capacity and (b) Thermal conductivity (λ) (Figures extracted from [21]); (c) TECs α_a and α_c (Figure based on data from [20]).

2.2. Nitride semiconductors

Nitride semiconductors such as GaN, InN and AlN have many applications in lighting and displays, e.g. they can be employed as blue, violet and green light emitting devices as well as high temperature transistors [22, 23]. Hereafter, the main characteristics of those nitrides will be explained.

2.2.1. Crystal structure

The crystal structures of group III nitrides are rock salt, wurtzite and zinc blende. Rock salt structure is formed by the application of high pressure because the interionic Coulomb interaction facilitates the formation of ionic bonds over covalent bonds due to the reduction of the lattice parameters [23]. On the other hand, the zinc blende structure has a cubic unit cell characterized by the combination of four group III elements and four nitrogen elements [23]. Alike the previous one, the wurtzite structure has a hexagonal structure with two interpenetrating hexagonal-close-packed sublattices. Figure 2.6 shows the main difference between the wurtzite and zinc blende structures, i.e. the laterality of the fourth interatomic bond: left for the wurtzite, whereas right for the zinc blende [24].

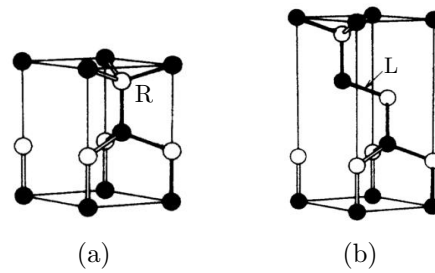


Figure 2.6.: Main structures of nitrides and their laterality of the fourth interatomic bond: (a) Wurtzite to the right (R), (b) Zinc blende to the left (L). Figures adapted from [24].

2.2.2. Main applications

Among the main applications of the AlN are the following [25–28]:

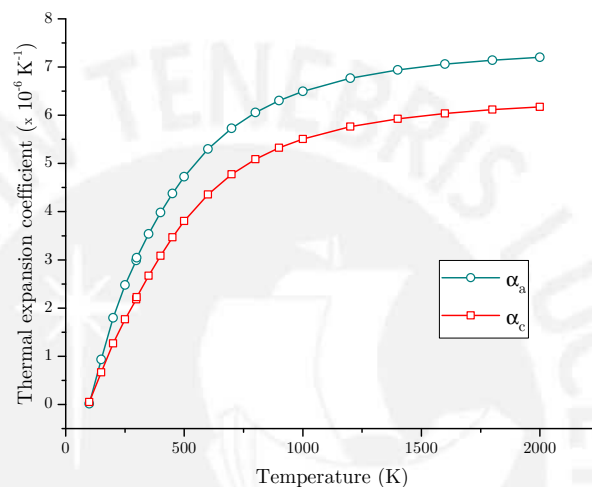
- Surface acoustic wave devices: The AlN is a suitable material for this application owing to its high acoustic velocity (around 6000 m/s to 8000 m/s).
- Ultraviolet (UV) lasers: Due to its band gap (6.2 eV), i.e. the required energy for a valence electron to belong to the conduction band [17], the aluminum nitride can be used as UV laser. Since the energy band gap E_b can be related to the wavelength with the Planck-Einstein relation ($E_b = h_p c_l / \lambda_w$, where h_p is the Planck's constant, c_l is the speed of light and λ_w is the wavelength), the wider the band gap, the shorter the wavelength. Hence, its application lies on the UV region (wavelengths from 10 nm to 400 nm) [29].
- Electronic structures: Given its high thermal conductivity ($285 \text{ Wm}^{-1}\text{K}^{-1}$), as well as, its electrical insulator property ($10^9 \Omega\text{m}$ to $10^{11} \Omega\text{m}$), AlN is used to fabricate this structure type.
- MEMS structures: Since the wurtzite structure of the aluminum nitride has the piezoelectric effect, this material is used to fabricate MEMS structure for sensing applications such as gravimetric or chemical sensors, inter alia.

2.2.3. Parameters of aluminum nitride

The mechanical and thermal parameters considered for the simulation in next chapters are shown in Table 2.3.

Table 2.3.: Mechanical and thermal parameters of wurtzite AlN.

	Parameter	Magnitude	Reference
	Density (kg/m^3)	3260	[30]
Elastic constants	c_{11} (GPa)	345	[31]
	c_{12} (GPa)	125	[31]
	c_{13} (GPa)	120	[31]
	c_{33} (GPa)	395	[31]
	c_{44} (GPa)	118	[31]
TEC	α_a, α_c (K^{-1})	See Figure 2.7	
	Heat capacity ($\text{Jkg}^{-1}\text{K}^{-1}$)	720	[32]
	Thermal conductivity ($\text{Wm}^{-1}\text{K}^{-1}$)	285	[23]

**Figure 2.7.:** Variation of the thermal expansion coefficients α_a and α_c of AlN. Figure based on data from [33].

2.3. Microelectromechanical systems

Abbreviated as MEMS, it is a technology that combines microelectronics, based on silicon, and the micromachining technology in order to build embedded systems, which integrate electrical and mechanical parts [1,34]. Since its emergence, microelectromechanical systems have been used in different areas such as telecommunication, military applications, medicine, among others.

2.3.1. Classification

MEMS elements are used as sensors or actuators. The former convert one type energy into another, which is read posteriorly by the user, and can be divided regarding to the working energy as follows [1]:

- Mechanical: Force, pressure, position, acceleration, speed

- Thermal: Heat, entropy, temperature
- Chemical: Concentration, hydrogenionic potential, entropy, heat
- Electrical: Current, voltage, resistance, capacitance

On the other hand, actuators convert an electrical signal into an action, e.g. a force to move themselves or other elements [1].

2.3.2. Thin films

The term *thin films* involves liquids, gases and solids phases. According to the thickness, they can be separated in three types [35]: ultra thin films (from 5 nm to 10 nm), thin films (from 10 nm to 100 nm) and thicker films (above 100 nm).

2.3.3. Manufacturing processes

Unlike macroscopic manufacturing, such as drilling, turning or milling, MEMS elements are produced by micromachining. It is a batch process, where at least dozens of MEMS elements with dimensions of microns are manufactured simultaneously on the same wafer [34]. The basic manufacturing processes are shown in Figure 2.8.

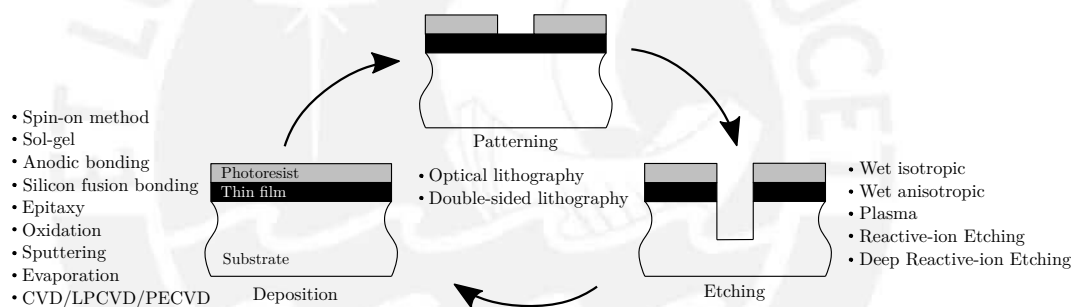


Figure 2.8.: Basic manufacturing process of micromachining: layers are deposited, then a pattern is applied to the photoresist through lithography, which is used as a guide for the etching process. Figure redrawn from [34].

2.3.3.1. Photolithography

This process consists in applying visible light or UV radiation (with wavelengths from 400 nm to 830 nm and from 193 nm to 400 nm respectively) to a photosensitive resist material, known as photoresist, in order to print a pattern [29, 36]. The steps of photolithography are the following: application of the photoresist, exposition of the photoresist to the light source and then the immersion in a developer [34]. It is also divided into subtractive or additive processes: in a subtractive process the photoresist delimits an area on an etching resistant thin film previously applied; whereas in an additive or “lift off” process, the photoresist is removed after thin film deposition and thus, the free areas stay with the film [36].

2.3.3.2. Sputtering

It is a deposition process where ions are accelerated to bombard a surface in order to eject its surface atoms. A representation of this method is shown in Figure 2.9.

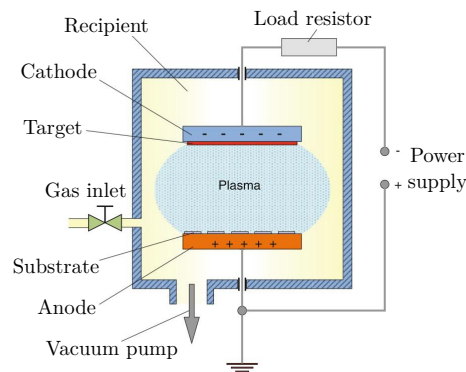


Figure 2.9.: Representation of the direct-current diode sputtering method. Figure extracted from [36].

This process involves other methods as follows [37, 38]:

- Diode Sputtering: The material is transported from the target to a substrate by using a sheet of the material to be deposited on a cathode.
- Reactive Sputtering: It is the sputtering process under reactive gasses.
- Magnetron Sputtering: In this method, a magnetic field is used to increase the time of flight of the electrons in the plasma, which increases the probability of ionization of the gas molecules rising the sputtering rate.

2.3.3.3. Etching

An etching process is the material removal of the surface by the application of liquid or gaseous etchants (aggressive compounds). Respect to the aggregate state of the etchants, the etching process is classified as wet-chemical etching or dry etching when etchant is liquid and gas respectively.

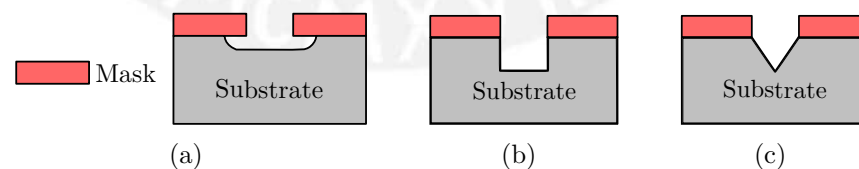


Figure 2.10.: Etching process according to the attack direction: (a) Isotropic, (b) Anisotropic, (c) Partially anisotropic. Figures redrawn from [36].

The direction of the etching process is other classification criteria (see Figure 2.10): isotropic etching refers to an attack in all directions whereas an anisotropic etching follows the crystal direction of a single crystal material.

It is performed after the generation of the pattern by the photolithography. Furthermore, etching processes are used to prepare MEMS structures. For example, anisotropic chlorine plasma etching, wet etching and isotropic etching were applied for the preparation of Cr_2AlC doubly-clamped beams and cantilevers, once the thin film of Cr_2AlC was deposited on the substrate wafer [4].

2.3.3.4. Evaporation

Also known as Physical Vapor Deposition (PVD), it involves heating a material to generate vapor, which condenses on the substrate surface in order to create a film. With the aim of avoiding to contaminate the vapor, this process is performed in a vacuum chamber at pressures below 10^{-4} Pa.

2.3.3.5. Chemical vapor deposition

Abbreviated as CVD, this process is carried out inside a reactor, where the deposition of the material on the substrate occurs due to a chemical reaction. The steps (see Figure 2.11) corresponding to this process are the following [34, 36]:

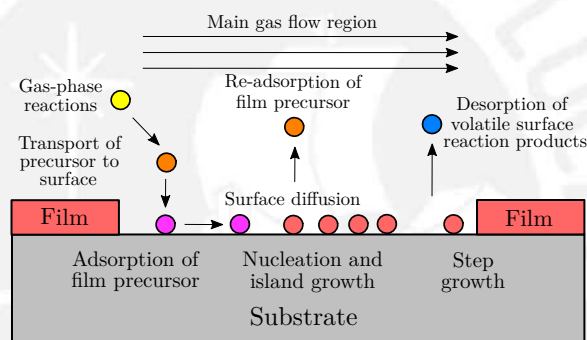


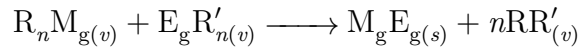
Figure 2.11.: Steps developed during a CVD. Figure redrawn from [36].

- Transport of the reactants in the main gas flow to the reaction zone.
- Gas-phase reactions generate new reactants as well as by-products, which travel to the surface by diffusion.
- Chemical and physical adsorption of the species occurs on the substrate surface. These species sweep the surface by diffusion.
- Nucleation and island growth of the film.
- Desorption of volatile by-products and then convective or diffusive transport of by-products.

This process is performed at high temperatures (above $300\text{ }^{\circ}\text{C}$). CVD is categorized as Atmospheric-pressure Chemical Vapor Deposition (APCVD), Low-Pressure Chemical Vapor Deposition (LPCVD), Metal Organic Chemical Vapor Deposition (MOCVD) or Plasma-Enhanced Chemical Vapor Deposition (PECVD) [34].

- **MOCVD:**

This process is commonly used for the deposition of III-V semiconductors, e.g. AlN, GaN, GaAs, among others, to fabricate optoelectronic devices. In this case, the chemical reaction occurs by the interaction of metalorganic compounds [37]. This reaction can be simplified, i.e. disregarding possible intermediate steps, as follows:



where R and R' are organic radicals, M_g is a II-III group metal, E_g is a V-VI group element (see Figure 2.1a), n is the stoichiometric coefficient, while the subscripts v and s indicate the substance phase: vapor or solid, respectively. As a result, the compound $M_g E_{g(s)}$ is deposited on the substrate, whereas the volatile products $R R'_{(v)}$ are discharged to the exhaust. Figure 2.12 depicts a schematic representation of the MOCVD.

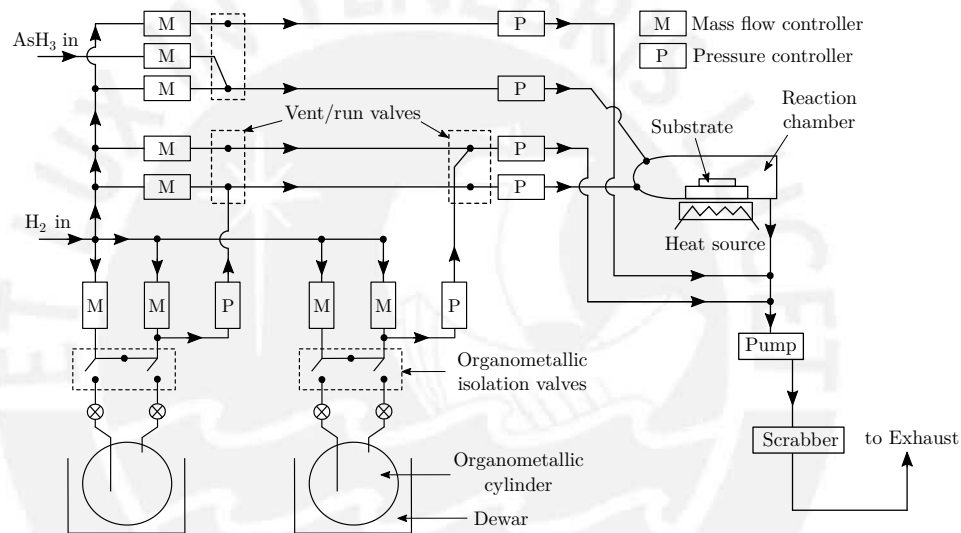


Figure 2.12.: Schematic view of the production by MOCVD of AlGaAs. The organometallic compounds are sent to the reaction chamber, where the deposition occurs. Later, its volatile products are discharged by the H_2 to the exhaust. Figure redrawn from [37].

2.4. Resonant MEMS

This type of sensor, known as μ -resonators, belongs to the mechanical resonance sensors on a micro or nano scale, which change their oscillating characteristics, e.g. resonance frequency, vibration amplitude, quality factor, inter alia, with respect to the measured variable. Among the applications of μ -resonators are mass sensors used in biomedical and chemical applications, pressure sensors, gyroscopes and strain sensors [39, 40]. The basic mechanical structures are the cantilever, the double-clamped beam and

the diaphragm (see Figure 2.13). Hereafter, the operational modes and fundamental formulations of resonant MEMS will be explained.

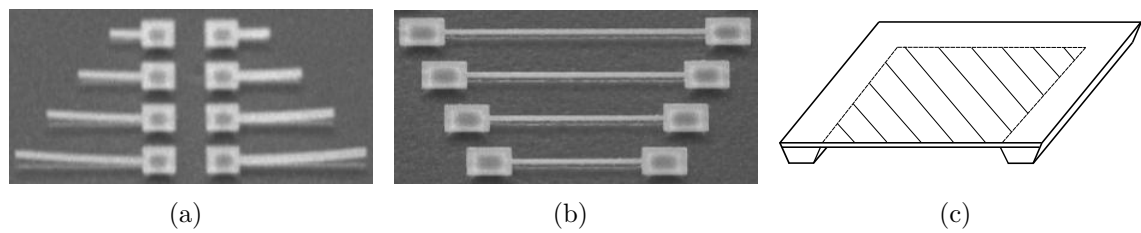


Figure 2.13.: Basic mechanical structures of resonant MEMS: (a) Cantilever, (b) Doubly-clamped beam, both figures extracted from [41]; and (c) Diaphragm, figure redrawn from [42].

2.4.1. Operational modes

The operational modes of resonant sensors are dynamic, heat mode and static [43] (see Figure 2.14).

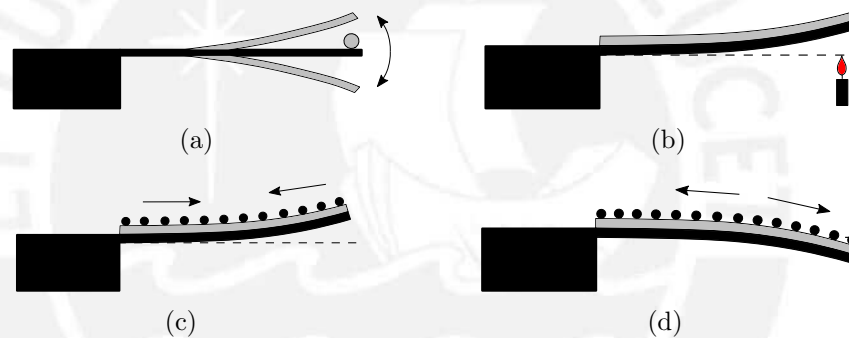


Figure 2.14.: Operational modes of resonant MEMS: (a) Dynamic mode, (b) Heat mode, (c) and (d) Static mode under compressive and tensile surface stresses respectively. Figures redrawn from [43].

- **Dynamic mode**

In this mode, the resonance frequency is measured, which varies according to an increased cantilever or bridge mass [40]. The behavior of a cantilever can be approximated as a harmonic oscillator, i.e. an ideal undamped spring-mass system [43], by the following equation:

$$f = \frac{1}{2\pi} \sqrt{\frac{k}{m}} \quad (2.8)$$

where f is the resonance frequency, k is the spring constant and m is the mass of the resonator. According to Equation (2.8), the resonance frequency increases when the mass of the resonator rises, i.e. if a mass is added to the cantilever [43].

- **Heat mode**

This mode works with a bimetallic resonant structure, which bends, due to the difference between the coefficient of thermal expansion, when is exposed to a heating process (see Figure 2.8b) [43]. Therefore, this type of sensors is used to detect a temperature variation.

- **Static mode**

Unlike the previous modes, the deflection of the resonator is measured, which is caused by stresses originated on a surface [40]. This surface stresses can be compressive (see Figure 2.13c) or tensile (see Figure 2.13d).

2.4.2. Theory of cantilever and beams

Different theories were developed with the purpose to describe the mechanical behavior of a cantilever, being the theory formulated by Euler-Bernoulli one of the most useful [40]. Hereafter, the theory presented will consider a rectangular cross section cantilever of dimensions w , h and l as shown in Figure 2.15. The Euler-Bernoulli theory is based on three main assumptions regarding the cross section [44]: it is infinitely rigid in its own plane, remains plane after the deformation and stays normal to the neutral axis.

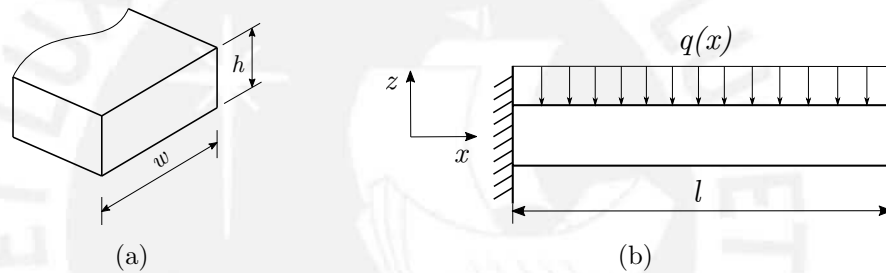


Figure 2.15.: Dimensions of the cantilever: (a) Cross section of w and h , (b) Cantilever length is equal to l and is under a distributed load $q(x)$. Redrawn from [45].

Initially, the cantilever is studied under a distributed load $q(x)$ that represents the effect of the gravity [45]. The force $F(x)$ and moment $M(x)$ originated by $q(x)$ are calculated as follows:

$$\frac{dF(x)}{dx} = q(x) \quad (2.9)$$

$$\frac{d^2M(x)}{dx^2} = q(x) \quad (2.10)$$

The relation between small deflections $u(x)$ and the moment $M(x)$ is the following:

$$M(x) = \frac{1}{EI} \frac{\partial^2 u(x)}{\partial x^2} \quad (2.11)$$

where E is Young's module of the cantilever and I is equal to the second moment of area in respect to the y axis [45]. Note that in a dynamic case the variables also depend on the time t . By applying the Euler-Lagrange equations, the Euler-Bernoulli equation of cantilever is obtained and is equal to

$$EI \frac{\partial^4 u(x, t)}{\partial x^4} + \rho A \frac{\partial^2 u(x, t)}{\partial t^2} - q(x, t) = 0 \quad (2.12)$$

where A is the cross section area and ρ is the beam density [45]. The solution of Equation (2.12) is obtained by considering a negligible effect of $q(x)$ and change of variable of the deflection into $\hat{u}(x)$ (a more detailed solution can be seen in [46]), which is calculated as follows:

$$\hat{u}(x) = A_1 \cosh(\beta_n x) + A_2 \sinh(\beta_n x) + A_3 \cosh(\beta_n x) + A_4 \sinh(\beta_n x) \quad (2.13)$$

where A_1, A_2, A_3 and A_4 are constants that will be calculated with the boundary conditions and the normalized eigenvalue β_n is calculated considering the radial frequency ω_n by the following Equation:

$$\beta_n = \left(\omega_n^2 \frac{\rho A}{EI} \right)^{\frac{1}{4}}, \quad n = 1, 2, \dots \quad (2.14)$$

where n counts the mode number [47].

The radial frequency and thus the eigenfrequencies of the cantilevers and beams, noted as $f_{n,c}$ and $f_{n,b}$ respectively, are obtained by considering the following boundary conditions: the displacement and the angle formed between the cantilever elastic curve and the horizontal equal to zero at $x = 0$ for the cantilever; whereas for the beam at $x = 0$ and $x = l_b$. This yields to

$$f_{n,c} = \frac{\kappa_{n,c}^2}{2\pi l_c^2} \sqrt{\frac{EI}{\rho A}} \quad (2.15)$$

where $\kappa_{n,c} = l_c \beta_{n,c}$ is the eigenvalue [45]. For an ideal cantilever, $\kappa_{n,c} = 1.875, 4.694, 7.855, \pi(n - 1/2)$ for $n = 1, 2, 3, \geq 4$ [45]. Bouwstra and Geijselaers [46] solved the Equation (2.13) and obtained the eigenfrequency for a double-clamped beam:

$$f_{n,b} = \frac{\kappa_{n,b}^2}{2\pi l_b^2} \sqrt{\frac{EI}{\rho A}} \sqrt{1 + \gamma_{n,b}(\varepsilon_b) \frac{l_b^2}{h_b^2} \varepsilon_b} \quad (2.16)$$

where $\kappa_{n,b} = 4.73, 7.85, \dots, (n + 1/2)\pi$ is the eigenvalue of the beam, $\gamma_{n,b}$ is the strain dependent eigenvalue and ε_b is the residual strain [46, 47]. Brückner et al. [47] stated that considering $\gamma_{n,b}$ constant and equals to 0.2949, 0.1453, ..., $12(\kappa_{n,b} - 2)/\kappa_{n,b}$ lead to an error below 0.5% for the fundamental mode. However, this consideration only applies for weakly strained or very short beams, i.e. whether $\gamma_{n,b}(\varepsilon_b)c/12 \ll 1$ where $c = 12\varepsilon_b l_b^2/h_b^2$ [47]. On the other hand, for highly strained long and thin beams, this

assumption leads to an error of 12% for the fundamental mode. The residual strain can be calculated by Equations (2.15) and (2.16) as follows:

$$\varepsilon_b = \left(\left(\frac{f_{n,b}}{f_{n,c}} \right)^2 \left(\frac{\kappa_{n,c} l_b}{\kappa_{n,b} l_c} \right)^4 - 1 \right) \frac{h_b^2}{\gamma_{n,b}(\varepsilon_b) l_b^2} \quad (2.17)$$

2.5. Residual stress

Residual stress (σ_R) is defined as the remaining stress in a material, in a lack of external forces as well as temperature gradients, after manufacturing processes [48]. Likewise, residual stress is composed by three components such as thermal (σ_T), intrinsic (σ_I) and quenching (σ_Q) stresses [49], see Equation 2.18. The first one is caused by the mismatch of the coefficient of thermal expansion between the thin films and the substrate; the second one, by lattice mismatch, chemical reaction, strain misfits during phase transformation, deposition temperature, etc. and the third one, by rapid contraction of the sprayed splats from a high processing temperature to substrate temperature [49–52].

$$\sigma_R = \sigma_T + \sigma_I + \sigma_Q \quad (2.18)$$

The residual stress description will be presented in the next subsection. Since the origin of the quenching and intrinsic stresses lays on the atomic interaction between substrate and film, the equations will refer to the thermal stress.

2.5.1. Residual stress formula

2.5.1.1. Stoney equation

It considers the case of a single thin film over a single substrate. A representation of this joint is shown in Figure 2.16.

This equation is applicable under the following conditions [50, 53]:

- Film and substrate thicknesses are small compared to the width dimension.
- The film thickness (t_f) is uniform and is lower than substrate thickness (t_s), i.e. $t_f \ll t_s$.
- The film material is isotropic, whereas the substrate material is homogeneous, isotropic and linearly elastic.
- The substrate and film adhere perfectly.
- Invariant physical quantities respect to a position change parallel to the interface.

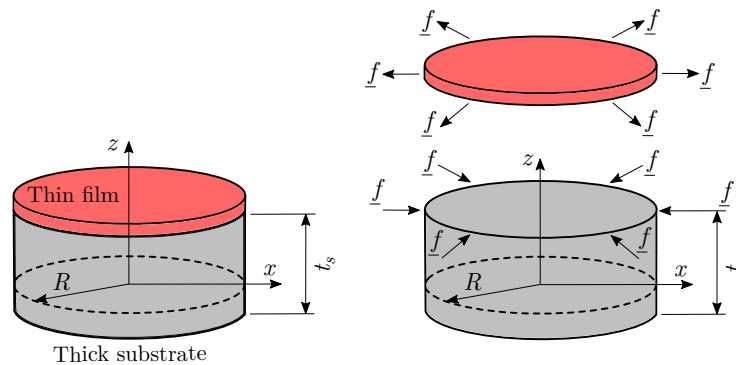


Figure 2.16.: Single thin film on top of a single thick substrate. Note that R is the radius of the sample; t_s , the substrate thickness and \underline{f} , the residual force per length unit along the interface. Figure redrawn from [53].

Due to the presence of the residual stresses, the sample bends and the substrate curvature (κ) is determined as follows

$$\kappa = \frac{6\underline{f}}{E_s^* t_s^2} \quad (2.19)$$

where \underline{f} is the residual force per length unit along the interface between the substrate and thin film, E_s^* represents the biaxial module of the substrate equals to $E_s^* = E_s / (1 - \nu_s)$ (E_s and ν_s are the Young's module and Poisson's ratio of the substrate respectively). considering the curvature and the film thickness (t_f), the film stress is obtained by Equation 2.20 [53].

$$\sigma_f = \frac{\underline{f}}{t_f} \quad (2.20)$$

Using Equations (2.19) and (2.20) yields to

$$\sigma_f = \frac{\kappa E_s^* t_s^2}{6t_f} = \frac{E_s^* t_s^2}{6t_f \rho} \quad (2.21)$$

where the curvature (κ) is equal to the inverse of the radius of curvature (ρ) [53]. Nevertheless, the application of this equation is limited because of the assumptions taken to develop it.

2.5.1.2. Stoney equation for multilayer structures

Guo et al. [54] studied the residual stresses in multilayer structures by applying the Stoney equation considering the radius of curvature variation before and after a monolayer deposition. For the case of a bilayer deposition, i.e. two monolayers A and B, on a substrate, the residual stresses σ_A and σ_B of each monolayer is estimated using Equation 2.21 as follows:

$$\sigma_A = \frac{E_s^* t_s^2}{6t_A} \left(\frac{1}{\rho_A} - \frac{1}{\rho_0} \right) \quad (2.22)$$

$$\sigma_B = \frac{E_s^* t_s^2}{6t_B} \left(\frac{1}{\rho_B} - \frac{1}{\rho_A} \right) \quad (2.23)$$

where t_A and t_B are the thickness of the monolayer, whereas ρ_0 , ρ_A and ρ_B are the radii of curvature of the substrate, monolayer A and monolayer B respectively. Note that each radius of curvature is measured after the deposition of the corresponding layer. The assumptions considered by Guo et al. [54] were the following:

- Young's modulus and Poisson's ratio of the films are equal to that of the substrate.
- Absence of cracks or delamination in the system.
- Substrate deformation is in the elastic range.

2.5.1.3. Freund equation

Unlike the Stoney equation shown before (Equation 2.21), this equation takes into account the film thickness (t_f) on the substrate curvature. Therefore, the curvature (κ) is obtained with Equation (2.24), where E_f^* is the biaxial elastic module of the film equals to $E_f/(1 + \nu_f)$; whereas ν_f and E_f are the Poisson's ratio and Young's module of the thin film [53].

$$\kappa = \frac{6f}{E_s^* t_s^2} \left(1 + \frac{t_f}{t_s} \right) \left[1 + 4 \frac{t_f E_f^*}{t_s E_s^*} + 6 \frac{t_f^2 E_f^*}{t_s^2 E_s^*} + 4 \frac{t_f^3 E_f^*}{t_s^3 E_s^*} + \frac{t_f^4 E_f^*}{t_s^4 E_s^*} \right]^{-1} \quad (2.24)$$

Combining Equations (2.20) and (2.24), the film stress is obtained as follows

$$\sigma_f = \frac{E_s^* t_s^2}{6t_f \rho} \left(1 + \frac{t_f}{t_s} \right)^{-1} \left[1 + 4 \frac{t_f E_f^*}{t_s E_s^*} + 6 \frac{t_f^2 E_f^*}{t_s^2 E_s^*} + 4 \frac{t_f^3 E_f^*}{t_s^3 E_s^*} + \frac{t_f^4 E_f^*}{t_s^4 E_s^*} \right] \quad (2.25)$$

2.5.1.4. Hsueh equation

Unlike previous equations, Hsueh [55] studied the residual stress presented in a multilayer system. Figure 2.17 shows a multilayer system consisting of n layers, each one with a thickness t_i (i from 1 to n), on a substrate with a thickness t_s to produce the multilayer structure. On the right side, it shows the z coordinate system ($z = h_i$) calculated with Equation 2.26.

$$h_i = \sum_{j=1}^i t_j \quad (\text{for } i = 1 \text{ to } n) \quad (2.26)$$

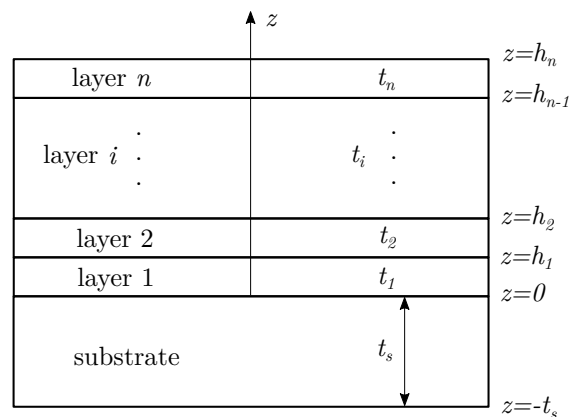


Figure 2.17.: Schematic view of a multilayer system on a substrate. Redrawn from [55].

After the deposition processes, the system is cooled to room temperature (ΔT) where the system bends due to a mismatch of TEC (α_s for the substrate and α_i for each layer) between the layers and the substrate [55]. The strain (ε) produced by bending has a uniform component (c) and a bending component as follows

$$\varepsilon = c + \frac{z - t_b}{\rho} \quad (\text{for } -t_s \leq z \leq h_n) \quad (2.27)$$

where t_b is the location of the bending axis. After applying equilibrium equations, i.e. the resulting force due to the bending strain component and to the uniform strain component are zero [55] as well as the bending moments respect to the bending axis are in equilibrium, the components c and t_b are calculated with Equations (2.28) and (2.29), whereas ρ with Equation (2.30) [55].

$$c = \alpha_s \Delta T + \sum_{i=1}^n \frac{E_i t_i (\alpha_i - \alpha_s) \Delta T}{E_s t_s} \quad (2.28)$$

$$t_b = \frac{t_s}{2} \left(1 - \sum_{i=1}^n \frac{E_i t_i}{E_s t_s} \right) \quad (2.29)$$

$$\frac{1}{\rho} = 6 \sum_{i=1}^n \frac{E_i t_i (\alpha_i - \alpha_s) \Delta T}{E_s t_s^2} \quad (2.30)$$

The residual stresses in the films (σ_i) and in the substrate (σ_s) can be calculated as follows

$$\sigma_i = E_i (\varepsilon - \alpha_i \Delta T) \quad (\text{for } i = 1 \text{ to } n) \quad (2.31)$$

$$\sigma_s = E_s (\varepsilon - \alpha_s \Delta T) \quad (\text{for } -t_s \leq z \leq 0) \quad (2.32)$$

Replacing Equations (2.28), (2.29) and (2.30) in (2.31) and (2.32) yields to

$$\sigma_s = \frac{E_s}{3\rho} (3z + 2t_s) - \frac{2}{3\rho} \sum_{i=1}^n E_i t_i \quad (2.33)$$

$$\sigma_i = -\frac{E_s t_s^2}{6t_i \rho_i} + \frac{2E_i t_s}{3\rho} \quad (2.34)$$

where ρ_i is equal to

$$\frac{1}{\rho_i} = \frac{6E_i t_i (\alpha_i - \alpha_s) \Delta T}{E_s t_s^2} \quad (2.35)$$

2.5.1.5. General thermal stress

The stress generated by the mismatch of TEC between the thin film and substrate during the deposition of the thin film can be estimated by Equation 2.36 as follows [53]:

$$\sigma_{th} = \frac{E_f}{1 + \nu_f} (\alpha_{s_d} - \alpha_f) \Delta T \quad (2.36)$$

where α_{s_d} is the TEC of the substrate at deposition temperature and α_f is the TEC of the thin film at room temperature.

2.5.2. Residual stress characterization

The most used characterization techniques are the following [56]:

2.5.2.1. Wafer curvature measurement

This method is based on the measurement of the wafer bending due to the residual stress. Once this parameter is obtained, the radius of curvature is estimated and thus, the residual stress is calculated with the suitable equation, e.g. Stoney's and others (see subsection 2.5.1).

2.5.2.2. Nondestructive measurement

It uses X-ray Diffraction (XRD) technique, Raman spectroscopy, inter alia.

- **XRD technique**

It is a method used to measure the residual stress in crystalline films in order to get the distance between adjacent crystallographic planes (d_{hkl}), which is calculated by the Bragg's law as follows [48].

$$d_{hkl} = \frac{n\lambda_x}{2\sin\theta} \quad (2.37)$$

Where λ_x is the X-ray wavelength, θ is the angle of incidence and reflection whereas $n = 1$ because the measurement is based on the first-order reflected beam [48]. Therefore, the residual stress σ_m is estimated with Equation (2.38) for isotropic materials.

$$\sigma_m = -\frac{E_f}{2\nu_f} \left(\frac{d_{hkl} - d_0}{d_0} \right) \quad (2.38)$$

Where ν_f is the Poisson's ratio of the film, d_0 is the normal spacing between atoms [48]. For anisotropic materials, the previous equation is modified as follows [48]:

$$\sigma_m = -\frac{c_{11}}{2c_{12}} \left(\frac{d_{001} - d_0}{d_0} \right) \left(c_{11} + c_{12} - \frac{2c_{12}^2}{c_{11}} \right) \quad (2.39)$$

where d_{001} is the distance between adjacent crystallographic planes for an anisotropic material [48].

On the other hand, the residual stresses can be classified as macro-, micro- and nano-stresses. The first one, noted as stress type I, is a homogeneous stress within body and thus, can be estimated with the wafer curvature measurement [57]. The stresses at macro-scale (type II) refer to a grain-size level, whereas the nano-stresses (type III) are generated inside a grain due to the presence of crystalline defects. Types II and III impact on lattice strains and can be estimated by nondestructive techniques. For example, the Transmission Electron Microscopy is used to measure stress type III, while the XRD technique can be used to measure a sum of the types I and II because both stresses impact similarly on the diffraction profile. As a result of applying the XRD, the average strain ε_0 can be calculated as follows [57–59]:

$$\varepsilon_0 = \frac{\beta}{4\tan\theta} \quad (2.40)$$

where β is the Full Width at Half Maximum (FWHM). Once the strain is obtained, the average residual stress (σ_0) can be calculated.

- **Raman spectroscopy**

This technique is depicted in Figure 2.18, where a laser is applied to a sample through a lens in order to focus the signal in a spot. As a result of the irradiation, the laser light is scattered and contains the Raman signals, which are collected and read by a spectrometer as a frequency function [56]. Therefore, the Raman spectrum is calculated as a frequency shift as follows:

$$\Delta\omega = \frac{1}{\lambda_i} - \frac{1}{\lambda_s} \quad (2.41)$$

where λ_i and λ_s are the wavelength of the incident and scattered radiation respectively. The residual stress can be estimated using the phonon deformation potentials of Anastassakis ($\sigma_R \cong -434\Delta\omega$) or Chandrasekhar ($\sigma_R \cong -518\Delta\omega$) [56].

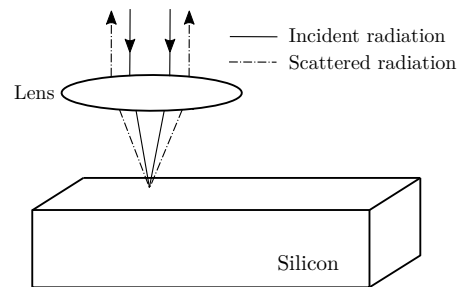


Figure 2.18.: Representation of Raman spectroscopy: incident radiation (continuous line) impact on a sample, in this case silicon, and thus, the scattered radiation (dashed-dot line) contains the Raman signal. Figure redrawn from [56].

2.5.2.3. MEMS structures

- **Bulge test method**

This method involves the application of uniform pressure p on a thin film window, i.e. a zone without substrate (see Figure 2.19) [56]. As a result, a bulge h is generated and can be estimated with Equation 2.42.

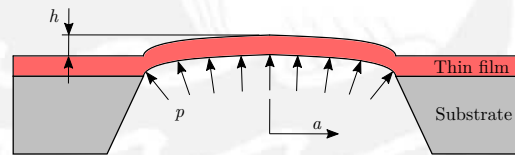


Figure 2.19.: Deflection h generated in a thin film window by a pressure p . Parameter a is in this case the radius of the membrane. Figure redrawn from [56].

$$p = C_1 \frac{\sigma_R t_f}{a^2} h + C_2 \left(\frac{E_f}{1 - \nu_f} \right) \frac{t_f}{a^4} h^3 \quad (2.42)$$

Where C_1 and C_2 are geometry factors, whereas a is the characteristic length of the membrane [56].

- **Strain gauge structures**

This type of structure is used to measure the displacement x caused by the residual stress relief in the film [56]. The residual stress is calculated from x and the dimensions of the structure according to Equation 2.43: L_C is the length of the pointer, L_A and L_B are the lengths of the anchorage arms, whereas L_O is the distance between the turning points of anchorage arms (see Figure 2.20) [3].

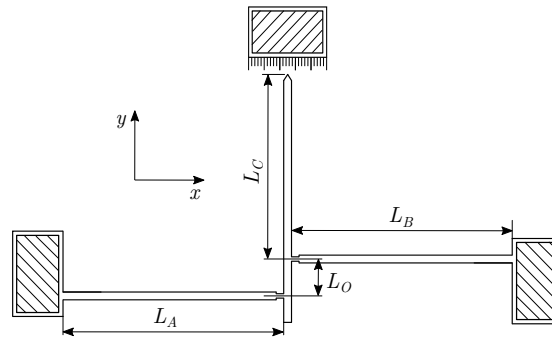


Figure 2.20.: Schematic view of a strain gauge structure. Figure redrawn from [56].

$$\sigma_R = \frac{L_O E}{(L_A + L_B)(L_C + L_O/2)} x \quad (2.43)$$

2.6. Finite Element Method

Abbreviated as FEM, it is a numerical technique used to solve complex engineering problems. It is based on the discretization of a continuous element and thus can be affected by computational errors and discretization errors. The former are related to the round-off process performed by the computer as well as the equations employed; whereas the latter are generated by the mismatch between the distribution of the discretization elements and the continuous structure [60].

2.6.1. Steps of FEM

The steps to apply the FEM are the following [60, 61]:

- a) Generate the geometrical model: Based on the real problem, the user develops a geometrical model (see Figure 2.21a).
- b) Discretize the model: Also known as mesh generation, in this step the continuous model is discretized in finite elements forming a mesh of elements and nodes (see Figure 2.21b). The elements used can be line elements, surface elements and solid elements. Some of them can be seen in Table 2.4.

Note that the quality of the mesh as well as the type of element impact on the results achieved by the finite element method. Moreover, there are dimensionless parameters available in Ansys used to describe the quality of a meshing. The most used are the following [63]:

- Element quality: It is calculated by the ratio of the element volume and the sum of the edge lengths of the element. It varies from 0 to 1: a 0 value means that the element has a negative or zero volume; whereas a 1 value states a perfect cubic element.

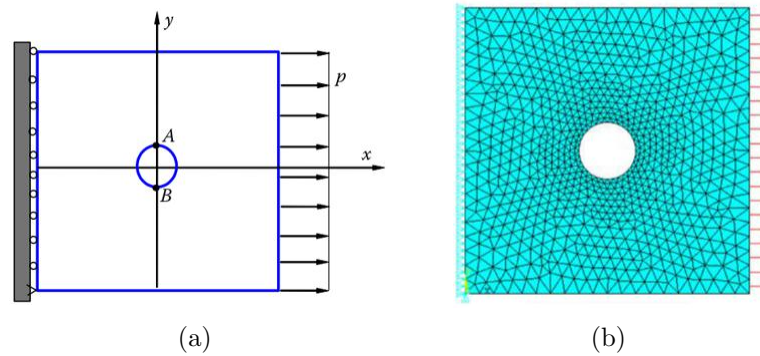


Figure 2.21.: Discretization of an element: (a) Continuous element, (b) Discretized element by finite elements, where boundary conditions and loads are applied. Figures extracted from [62].

- Aspect ratio: It indicates the ratio between the edge sizes of the elements. A value of 1 is the best possible aspect ratio for an element (see Figures 2.22a and 2.22b).
- Skewness: Parameter that indicates how close the element to the ideal element (equilateral triangle or equiangular quad) is. A value of zero means that the element has equal length sides, while a value of 1 indicates a fully corrupted element.

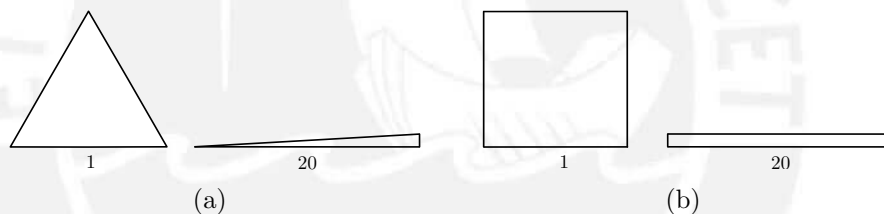






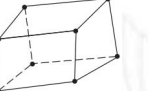




Figure 2.22.: Aspect ratio for triangular and rectangular elements: (a) Aspect ratio of 1 and 20 for triangular element, (b) Aspect ratio of 1 and 20 for rectangular element. Figures redrawn from [63].

- Define element properties: Select the material of the structure and the type of finite element to use in the method.
- Apply the loads: The forces, moments, temperatures, etc. that actuate in the real problem are applied on the model.
- Define boundary conditions: The contact type, the number of supports and the type of them are defined by the user.
- Solution of the algebraic system equations: As a result, the forces, stresses, deformations, strains, eigenfrequencies, among others desired parameters, are obtained.

Table 2.4.: Some elements used to discretize. Table extracted from [60].

Element of type	Name	Shape	Number of nodes	Applications
Line	Truss		2	Pin-ended bar in tension or compression
	Beam		2	Bending
Surface	4-node quadrilateral		4	Plane stress or strain, axisymmetry, shear panel, thin flat plate in bending
	8-node quadrilateral		8	Plane stress or strain, axisymmetry, thin plate or shell in bending
	3-node triangular		3	Plane stress or strain, axisymmetry, shear panel, thin flat plate in bending.
	6-node triangular		6	Plane stress or strain, axisymmetry, thin plate or shell in bending.
Solid	Brick: 8-node hexagonal		8	Solid, thick plate
	Wedge: 6-node pentagonal		6	Solid, thick plate. Used for transitions.
	Tet: 4-node tetrahedron		4	Solid, thick plate. Used for transitions.

2.6.2. Software packages

Nowadays, the available software that employ FEM are Ansys, Comsol, Abaqus, NASTRAN, etc. and their structure is based on the following stages [61].

- a) Pre-processor stage: Here the material properties, boundary conditions, discretization of the structure and application of loads are entered by the user and thus, the algebraic equations are defined for each element by the software. For each element, the software sets an equation that relates the stiffness matrix, the displacements and the forces as follows

$$[K] \{u\} = \{F\} \quad (2.44)$$

where matrix $[K]$ is the stiffness matrix, $\{u\}$ the vector of displacements at the nodes and $\{F\}$ is the vector of forces at the nodes.

- b) Solution process stage: The software solves the algebraic equations generated by the previous step to obtain the displacements at the nodes and thus, to calculate the strains as follows

$$\{\sigma\} = [K] \{\varepsilon\} \quad (2.45)$$

where $\{\sigma\}$ is the stress vector and $\{\varepsilon\}$ is the strain vector calculated with $\{u\}$.

- c) Post-processor stage: Results obtained by the previous stage are shown in graphics, e.g. displacements, strains, stress, etc. (see Figure 2.23). Besides, in this stage, the results are validated with reference values, which are achieved through analytical calculations or experiments.

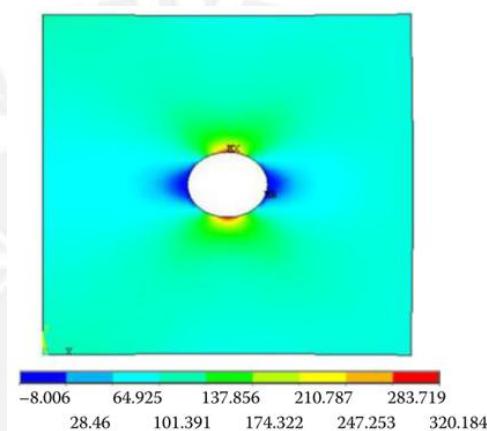


Figure 2.23.: Stress distribution, calculated by the FEM, to be analysed by the user. Figure extracted from [62].

Simulation of residual stresses

In Chapter 3 the residual stresses generated in multilayer MEMS structures will be addressed as a preliminary study about the residual stresses in wafers model with a single-layer thin film. First, the preparation processes of the MEMS structures will be presented. Second, the types of simulations proposed in this work will be explained. Finally, the results and comparison with theoretical equations and experiments are shown.

3.1. MEMS structures

The MEMS structures fabricated using the Cr_2AlC phase and AlN are doubly-clamped beams and cantilevers. Those structures consist of two main layers (silicon dioxide (SiO_2) and the thin film (Cr_2AlC or AlN), which are deposited successively following a pattern over a substrate (silicon). For instance, Figure 3.1 depicts two types of multilayer deposition of Cr_2AlC with the same Cr – C – Al pattern but at different layer thickness. This procedure is done to visualize the influence of the layers thicknesses as well as the pattern in the properties of the structure. Besides, the structures are fabricated at different lengths (l_b) to investigate the vibration behavior of the MEMS structures, since the eigenfrequencies depend on l_b according to Equation (2.16). The dimensions of the doubly-clamped beam are shown in Figure 3.2.

The multilayer beam structures have complex geometries and thus, the simulation will demand high calculation time, e.g. the change of section in the support from $4\ \mu\text{m}$ to $100\ \mu\text{m}$ requires refining meshing methods in that zone whereas a thickness of $2\ \text{nm}$ will need fine elements to get good results (see Figure 3.2). Therefore, a preliminary study considering a wafer geometry with a single-layer thin film was performed.

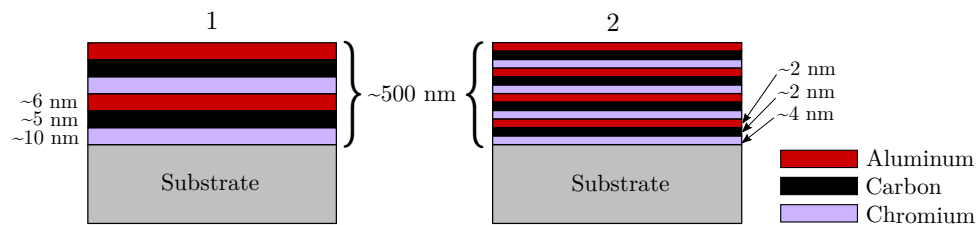


Figure 3.1.: Schematic section view of two multilayer deposition of Cr_2AlC : left side with layers of 10 nm, 5 nm and 6 nm of chromium, carbon and aluminum respectively; whereas on the right side with layers of 4 nm, 2 nm and 2 nm of chromium, carbon and aluminum respectively. Figure redrawn from [41].

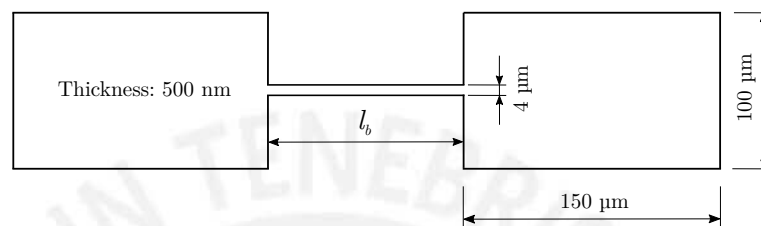


Figure 3.2.: Dimensions of the doubly-clamped beam structure. l_b represents the beam length and varies from 20 μm to 150 μm [4].

3.2. Preparation processes

The fabrication processes of Cr_2AlC and AlN thin films wafers involve the application of micromachining processes (see subsection 2.3.3) as follows.

- **Cr_2AlC phase**

Firstly, a 50 nm silicon dioxide layer was applied as a diffusion barrier on a 250 μm silicon substrate in order to prevent an undesirable intermixing of the $\text{Cr} - \text{C} - \text{Al}$ layers and the substrate [41, 64]. Secondly, the pure element layers were applied consecutively using a sputtering system forming a 500 nm thickness layer at 22 $^\circ\text{C}$. Then the wafer was heated at 600 $^\circ\text{C}$ for 30 s using a heating rate of 15 K/s and then cooled using a cooling rate of 4 K/s to 22 $^\circ\text{C}$.

- **AlN**

Alike the previous MAX phase, a 50 nm SiO_2 layer was applied between the nitride and the 250 μm silicon substrate. Then the substrate and the silicon dioxide were heated to a temperature of 1190 $^\circ\text{C}$ [65]. Afterwards, the AlN was deposited by MOCVD at 1190 $^\circ\text{C}$ and subsequently cooled to room temperature.

The temperature curves of the wafers are shown in Figure 3.3. As can be seen, the heating for both materials was performed in two stages, followed by a cooling process to room temperature. Since this work performed static simulations (see section 3.4), the time did not play an important role and thus, the heating, deposition and cooling processes were approximated as one step each one.

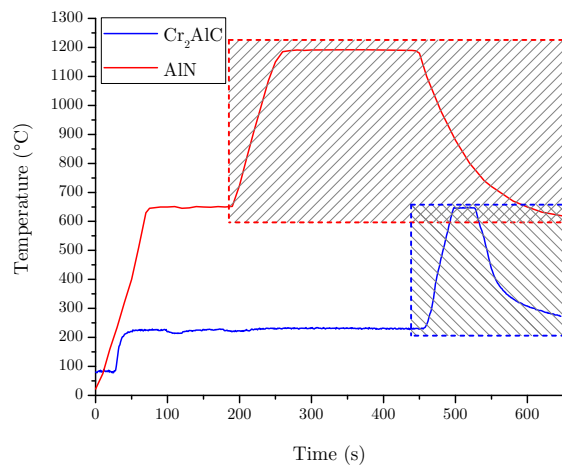
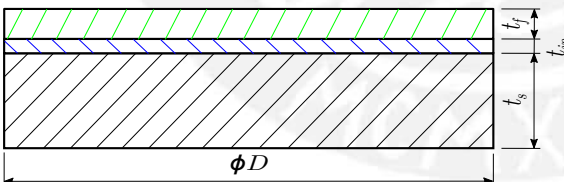


Figure 3.3.: Temperature curve of the preparation processes of AlN and Cr₂AlC films. Data enclosed by the sparse-line rectangles were considered as single steps each one.

3.3. Dimensions of the wafer

Even though the thin film is a multilayer body, it was considered as single-layer. Otherwise, given the very thin thicknesses in a multilayer body, e.g. 2 nm, the mesh operation would require high calculation time and high memory consumption to generate elements with good quality parameters (see 2.6.1). Therefore, the AlN and Cr₂AlC wafers consisted of a substrate, a layer of SiO₂ and a single-layer film with thicknesses noted as t_s , t_{in} and t_f respectively. The dimensions are shown in Table 3.1.

Table 3.1.: Dimensions of the wafer considered in the simulation.

Section view of the wafer	Thin film	D (mm)	t_s (μm)	t_{in} (nm)	t_f (nm)
	AlN	50	250	50	240
	Cr ₂ AlC	50	250	50	500

Furthermore, the properties of the silicon dioxide considered in the simulation can be seen in Figures 3.4a, 3.4b, 3.4c and 3.4d; whereas the substrate properties (anisotropic silicon), in Table 3.2 and Figure 3.5.

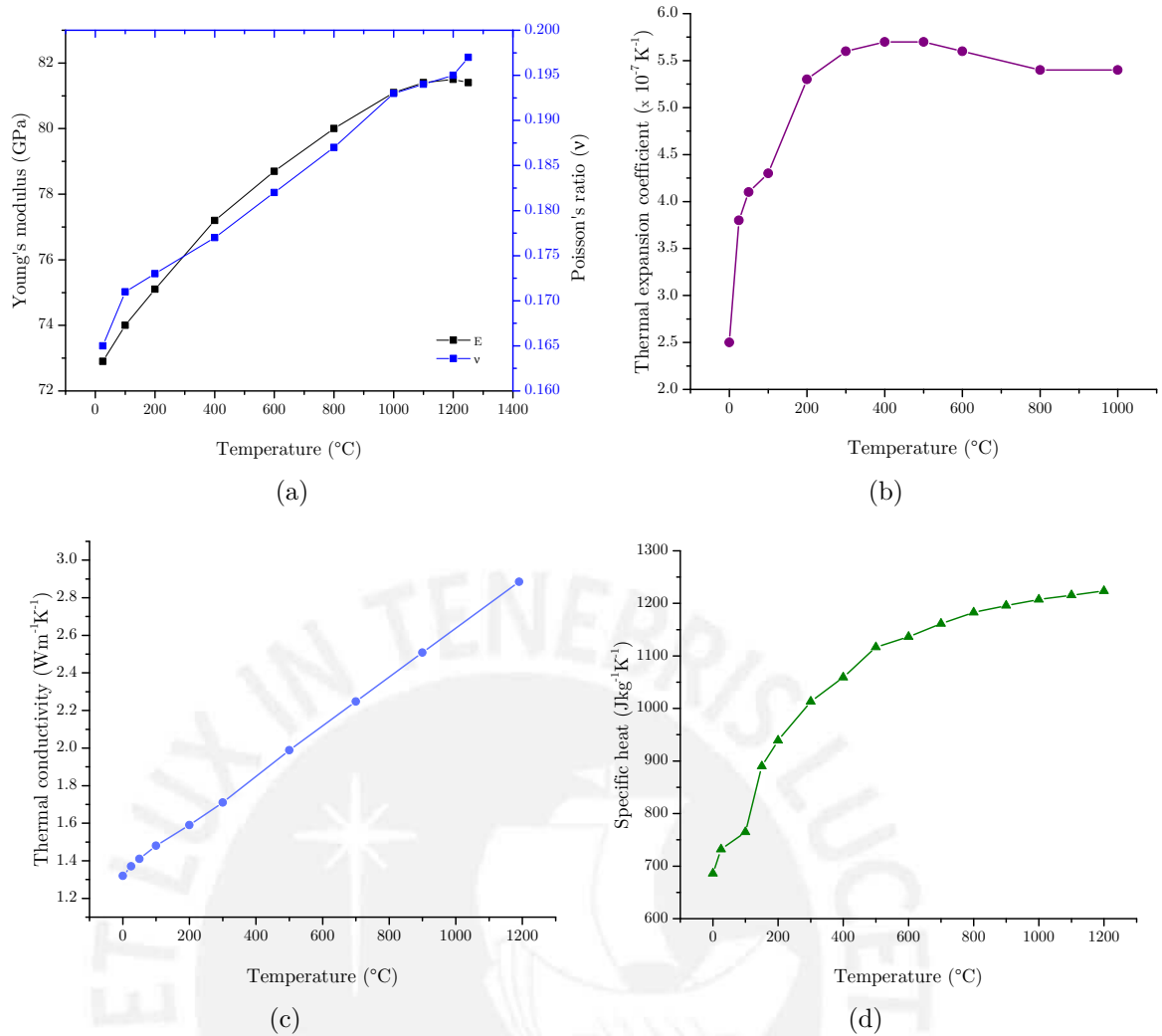


Figure 3.4.: Parameters of SiO₂: (a) Young's module (E) and Poisson's ratio (ν), (b) TEC, (c) Thermal conductivity, (d) Specific heat. Figures based on data from [66].

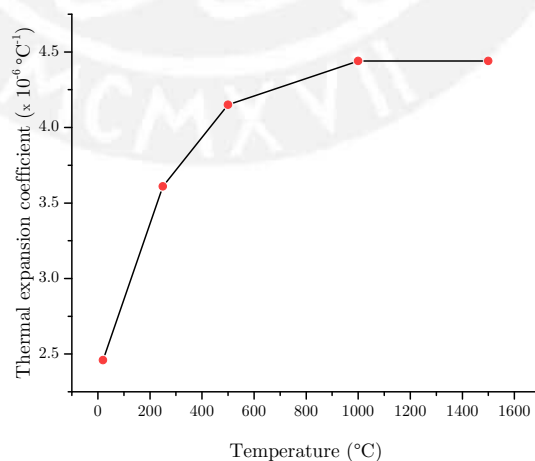


Figure 3.5.: Thermal expansion coefficient of anisotropic silicon. Figure based on data from ANSYS software.

Table 3.2.: Mechanical and thermal parameters of anisotropic silicon. Data extracted from Ansys software.

	Parameter	Magnitude
	Density (kg/m^3)	2330
Elastic constants	c_{11} (GPa)	166
	c_{12} (GPa)	64
	c_{13} (GPa)	64
	c_{33} (GPa)	80
	c_{44} (GPa)	80
	TEC ($^{\circ}\text{C}^{-1}$)	see Figure 3.5
	Heat capacity ($\text{Jkg}^{-1}\text{C}^{-1}$)	702
	Thermal conductivity ($\text{Wm}^{-1}\text{C}^{-1}$)	124

3.4. Types of simulation

Since this work is a first approach to the simulation of residual stresses in thin films, it considered static simulations with the aim of reducing calculation time. This, in turn, eased the variation of parameters, such as the element size for the mesh and boundary conditions. The obtained results could be applied to subsequent simulations, e.g. transient thermal-mechanical, modal analysis, among others. In addition, since the origin of the quenching and intrinsic stresses is based on the lattice mismatches and shrinkage of the splats during the deposition (see section 2.5), which cannot be represented in static simulations due to their atomic interaction, the residual stresses simulated in this thesis were thermal stresses.

On the other hand, the static simulation of the residual stresses was performed from simple to complex. Therefore, the types of simulation performed in this work are shown in Figure 3.6 and are described briefly as follows.

1. Simulation 1: It is a static simulation where thermal loads were applied to a quadrant of the circular plate (see section 3.5), composed of substrate, SiO_2 layer and thin film. Those loads were applied as heating and cooling steps from room to deposition temperature and vice versa.
2. Simulation 2: Since the thin film layer was always present in the model in simulation 1, which did not depict the deposition of the thin film, this simulation considered the birth and death technique available in ANSYS software to represent the layer deposition. This technique does not remove the layer but multiplies the stiffness matrix of the killed element by a reduction factor (for further information, see section 3.6). Moreover, simulation 2 was split under the considered geometrical model as follows:
 - 2.1. Axisymmetric model: The three-dimensional wafer model was approximated in a two-dimensional model by considering its transversal section (see subsection 3.6.1).

- 2.2. Axisymmetric model with initial curvature: The previous model was enhanced by adding the initial curvature of the wafer obtained by deflection measurements (see subsection 3.6.2).
- 2.3. Quadrant model with initial curvature: It is a three-dimensional model generated by the revolution of the above mentioned transversal section (see subsection 3.6.3).
3. Simulation 3: It pursued the residual stress simulation by detecting the contact between the thin film and the bilayer solid consisting of the SiO_2 layer and the substrate (see section 3.7). Therefore, at the beginning, the thin film and the bilayer solid were separated one from another and then they were approached until the contact was detected by the software.

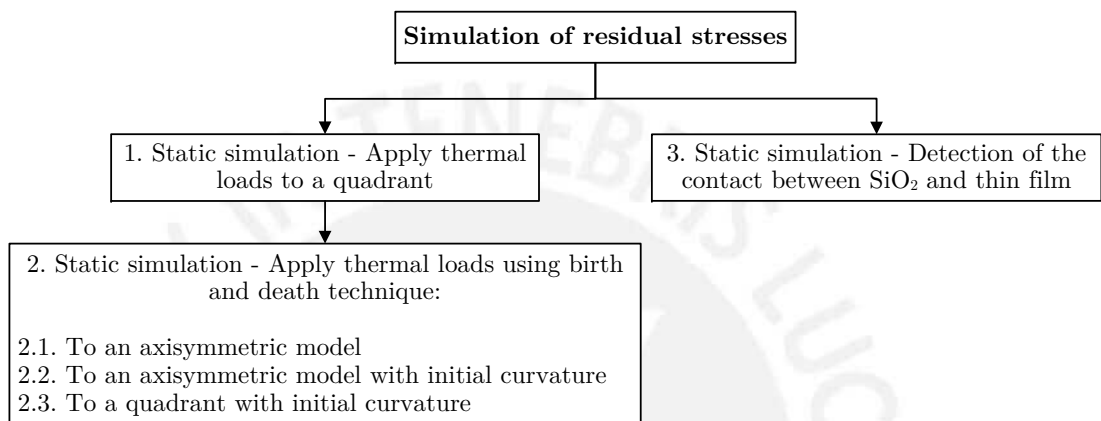


Figure 3.6.: Types of analysis performed to simulate the residual stresses.

3.5. Simulation 1 - Static load to quadrant

This simulation took into account a quadrant of the entire wafer as a geometrical because of its symmetry with regard to the y -axis [53]. Figure 3.7 depicts the wafer solid, approximated as three cylinders joined together, and the quadrant considered as the geometrical model.

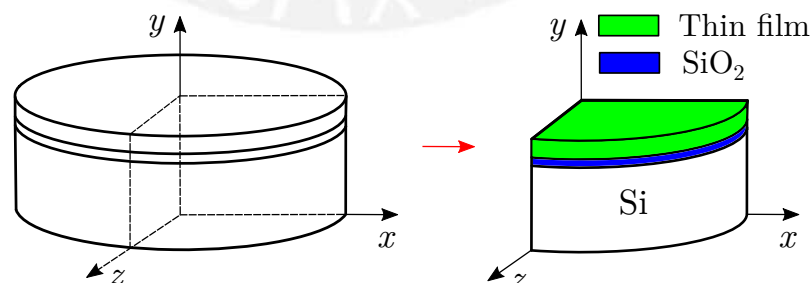


Figure 3.7.: Schematic representation of the quadrant: the wafer (on the left side) where the quadrant solid comes from (on the right side).

The steps followed in the simulation are described in the flowchart (see Figure 3.8). The first step was to build the quadrant model and generate the mesh, as well as to include the material properties in the program. Then to define the model supports and to apply the thermal loads at the deposition temperature, i.e. 1190 °C for the AlN and 600 °C for the Cr₂AlC, followed by a cooling process to room temperature. Finally, the results were compared with the equations described in section 2.5.1.

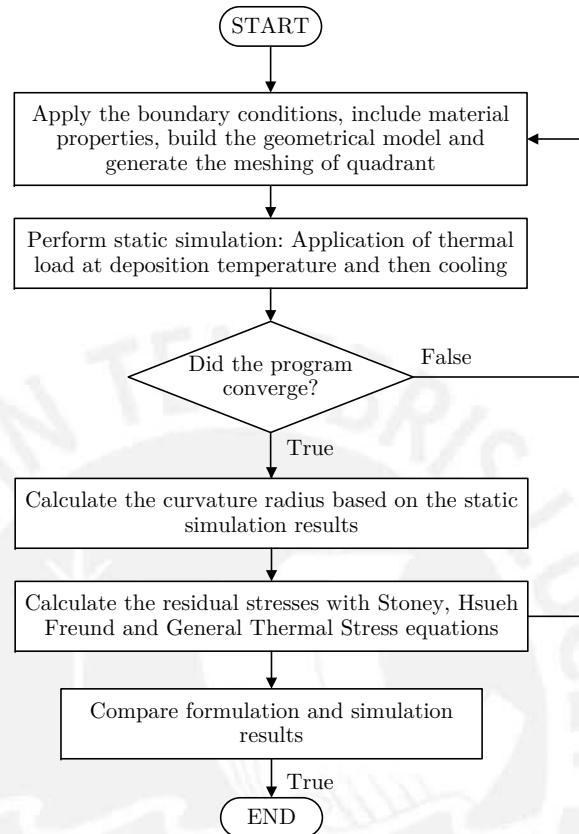


Figure 3.8.: Steps of simulation 1 - static load to quadrant.

3.5.1. Mesh

The circular plate was generated by employing a cyclic symmetric operation applied to a quadrant. This is shown in Figure 3.9a, where that operation required a cylindrical coordinate system as a reference and low and high regions, noted in blue and red squares respectively, to develop the revolution respect to the generating axis (z-axis in the cylindrical coordinate).

Since the quadrants were three-dimensional solid, a 3D structural solid element type was selected to generate the meshing. Among the element types available in ANSYS, the 3D structural solids are SOLID185 and SOLID186 (see Figure 3.10), whose characteristics are the following: SOLID185 is a 3D 8-node structural solid (IJKLMN) with three degrees of freedom at each one along x, y and z directions [67], whereas SOLID186 is a 3D 20-node structural solid (IJK . . . WX) with equal degree of freedoms that the latter, but displays a quadratic displacement behavior [67], which could give

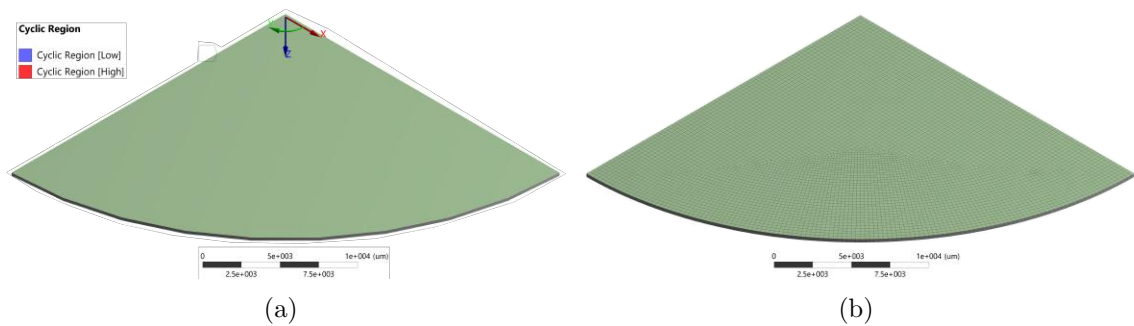


Figure 3.9.: Simulation 1 - Mesh process: (a) Cyclic symmetric operation applied to the quadrant. Regions Low and High denote the orientation of the revolution respect to the cylindrical coordinate system in the center, (b) Mesh of the quadrant model.

a better representation of the deformation along y-axis. Hence, the SOLID186 was chosen as element type for the mesh. Moreover, since the simulation was performed in ANSYS Workbench, the element was assigned automatically by the software. Otherwise, if a modification of the element type is required, the APDL command `et, 1, SOLID186`, where 1 is the reference number of the element. The mesh of the quadrant is shown in Figure 3.9b.

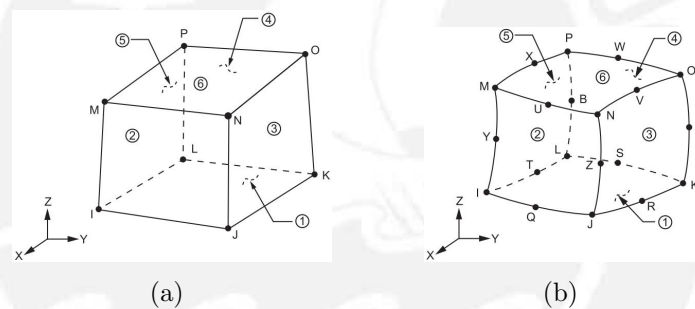


Figure 3.10.: 3D structural element types: (a) SOLID185, (b) SOLID186. Figures extracted from [67].

On the other hand, the element sizes were varied downward until the system ran out of memory during the meshing process or there was not enough memory to calculate a solution by ANSYS. For that reason, the element sizes were $300\ \mu\text{m}$ for the substrate and $200\ \mu\text{m}$ for the silicon dioxide layer and thin film. Although those values were thicker than their physical thicknesses, i.e. $240\ \text{nm}$ for the AlN and $500\ \text{nm}$ for the Cr_2AlC , the program was capable of generating the mesh. These element sizes impact on the mesh by reducing its quality parameters (see Table 3.3), e.g. the mesh had aspect ratios of 572.69 and 275.09 for the AlN and Cr_2AlC quadrants and thus, the elements were thin rectangles (see Figure 2.22b).

Table 3.3.: Meshing parameters of the AlN and Cr₂AlC bilayer quadrants.

Parameter	AlN	Cr ₂ AlC
Nodes	137699	137699
Elements	19409	19409
Element quality (average)	0.302	0.303
Aspect ratio (average)	572.69	275.09
Skewness (average)	0.016	0.016

3.5.2. Simulation

The adherence between the surfaces required to select a contact type to be included in the model. The contact types available in ANSYS are determined by the permitted separation of each one along the normal direction, i.e. a gap between the bodies, or relative sliding between the contacting bodies. The main differences among them are shown in Table 3.4. Although the adherence depends on different factors such as the presence of oxides, grains sizes, interface structures, among others [68, 69], in this work a perfect adherence between the contacting bodies was considered with the purpose to simplify the model and thus, relate the deformations and stresses of the bodies to each other. Hence, the bonded contact type was selected as contact model between the silicon and thin film layer.

Table 3.4.: Contact type characteristics available in ANSYS. Table based on [70].

Type	Separation in normal direction	Sliding in tangential direction	Comments
Bonded	No	No	Behaves as glued contact
No separation	No	Yes	Assumes a zero coefficient of friction
Frictionless	Yes	Yes	Assumes a zero coefficient of friction
Rough	Yes	No	Considers an infinite coefficient of friction between the bodies
Frictional	Yes	Yes	Sliding occurs if the tangential force exceeds the static friction force

Once the mesh was obtained, the next steps were to apply the load and the supports. Regarding the loads, they were applied to the substrate and SiO₂ layer as thermal loads at the deposition temperature (see Figure 3.11a). In relation to the supports, the displacement in the y-axis of the circular arc of the quadrant in contact with the XZ plane (see Figure 3.11b) was limited to zero in order to visualize the curvature of the plate.

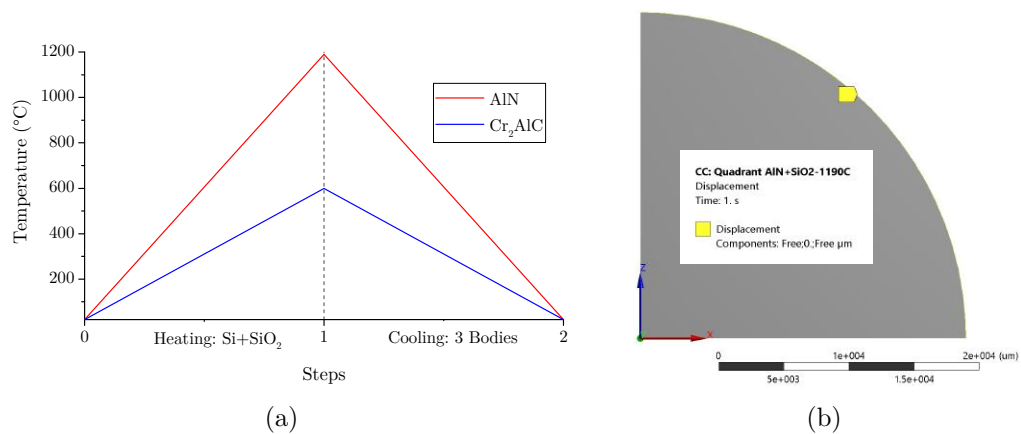


Figure 3.11.: Boundary conditions of the quadrant: (a) Thermal load applied to the substrate and SiO_2 layer, (b) Circular arc of the substrate (marked in yellow) limited to a zero displacement in y-axis.

Due to the thermal load, the substrate will expand whereas the thin film shrink. However, because of the contact between them, the bodies must maintain the same length, which will cause tensile stress in the film and compressive stress in the substrate [71]. This stress difference will generate a moment in the wafer, which will be counteracted by a bending. Therefore, an upward concavity of the wafer, i.e. along the +y axis, was expected.

The stresses generated at the temperature deposition are shown in Figure 3.12, whereas the deformations along the x and y axis are depicted in Figures 3.13 and 3.14. As can be seen in Figures 3.13a and 3.13b, the prediction about the deflection was certain. Furthermore, the maximum stress was generated in the thin film (red areas in Figure 3.12), which is consistent with the residual stress theories.

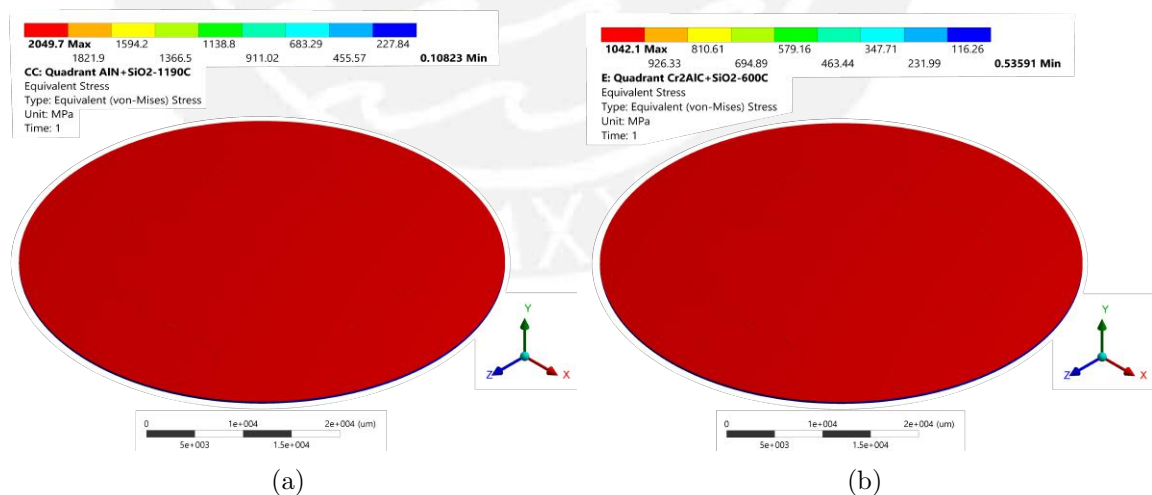


Figure 3.12.: Simulation 1 - Equivalent stresses (von Mises) in MPa generated at the deposition temperature: (a) AlN, (b) Cr_2AlC .

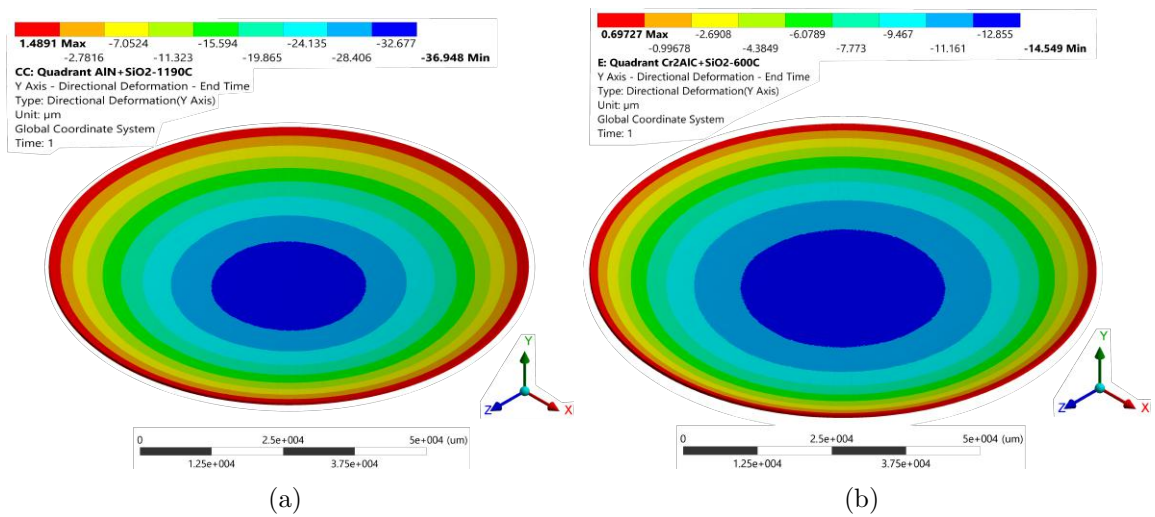


Figure 3.13.: Simulation 1 - Deformation (in μm) along y axis at the deposition temperature: (a) AlN, (b) Cr₂AlC.

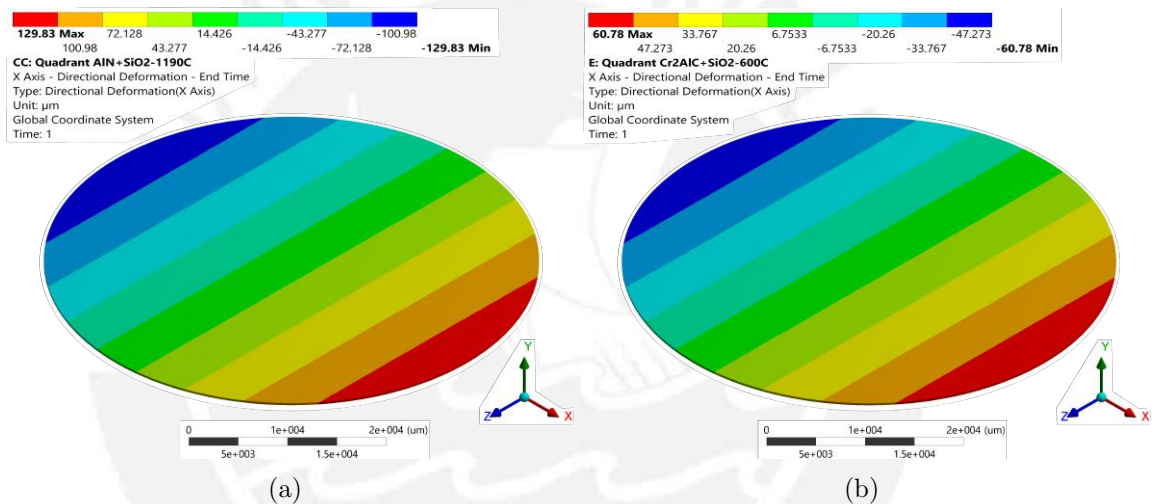


Figure 3.14.: Simulation 1 - Deformation (in μm) along x axis at the deposition temperature: (a) AlN, (b) Cr₂AlC.

3.5.3. Comparison with theoretical stresses

The results were compared with the equations discussed in subsection 2.5. Those depend mainly on the thicknesses (t_s , t_f), Young's modules (E_s , E_f) and the radius of curvature (ρ). The value of ρ was estimated as follows

$$\rho = \frac{R^2 + \delta_y^2 + \delta_x^2 + 2R\delta_x}{2\delta_y} \quad (3.1)$$

where δ_x and δ_y are respectively the deformation of the substrate along x and y axis obtained previously in the simulation. Equation 3.1 was obtained by applying the

Pythagorean theorem according to Figure 3.15, where a constant curvature, as well as equal deformations along x and z-axis, were considered.

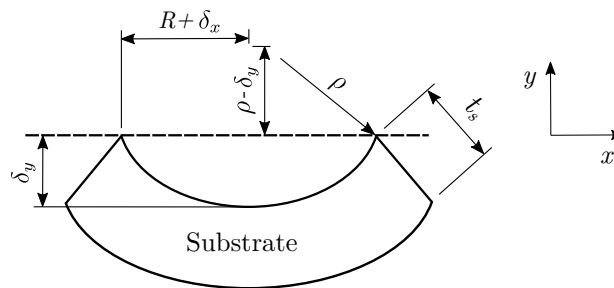


Figure 3.15.: Deformed circular plate characterized by a radius of curvature ρ and deformations δ_x and δ_y . Note that due to their thinner thickness, the thin film and SiO₂ layer were not graphed.

Furthermore, since the stresses formulations 2.21, and 2.25 consider isotropic material properties, the anisotropic properties were converted into moduli values with Equations 2.1, 2.2, 2.3 and 2.4 in order to obtain the Young's module and the Poisson's ratio. On the other hand, since in the first step (see Figure 3.11a) the substrate was heated from room to deposition temperature while the thin film was kept at room temperature, the thermal stress (see Equation 2.36) was estimated by considering only the substrate's TEC at the deposition temperature.

Figure 3.16 shows the comparison between theoretical formulations and simulation results for the AlN and Cr₂AlC. Stresses at the deposition temperature estimated by Stoney and Freund equations were lower than simulation results because the stresses were not residual type, but thermal stresses since thermal loads were still applied at the end of step 1 (see 2.5). On the other hand, thermal stresses estimated by the general thermal stress equation (third group of columns in Figure 3.16) were very close to these of the simulation. This, in turn, showed that the element sizes of the mesh generated in 3.5.1, as well as the supports described in Figure 3.11b, permitted simulate the thermal stress.

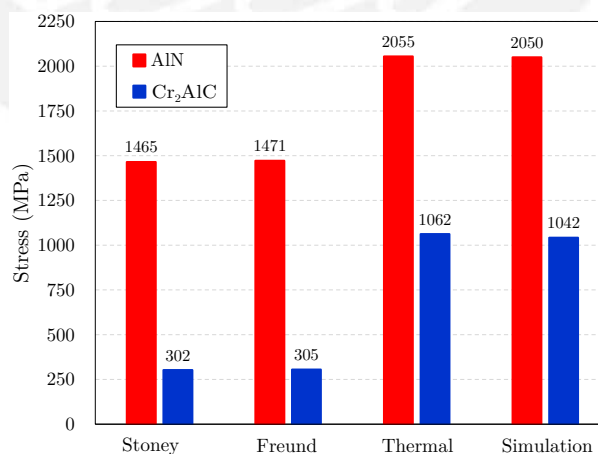


Figure 3.16.: Stresses at the deposition temperature estimated by theoretical formulations and simulations for AlN (in red) and Cr₂AlC (in blue).

On the other hand, Figure 3.17 depicts the residual stresses, i.e. those generated after the cooling at the end of step 2. As can be seen, the maximum values of the residual stresses were virtually none: 0.18 MPa and 0.02 MPa for the AlN and Cr₂AlC respectively. This occurred because the three bodies (substrate, SiO₂ layer and thin film) were always active during simulation 1 and therefore the three bodies behave like a whole one. As a result, the stress caused by the heating step was relaxed by the cooling step because the starting and final temperatures were the same and equal to 22 °C. Hence, a method to face this challenge will be described in the next section.

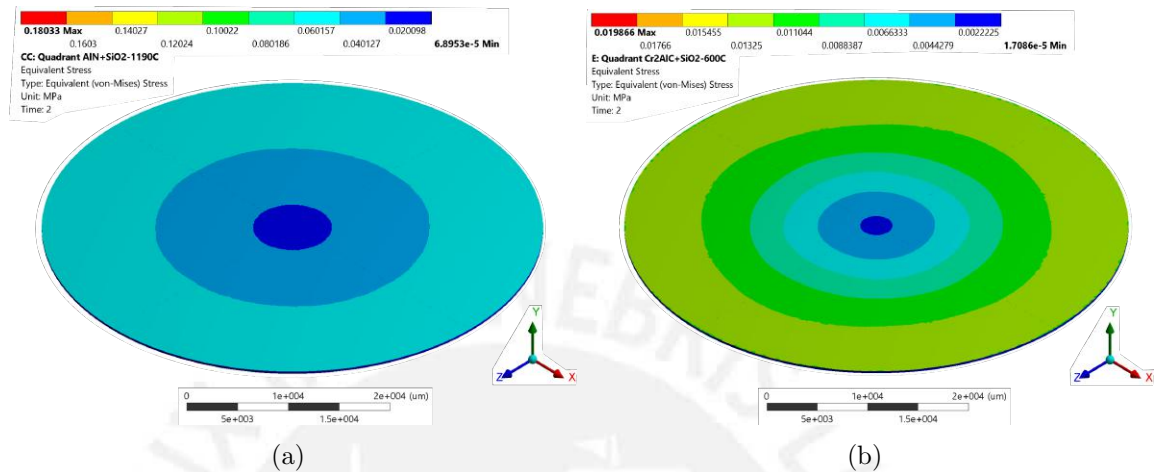


Figure 3.17.: Simulation 1 - Equivalent stresses (von Mises) in MPa generated after the cooling process: (a) AlN, (b) Cr₂AlC.

3.6. Simulation 2 - Static load by using birth and death technique

This simulation employed the birth & death technique by including the corresponding APDL commands to the model in ANSYS Workbench with the aim of representing the deposition of the thin film. This technique does not remove the layer, but multiplies the stiffness matrix of the killed element, in this case, the thin film, by a reduction factor¹ of 10⁻⁶. The effect on the solution process stage of the software can be understood by modifying Equation 2.45 as follows:

$$\{\sigma_k\} = [f_r K_k] \{\varepsilon_k\} \quad (3.2)$$

where σ_k , $[K_k]$ and $\{\varepsilon_k\}$ are the stress vector, the stiffness matrix and the strain vector in the killed element respectively; while f_r is the reduction factor equal to 10⁻⁶. Due to the very low value of f_r , the effect of the killed element can be neglected. Otherwise, f_r is equal to 1 when the body is born. Therefore, this technique allows beginning a

¹http://www.ansys.stuba.sk/html/guide_55../g-adv/GADV6.htm (visited on 20/02/17)

simulation with a killed body, which can be born at later steps and thus, was used to simulate the thin film deposition.

This simulation followed the flowchart shown in Figure 3.18. First, an axisymmetric simulation was performed to simplify the geometrical model. Second, a simulation considering a quadrant solid was conducted to visualize a three-dimensional deformation of the wafer. Third, the residual stresses were calculated by the wafer curvature measurement (see subsection 2.5.2) from experimental data and finally, the simulation and experimental results were compared.

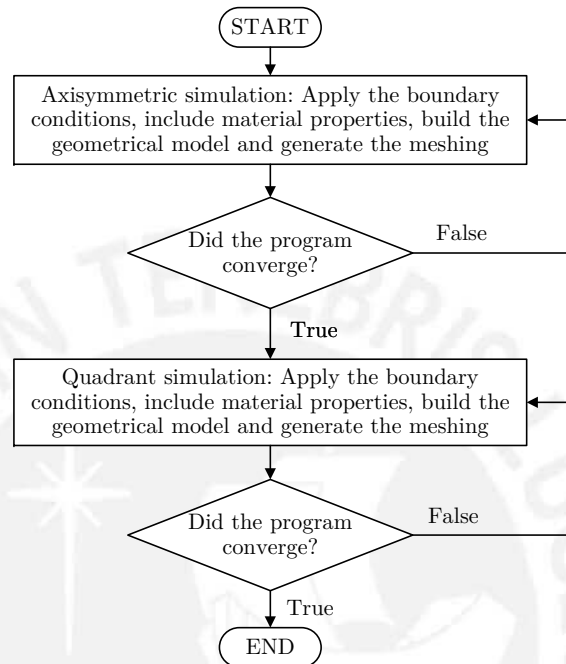


Figure 3.18.: Simulation 2 flowchart.

Unlike simulation 1, this simulation increased the number of layers by including the SiO_2 layer. Moreover, with the aim of representing the thin film deposition, the APDL commands, as well as the thermal loads, should be executed in the followings steps:

1. Step 1: Heating the substrate and SiO_2 layer from room temperature to process temperature shown in section 3.2. In this step, the thin film layer was killed or deactivated by the command `ekill`. Previously, the user must tag the body to be killed, i.e. to give the body a reference name to be used in the subsequent steps. It was done by including a command in the geometry section, e.g. `part1=matid`, where `matid` is the material number of the body. Then the body was selected with the command `esel,s,mat,,part1` and then `ekill,all`.
2. Step 2: Maintaining the process temperature. The thin film was also deactivated.
3. Step 3: The thin film layer was activated and the temperature of three bodies dropped to room temperature. Therefore, the body was selected previously with `esel` and then activated with the command `ealive`. Besides, the reference temperature of the body was changed to the process temperature in order to

activate the body with zero deformation [49, 53]. This can be done by changing it in ANSYS Workbench (selecting Geometry-Thin Film-Reference Temperature by Body) or employing the APDL command `MP, REFT, part1, temp`, where `temp` was the process temperature. The correct usage of each option will be discussed in 3.6.1.2.

4. Step 4: The bodies were kept at room temperature.

3.6.1. Axisymmetric simulation

This simulation approximated the cylindrical solid in a two-dimensional transversal section with the aim of reducing the calculation time [72, 73]. Hence, an axisymmetrical geometry was included to the program by taking into account the conditions set by ANSYS [67]: the transversal section must be generated in the x-y plane with positive x values, as well as symmetric regarding the y-axis in such a way it generates the solid when the area is rotated respect to that axis. Figure 3.19 depicts a schematic view of the area.

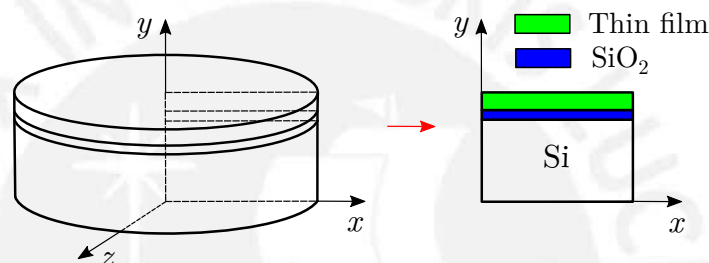


Figure 3.19.: Schematic view of the transversal section: the 3D three-layered wafer (on the left side) where the 2D area comes from (on the right side). Figure based on [74].

3.6.1.1. Mesh

According to ANSYS Mechanical APDL Element Reference [67], the recommended elements to work with a 2D axisymmetric model are PLANE182, PLANE183, SHELL208 and SHELL209. Nevertheless, the shell elements were discarded because they are commonly used to model shell bodies such as pipes, tanks among others [67]. The characteristics of both plane elements are the following (see 3.20a): PLANE182 is a 4-node (IJKL) structural solid with two degrees of freedom at each one along x and y directions [67] and has a linear interpolation function [75]; whereas PLANE183 is a 8-node (IJKL-MNOP) structural solid with two degrees of freedom at each one along x and y directions [67] and unlike the previous element, has a quadratic interpolation function [75]. Since the interpolation function describes the change of the degrees of freedom throughout the element edges, a quadratic formulation could give a better representation of the deformation along the y-axis of the transversal section (see Figure 3.20b). Therefore, the PLANE183 was chosen as the element for the cross-section.

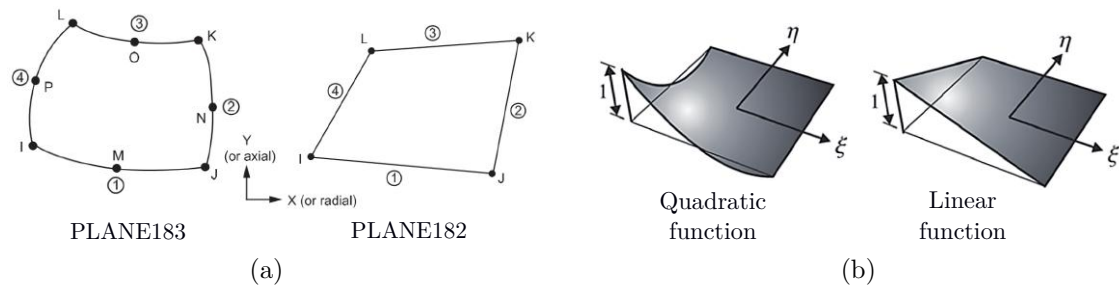


Figure 3.20.: Element features available in ANSYS: (a) Plane elements employed in axisymmetric models, (b) Changes in displacement obtained with different interpolation function, note that ξ and η are the centroidal coordinates of the 2D element [75]. Figures of (a) extracted from [67] and of (b) extracted from [75].

Likewise, the meshing described in 3.5.1, the element was assigned automatically by the software. Otherwise, the APDL command `et` can be added as `et, 1, PLANE183` if necessary. Furthermore, due to the thin film thicknesses, sizing and meshing methods were included to the geometry.

- Sizing methods: Due to the thicker thickness of the substrate, its element size can be bigger than the other solids. Therefore, considering a $125\ \mu\text{m}$ element size for the substrate, an aspect ratio of 1 was obtained because the substrate dimensions are multiple of 125. Furthermore, in order to obtain an aspect ratio of 1 for the SiO_2 layer, the element size must be $50\ \text{nm}$ generating 500 000 elements, which would lead to a large calculation time only for the meshing and consequently for the simulation. Hence, a $1\ \mu\text{m}$ size was chosen for the SiO_2 layer. Concerning the thin film, its element size was chosen by trial and error varying from $5\ \mu\text{m}$ to the corresponding thickness: $240\ \text{nm}$ for the AlN , whereas $500\ \text{nm}$ for the Cr_2AlC . The results are shown in 3.6.1.2.
- Meshing methods: The methods Quadrilateral Dominant and the Multizone Quad/Tri, with the option All Quad activated, were chosen in order to generate quadrant models. The former is based on the patching conforming algorithm, which creates the meshing respecting all the faces and boundaries of the surface and thus, the meshing captures the geometry details [63]. In contrast, the latter is based on the patching independent algorithm, which does not respect necessarily all the faces and boundaries and thus, it is employed to generate uniformly meshing [63].

Nevertheless, when the Quadrilateral Dominant method was selected, the ANSYS meshing algorithm did not create the mesh due to poor quality elements and in some cases, i.e. for thinner element sizes, the program ran out of memory. Therefore, the meshing option chosen was the Multizone. The mesh parameters of the aluminum nitride and MAX phase are shown in Table 3.5.

Table 3.5.: Meshing parameters of the AlN and Cr₂AlC axisymmetric sections.

Parameter	AlN	Cr ₂ AlC
Nodes	287507	240942
Elements	57580	48267
Element quality (average)	0.367	0.613
Aspect ratio (average)	10.5	11.4
Skewness (average)	4.29×10^{-10}	3×10^{-10}

3.6.1.2. Simulation

The supports are shown in Figure 3.21a, where the left edges of the transversal section were fixed in the x-axis ($u_x = 0$) in order to allow a free deformation of the wafer center. Besides, the bottom right vertex of the substrate was fixed in the y-axis ($u_y = 0$), otherwise the simulation cannot converge because the entire section could move along the y-axis transgressing the static analysis. In addition, the applied thermal load followed the steps shown in section 3.6 and can be seen in Figure 3.21b.

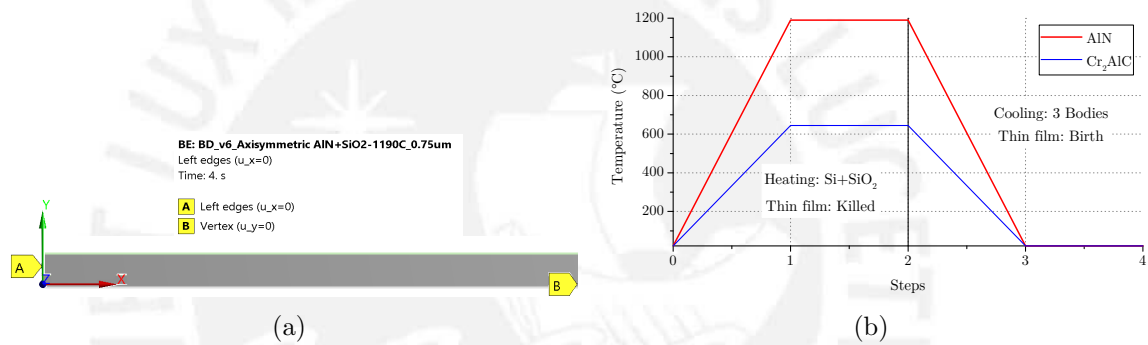


Figure 3.21.: Boundary conditions of the axisymmetric section: (a) Left edge fixed in x axis ($u_x = 0$ noted as A) and right vertex fixed in y axis ($u_y = 0$ noted as B), (b) Thermal load applied step by step.

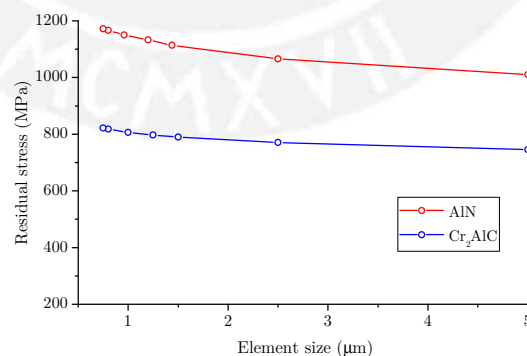


Figure 3.22.: Variation of residual stress with regard to the element size.

Besides, alike simulation 1, the bonded contact type was selected as contact model between the silicon and SiO₂ layers and also between the SiO₂ and the thin film layer.

As it was explained previously in 3.6.1.1, the simulations were performed by changing the element size until it reaches the layer thickness. However, the minimum given value for both layers was $0.75\ \mu\text{m}$, because the meshing algorithm could not mesh the area since the program ran out of memory when the element size was $240\ \text{nm}$ and $500\ \text{nm}$ for the AlN and Cr_2AlC layers respectively. The results are shown in Figure 3.22.

3.6.1.3. Results

As it was described in 3.6, there are two options to change the reference temperature of a body. The first alternative is to change this parameter with ANSYS Workbench interface, which allows the user to vary it only at the beginning of the simulation and thus, this change is valid from the first simulation step henceforth. On the contrary, by employing the APDL command `MP, REFT`, the reference temperature can be changed at the desired step. According to the preparation processes described in section 3.2, the sputtering deposition of the Cr_2AlC occurred at room temperature ($22\ ^\circ\text{C}$), while the aluminum nitride was deposited at $1190\ ^\circ\text{C}$. Thus, the change with ANSYS Workbench fitted the manufacturing process of the aluminum nitride, whereas the APDL command satisfied the MAX phase fabrication.

- **Aluminum nitride**

As mentioned above, the deposition of the AlN thin film was represented by changing its reference temperature with ANSYS Workbench. This was validated by plotting the deformations in y-axis with both alternatives and compared them with deflection measures of the wafer. Figure 3.23 depicts the APDL results, where a downward concavity of the section is shown; while Figure 3.24 shows the ANSYS Workbench results, where the section was deformed upward with a maximum deflection of $-35\ \mu\text{m}$. Given that the shape of the axisymmetric section deformed by the APDL commands was consistent with the wafer shape measured by experiments (see Figure 3.25), i.e. both with an upward concavity, the change of temperature reference with APDL commands was validated.

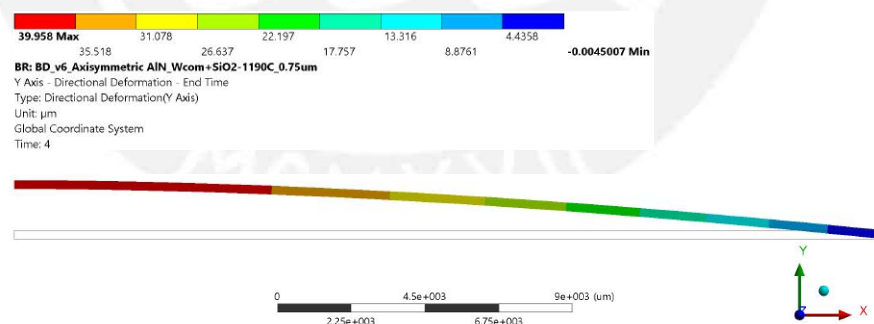


Figure 3.23.: Deformation along y axis (in μm) of the AlN axisymmetric model by changing the temperature reference with APDL command.

Moreover, the residual stresses generated on the left and right sides of the axisymmetric model, which represented the wafer center and wafer circumference respectively, were plotted to visualize the stress distribution. Figure 3.26 depicts that the higher residual stresses are generated in the thin film, where the stresses

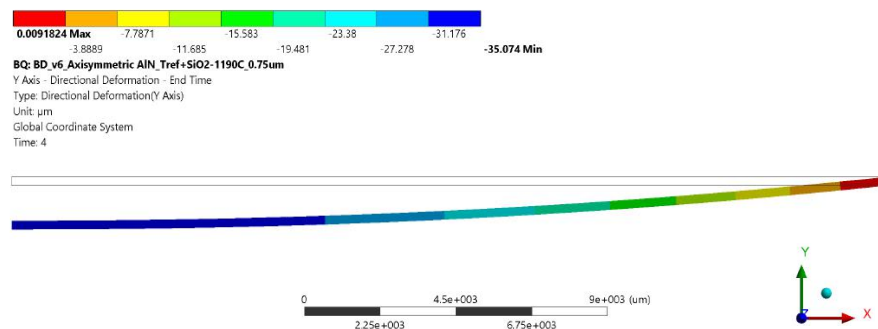


Figure 3.24.: Deformation along y axis (in μm) of the AlN axisymmetric model by changing the temperature reference with ANSYS Workbench interface.

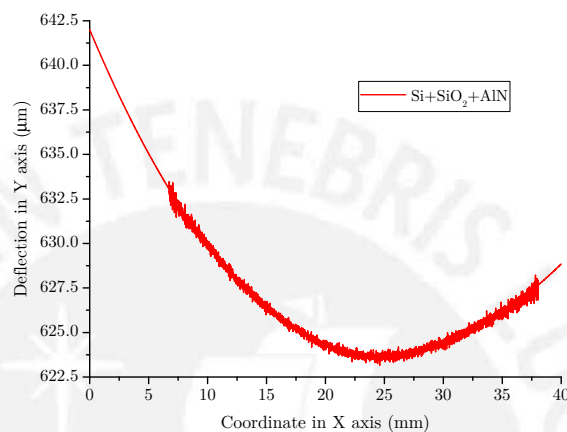


Figure 3.25.: Deflection scans along the x axis of the AlN wafer after the AlN layer deposition (red marks).

reach a maximum value of 1172 MPa on the left side and decrease towards the right side. Thus, as a result of the cooling, the maximum stresses are generated at the wafer center and decrease towards the wafer circumference. Besides, the stresses in the SiO_2 layer and substrate are lower, which vary from 0.06 MPa to 390.8 MPa.

Furthermore, the plots of residual stress distribution allow visualizing the stresses in each layer. As seen in Figure 3.27, the residual stresses in x-axis vary principally along the $+x$ direction from the center of the wafer (left side in the axisymmetric model) to the border (right side in the axisymmetric model), where residual stresses oriented in $-x$ axis appear. This large difference causes a resultant stress along the $+x$ direction with added to the stresses in the substrate and silicon dioxide, oriented in $-x$ direction, yield a moment in $-z$ direction. For that reason, the axisymmetric model deforms following an upward concavity with the aim of compensating that moment.

On the other hand, the stress distribution plots permit to visualize possible failure modes. In the case of the normal stresses in x-axis for (Figure 3.27), the difference in their directions lead to a buckling delamination as it can be seen in Figure 3.28, which would separate the thin film layer from the silicon dioxide.



Figure 3.26.: Distribution of equivalent stresses (von Mises) in MPa generated in the AIN axisymmetric model from the left to the right side of the model.

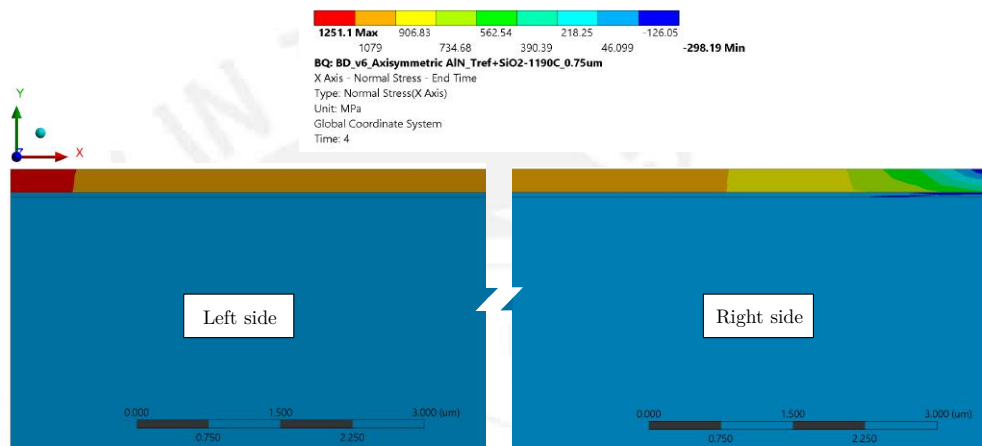


Figure 3.27.: Distribution of normal stresses oriented in x axis in MPa generated in the AIN axisymmetric model from the left to the right side of the model.

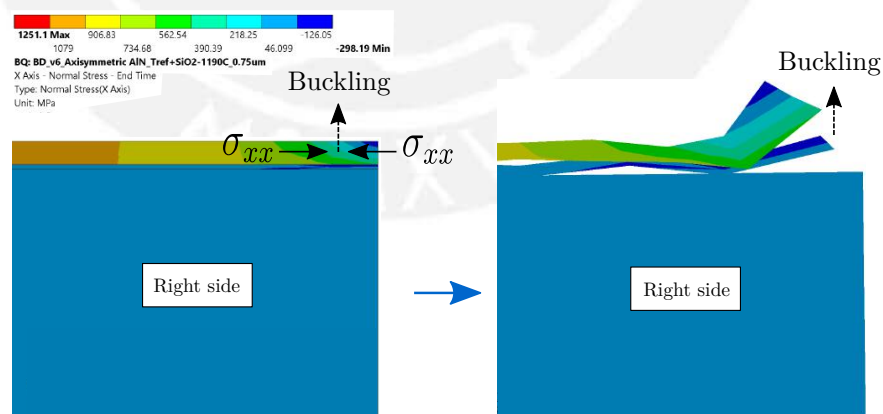


Figure 3.28.: Buckling delamination caused by the normal stresses in x axis (σ_{xx}) in the AIN section. Large-scale view to visualize the delamination.

- **MAX phase**

As mentioned above, the deposition of the Cr_2AlC thin film was represented by changing its reference temperature with APDL commands because it was heated to 600°C after being deposited at room temperature. Figure 3.29 shows the deformation along y-axis generated by this alternative, where the sections was deformed upward reaching maximum value of $-57\ \mu\text{m}$.

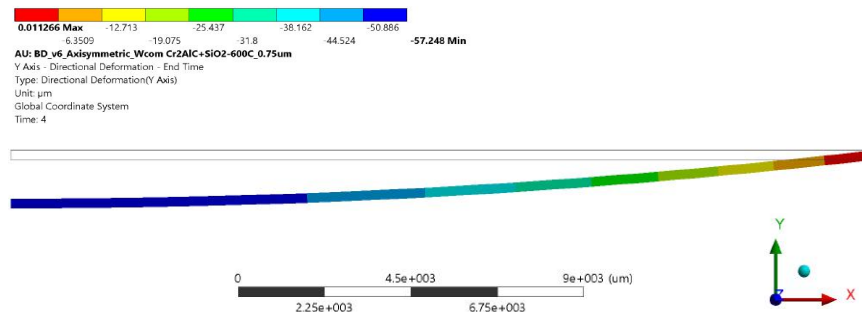


Figure 3.29.: Deformation along y axis (in μm) of the Cr_2AlC axisymmetric model by changing the temperature reference with APDL command.

Moreover, as seen in Figure 3.30, the higher residual stresses are generated in the thin film, where the stresses reach a maximum value of 822 MPa on the left side and decrease towards the right side. Therefore, as a result of the heat treatment, the maximum stresses are generated at the wafer center and decrease towards the wafer circumference. In addition, the stresses in the SiO_2 layer and substrate are lower, which vary from 0.38 MPa to 274.2 MPa.

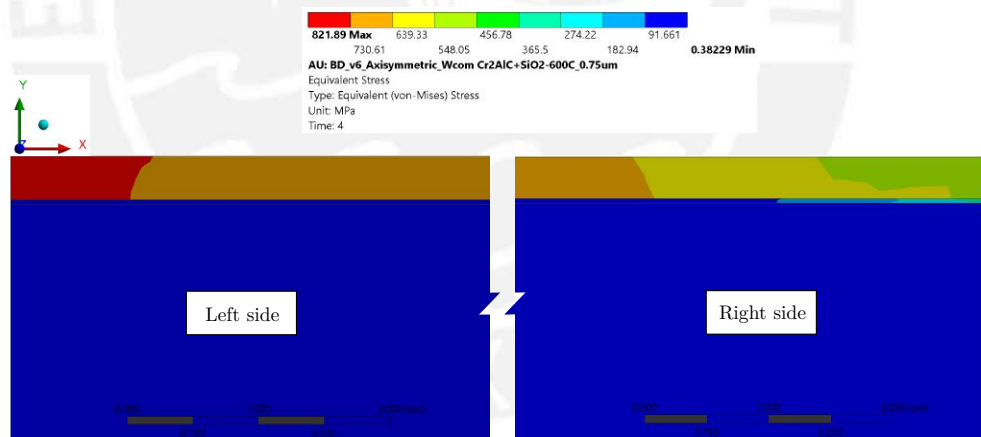


Figure 3.30.: Distribution of equivalent stresses (von Mises) in MPa generated in the Cr_2AlC axisymmetric model from the left to the right side of the model.

Besides, the axisymmetric model formed an upward concavity in order to compensate the moment in $-z$ direction. This, in turn, was generated by the difference of stresses between the thin film and the substrate and SiO_2 , which were oriented mainly along the $+x$ and $-x$ directions (see Figure 3.31). In addition,

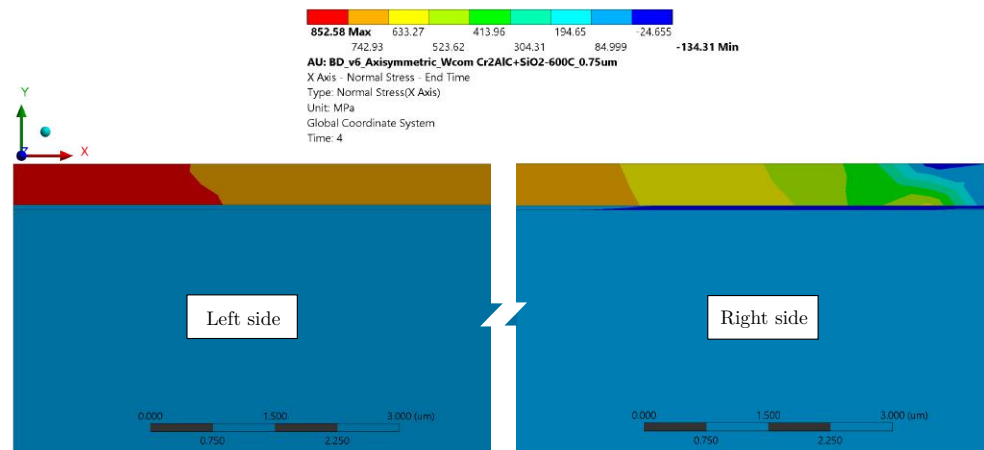


Figure 3.31.: Distribution of normal stresses oriented in x axis in MPa generated in the Cr_2AlC axisymmetric model from the left to the right side of the model.

the difference of the stresses in the thin film along the x-axis, lead to a buckling deformation (see Figure 3.32).

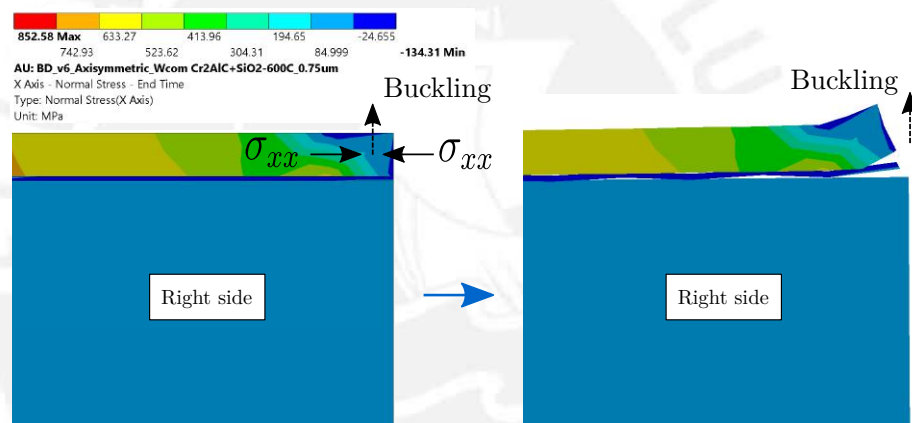


Figure 3.32.: Buckling delamination caused by the normal stresses in x axis (σ_{xx}) in the Cr_2AlC section. Buckling plotted on a larger scale to visualize it.

3.6.2. Axisymmetric simulation with initial curvature

The axisymmetric simulation exposed in 3.6.1 considered a flat wafer geometry, which differs from the measured data shown in Figure 3.25. Hence, with the purpose to improve the model and thus, visualize how the results vary in respect to the previous simulation, the initial curvature was added to the geometry. The initial curvature of the wafer was based on the scans along the x-axis, alike the estimation of the curvature radius, at the prior stage of the deposition of the thin films. As can be seen in Figure 3.25 (for another figures refer to Chapter 4), the measured deflections have a pronounced curvature near the coordinate $x = 20$ mm. Due to the coordinate system of the interferometer, the deflections vary from 631 mm to 642 mm for the AlN and from

626 mm to 635 mm for the Cr_2AlC . However, these values cannot be added directly to the geometrical model, since the model was built in the x-y plane in respect of the origin (see Figure 3.19). Therefore, the deflection at 20 mm in x-axis was chosen as a reference value to convert the deflections into data around zero, which can be added to the geometrical model. The results are shown in Figure 3.33.

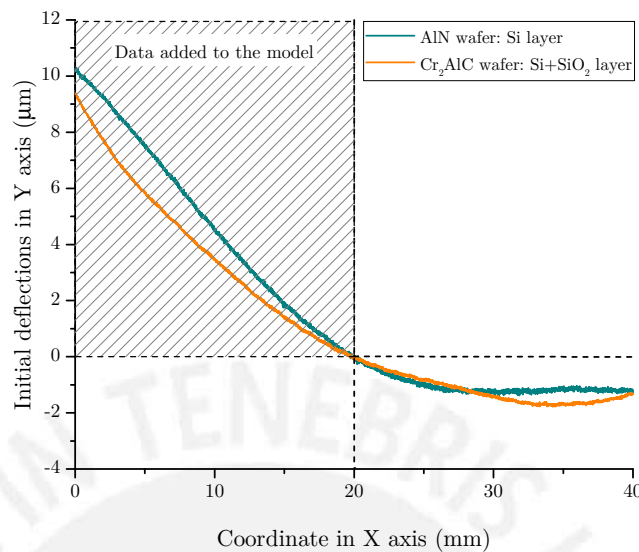


Figure 3.33.: Initial deflections of the aluminum nitride (dark cyan line) and Cr_2AlC (orange line) wafers. Data enclosed by the sparse-line rectangle were included to the geometry model.

Since the axisymmetric model considered a symmetric section regarding the y-axis, the initial curvature had to be also symmetric. For that reason, the present maximum deflection to the left and to the right of 20 mm was calculated in order to choose the values to be added to the model. Between 0 mm to 20 mm the maximum deflections were $10.25\ \mu\text{m}$ and $9.39\ \mu\text{m}$ for the AlN and Cr_2AlC respectively; whereas between 20 mm to 40 mm the maximum deflections were $1.19\ \mu\text{m}$ and $1.33\ \mu\text{m}$ for the AlN and Cr_2AlC respectively. Hence, the data between 0 mm to 20 mm in x-axis were included to the geometric model due to their higher deflections, which represented the most extreme case. Furthermore, since the real diameter of the wafer was 50 mm, the missing data were estimated by the corresponding regression equation.

3.6.2.1. Mesh

The mesh of the model was based on the methods described in 3.6.1.1. Nevertheless, the initial curvature added to the model caused the generation of irregular quadratic elements, which led to errors in the meshing particularly on the silicon dioxide and thin film layers. For this reason, the PLANE183 element type was selected in its triangular 6-node element variant (see Figure 3.34a) with the aim of meshing those thin layers. Alike the meshing in 3.6.1.1, sizing and meshing methods were included to discretize the geometry:

- Sizing methods: As in the previous mesh of the axisymmetric model, the elements sizes were equal to $125\ \mu\text{m}$ and $1\ \mu\text{m}$ for the substrate and silicon dioxide layer. Respect to the thin film, the element size was $0.8\ \mu\text{m}$.
- Meshing methods: Since the 6-node triangular variant of PLANE183 element type was selected, the Multizone Quad/Tri method was chosen with the mesh type All Tri.

As a result, triangular elements were generated in the silicon dioxide and thin film layers (see Figure 3.34b).

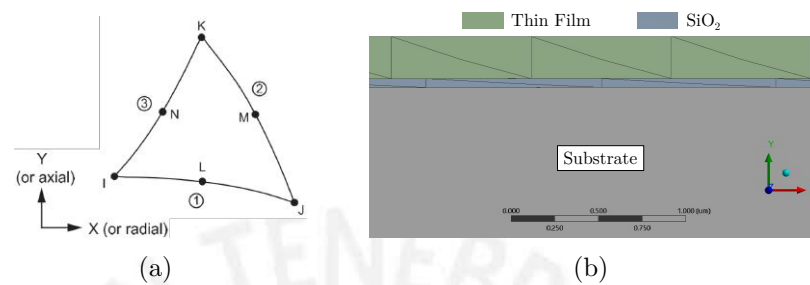


Figure 3.34.: Mesh of the axisymmetric section with initial curvature: (a) 6-node triangular variant of PLANE183 element type, Figure extracted from [67]; (b) Zoomed view of the triangular elements in the SiO_2 and thin film layers.

The parameters of the meshing are shown in Table 3.7.

Table 3.6.: Meshing parameters of the AlN and Cr_2AlC axisymmetric sections with initial curvature.

Parameter	AlN	Cr_2AlC
Nodes	339131	339131
Elements	112906	112906
Element quality (average)	0.294	0.455
Aspect ratio (average)	11.717	10.827
Skewness (average)	0.728	0.5792

3.6.2.2. Simulation

The supports, contact type, and thermal loads were the same of that of the flat-section axisymmetric simulation exposed in 3.6.1.2. In summary:

- Supports: Shown in Figure 3.21a, i.e. left edge fixed in x axis ($u_x = 0$) and bottom right vertex fixed in y axis ($u_y = 0$).
- Contact type: The contact was selected as bonded type among the three bodies.
- Thermal loads: They followed the temperature curves shown in Figure 3.21b.

3.6.2.3. Results

The methods for changing the reference temperature were as follows: the APDL commands for the Cr_2AlC and the ANSYS interface for the AlN (refer 3.6.1.3).

- **Aluminum nitride**

The deformation along y-axis is shown in Figure 3.35, where the section forms an upward concavity with a maximum deflection of $-35\ \mu\text{m}$ generated on the left side, i.e. at the center of the wafer.

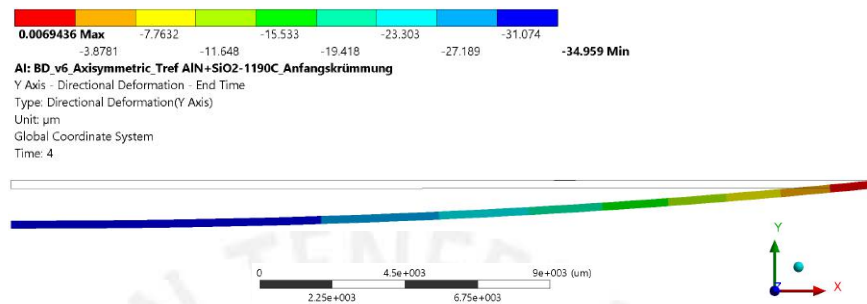


Figure 3.35.: Deformation along y axis (in μm) of the AlN axisymmetric model with initial curvature.

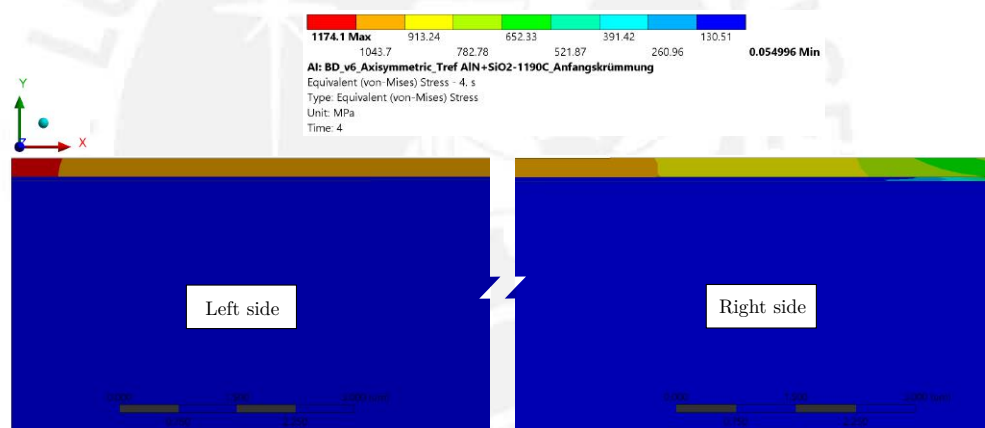


Figure 3.36.: Distribution of equivalent stresses (von Mises) in MPa generated in the AlN axisymmetric model, with initial curvature, from the left to the right side of the model.

On the other hand, Figure 3.36 depicts the distribution of the equivalent (von Mises) residual stresses in the section. As can be seen, the thin film withstands the higher stresses reaching a maximum value of 1174 MPa on the left side; while lower values are generated on the right side of the section. Regarding the silicon dioxide layer and substrate, they withstand lower stresses, which vary from 0.05 MPa to 391.4 MPa. Thus, extrapolating this results to the wafer, the stresses are the highest in the center and decrease towards its circumference.

Moreover, Figure 3.37 shows the distribution of the normal stresses oriented in x-axis. Alike the distribution of the equivalent stresses, the higher values are

generated in the thin film with a maximum value of 1235 MPa on the left side; while lower values are on the right side with a minimum value of -388 MPa. Hence, the stresses in the x-axis have the largest impact on the equivalent stresses calculation.

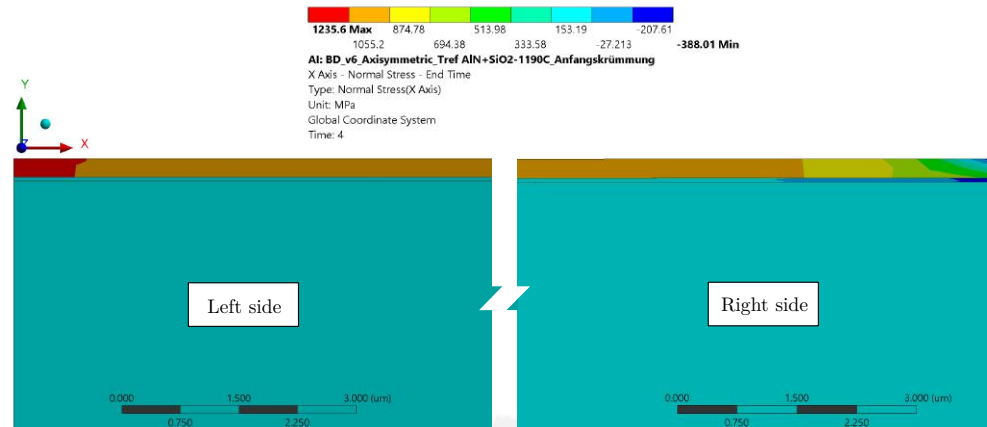


Figure 3.37.: Distribution of normal stresses oriented in x-axis in MPa generated in the AlN axisymmetric model, with initial curvature, from the left to the right side of the model.

- **MAX phase**

Figure 3.38 depicts the deformation along y-axis, where the section forms an upward concavity with a maximum deflection of -57 μm generated on the left side, i.e. at the center of the wafer.

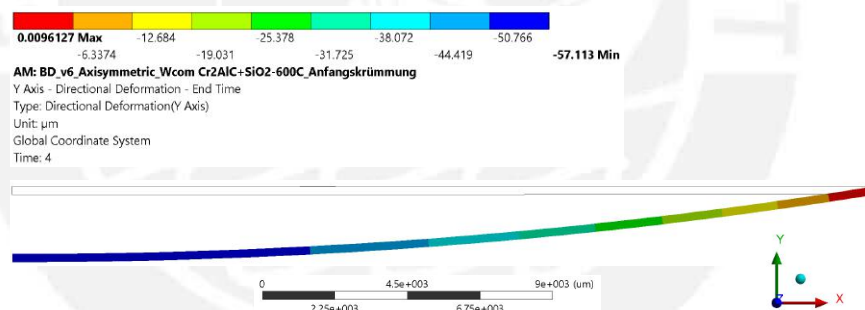


Figure 3.38.: Deformation along y axis (in μm) of the Cr_2AlC axisymmetric model with initial curvature.

Moreover, as noted in Figure 3.39, the thin film withstands the higher equivalent stresses reaching a maximum value of 813 MPa on the left side; whereas lower values are generated on the right side. In respect of the SiO_2 layer and substrate, they withstand lower stresses, which vary from 0.04 MPa to 271.5 MPa. Therefore, extrapolating this results to the wafer, the stresses are the highest in the center and decrease towards its circumference.

In addition, Figure 3.40 shows the distribution of the normal stresses oriented in x-axis. The stresses vary from -163 MPa to 840 MPa in the thin film; while -163 MPa to 59 MPa in the substrate and silicon dioxide layer.

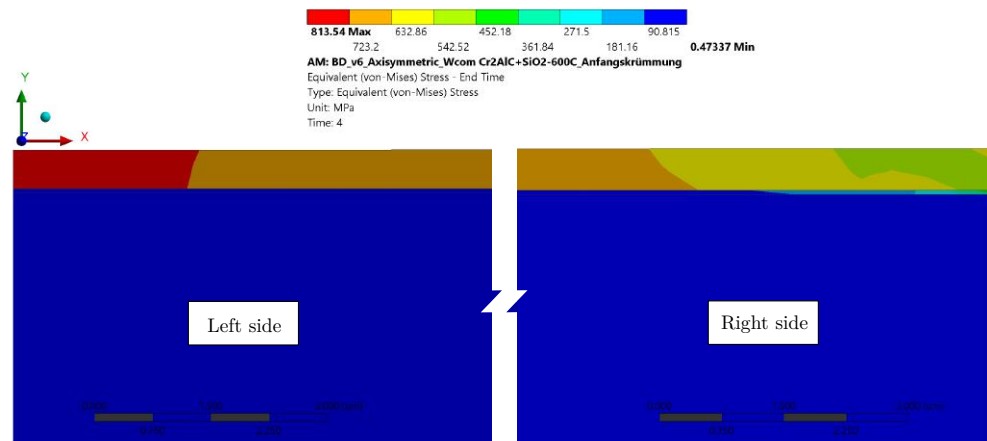


Figure 3.39.: Distribution of equivalent stresses (von Mises) in MPa generated in the Cr_2AlC axisymmetric model, with initial curvature, from the left to the right side of the model.

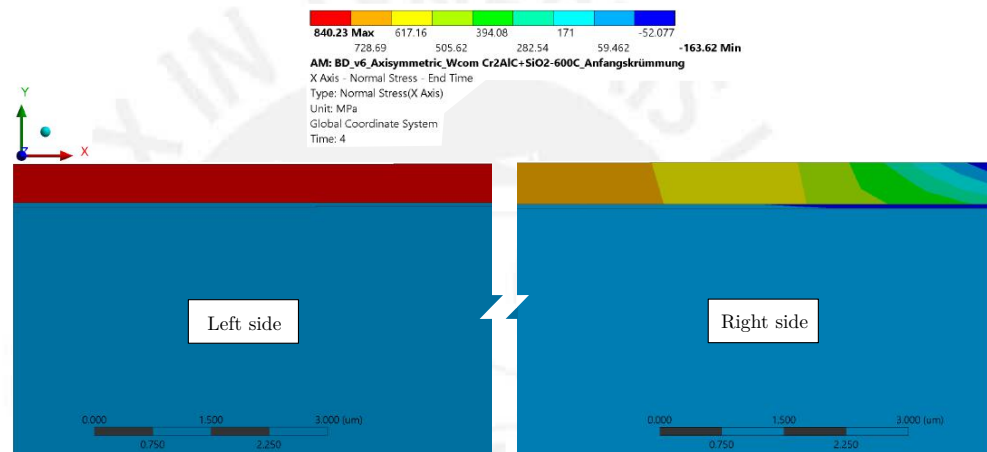


Figure 3.40.: Distribution of normal stresses oriented in x-axis in MPa generated in the Cr_2AlC axisymmetric model, with initial curvature, from the left to the right side of the model.

3.6.3. Quadrant simulation with initial curvature

This simulation was based on a quadrant geometry generated by the revolution of the axisymmetric geometry (see 3.6.2) respect to the y-axis.

3.6.3.1. Mesh

The element type was SOLID186 for the three layers (see Figure 3.10). Alike the previous simulations, sizing and meshing methods were taken into account.

- Sizing methods: Since the element size of the quadrants in simulation 1 was validated in subsection 3.5.3, the element size of the substrate was $300\ \mu\text{m}$, while for the silicon dioxide layer and thin film the element size was $200\ \mu\text{m}$.

- Meshing methods: Given that irregular elements were generated by the addition of the initial curvature, the Multizone patch independent method was included with the Hexa/Prism option activated in order to produce hexagonal and prismatic elements and thus, to ease the difficulties in meshing that the initial curvature addition may involve.

The parameters of the mesh are shown in Table 3.7.

Table 3.7.: Meshing parameters of the AlN and Cr₂AlC quadrant models with initial curvature.

Parameter	AlN	Cr ₂ AlC
Nodes	255533	221272
Elements	36122	31184
Element quality (average)	0.211	0.212
Aspect ratio (average)	1770	1560.5
Skewness (average)	2.459×10^{-2}	2.460×10^{-2}

3.6.3.2. Simulation

The boundary conditions added to this model were the following:

- Supports: Alike the quadrant model in simulation 1, the circular arc located in xz plane was limited in y axis (see Figure 3.11b).
- Contact type: Bonded type among the three bodies.
- Thermal loads: They followed the steps shown previously in Figure 3.21b.

Besides, the simulation of the AlN and Cr₂AlC quadrants used the change of the reference temperature by ANSYS Workbench and APDL command respectively.

3.6.3.3. Results

The deformation in y-axis for both quadrants are shown in Figure 3.41, where the maximum deflection occurred at the center reaching the following values: $-37.1 \mu\text{m}$ for the AlN and $-58.5 \mu\text{m}$ for the Cr₂AlC.

On the other hand, Figure 3.42 depicts the equivalent (von Mises) stresses. As can be seen, the higher values are generated in the thin film: $1077.5 \mu\text{m}$ for the AlN and $780.8 \mu\text{m}$ for the Cr₂AlC). Nevertheless, unlike the results obtained by simulations based on axisymmetric models, a stress distribution in the thin film cannot be seen. This could occur because the quality of the elements are lower than that of the axisymmetric models, e.g. the aspect ratios obtained in the quadrant models were 1770 and 1560 for the quadrant models (see Table 3.7), whereas 11 and 10 in the axisymmetric models (see Table 3.7).

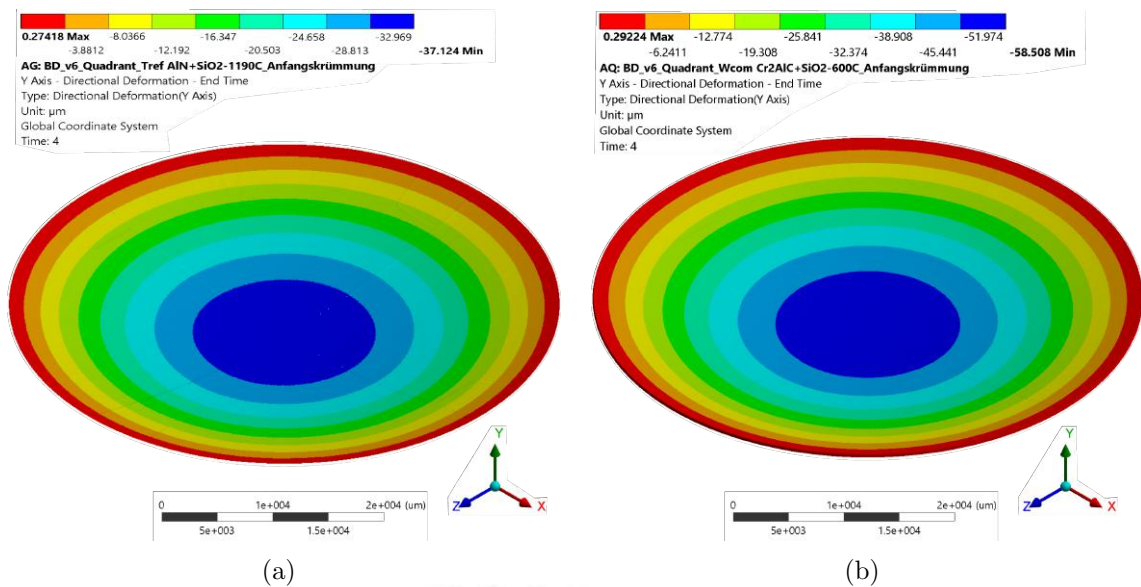


Figure 3.41.: Simulation 2 - Deformation in y-axis in μm : a) AlN, (b) Cr₂AlC.

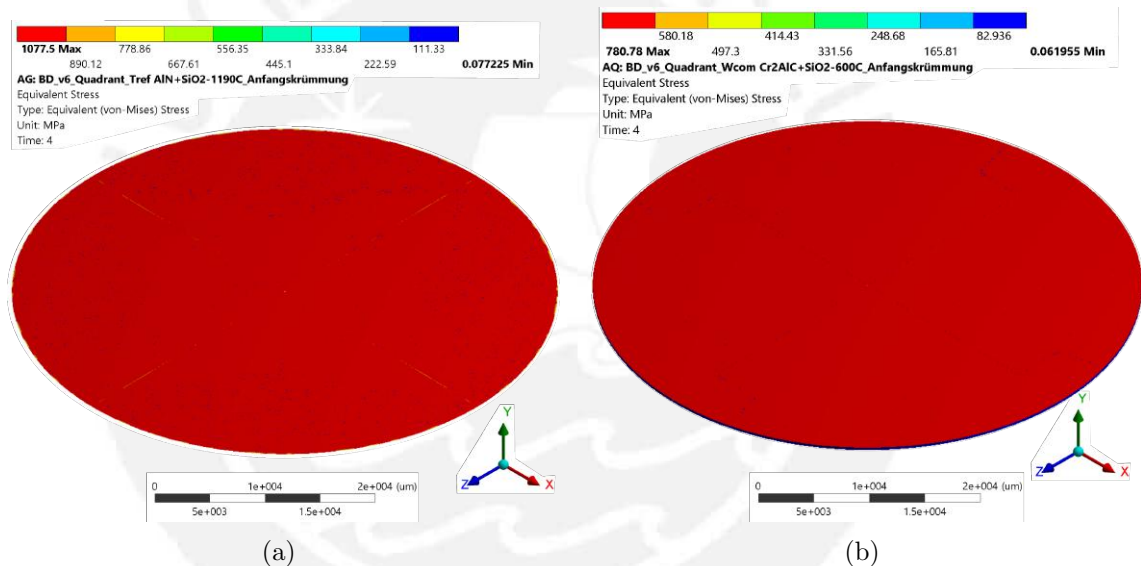


Figure 3.42.: Simulation 2 - Equivalent stresses (von Mises) in MPa: a) AlN, (b) Cr₂AlC.

3.7. Simulation 3 - Detection of the contact between SiO₂ and thin film

Unlike the previous simulations, where the bodies remained in the same position with their bonded contacts activated at different steps, in this simulation a different approach was proposed. It was applied firstly to the aluminum nitride circular plate. The stages followed by this simulation are depicted in Figure 3.43 and are as follows.

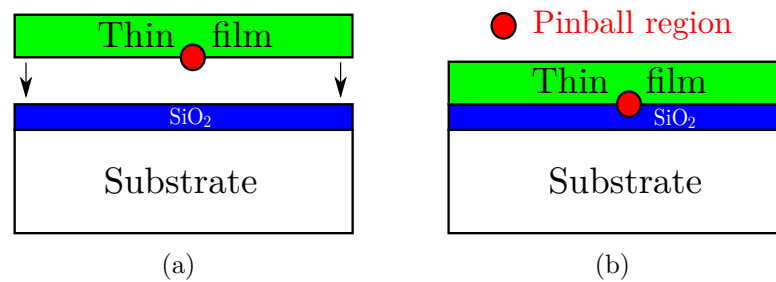


Figure 3.43.: Schematic representation of the contact detection: (a) At the beginning the bodies, i.e. thin film on the one hand and substrate-SiO₂ (marked in blue) body on the other, are separated, (b) By bringing the thin film together to the other body, the contact is detected because the SiO₂ layer is inside the pinball region (marked in red).

1. At the beginning, the thin film and the bilayer solid consisting of the substrate and silicon dioxide were separated. The contact type among the three layers was bonded (see Table 3.4); however, the formulation of the contact between the SiO₂ and the thin film was changed to Normal Lagrange with the pinball region option activated. That formulation was chosen because it considers the normal force F_n generated during the contact as a degree of freedom [70] and thus, the bonded contact could be included despite the gap between the bodies. Nevertheless, at this stage the contact should not be activated in order to approach the thin film to the bilayer body, otherwise, both bodies would move as a result of the thin film translation. For that reason, the pinball region (see Figure 3.44), i.e. a zone where the software considers if there is contact when the target body is located inside that [70], was selected. Its radius was equal to the SiO₂ thickness (50 nm) in order to set the contact only between the thin film and silicon dioxide layer. In this case, the bilayer body was selected as the target body.

Besides, the substrate-SiO₂ bilayer body was heated until the manufacturing temperature according, i.e. 1190 °C for the AlN and 600 °C for the Cr₂AlC, to room temperature.

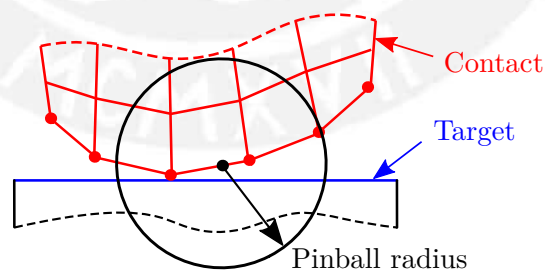


Figure 3.44.: Schematic view of the pinball radius. The contact is activated by the software if the target body is located inside the pinball region. Figure redrawn from [76].

2. The thin film was approached to the bilayer body (target body) until silicon dioxide layer is located inside the pinball region.

- The thin film remained in contact with the bilayer solid. The three bodies were cooled from their deposition temperature to room temperature.

3.7.1. Mesh

The geometric models considered in this simulation were the circular plates instead of the quadrants in order to

- Sizing methods: Due to the higher volume, the element size were bigger than that of the quadrant models. It was chosen as the maximum value from which a meshing was satisfactorily generated by the ANSYS meshing algorithms. Hence, the element size for the three layers was 700 μm and thus, the meshing had the parameters shown in Table 3.8.

Table 3.8.: Meshing parameters of the AlN circular plate.

Parameter	AlN
Nodes	76826
Elements	19920
Element quality (average)	0.263
Aspect ratio (average)	3387.9
Skewness (average)	0.507

3.7.2. Simulation

The stages described previously were included as four steps as follows:

- Step 1: The surface in contact with the thin film and the lateral faces of the bilayer body (see Figure 3.45a) were fixed on x and z-axes (see Table 3.9), i.e. $u_x = u_z = 0$ (see Figure 3.45a); whereas the thin film body was placed at a distance of 2 mm from the bilayer body. Besides, the bilayer body was heated to the deposition temperature of the thin film (see Figure Figure 3.45b).
- Step 2: The thin film solid was brought together to the bilayer body in order to activate the contact between them, whereas the fixations in step 1 were kept. Moreover, the bodies were at the deposition temperature.

Table 3.9.: Boundary conditions in Simulation 3: Supports applied step by step.

Step	Faces		Thin film	Bottom edge
	u_x (μm)	u_z (μm)	u_y (μm)	u_y (μm)
1	0	0	0	Inactive
2	0	0	-2000	Inactive
3	0	0	-2000	Inactive
4		Inactive		0

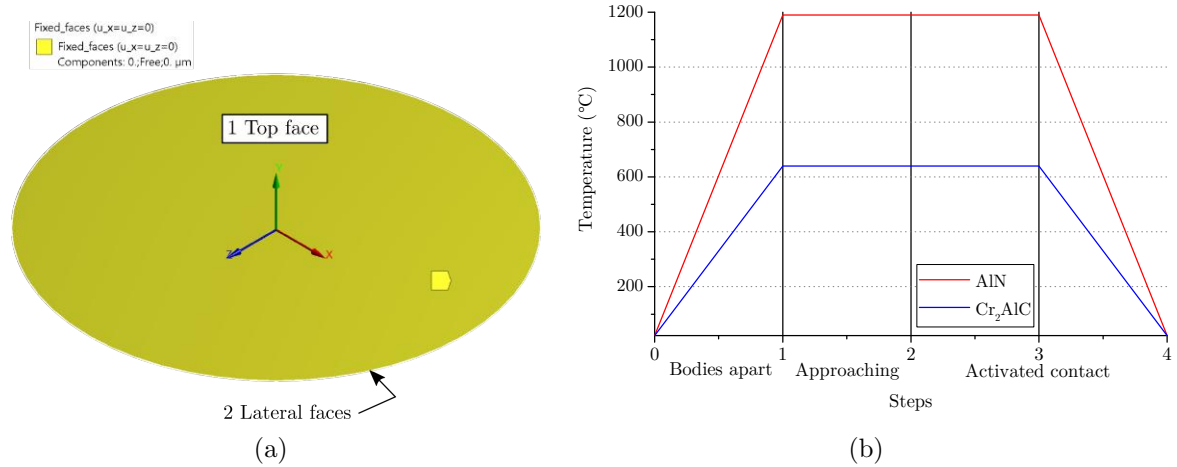


Figure 3.45.: Boundary conditions in Simulation 3: (a) Faces of the bilayer solid fixed on x and z axes, (b) Step-by-step detail.

3. Step 3: The faces fixation was kept and the thin film remained in contact with the bilayer body. Besides, the three bodies were at the deposition temperature.
4. Step 4: The limitation in displacement applied in steps 1, 2 and 3 was withdrawn, while the bottom edge of the bilayer body was fixed on y-axis with the aim of enabling the deformation of the wafer. The three bodies were cooled to 22 °C.

Furthermore, the option *Large deflection* was activated during the simulation due to the translation of the thin film.

3.7.3. Results

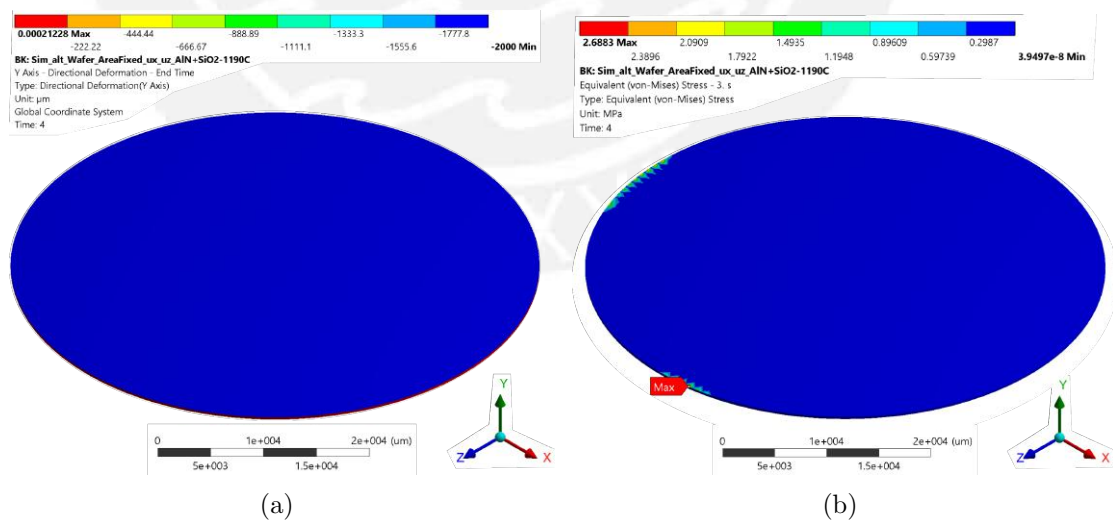


Figure 3.46.: Simulation 3 results: (a) Deformations along the y-axis, (b) Residual stresses at room temperature.

The results are shown in Figure 3.46. Regarding the residual stresses, a maximum value of 2.68 MPa was generated in the thin film, which was much less than the results of simulation 2. This could have been generated by the contact surface fixation, which only allowed deformations along the y-axis of the bilayer body. This can be seen in Figure 3.47, where the top surface, which is contact with the thin film, deformed along the y-axis only $0.0001\ \mu\text{m}$, while the bottom surface deformed $2.306\ \mu\text{m}$ along the -y direction. In this manner, when the bodies were cooled and the fixations were withdrawn, the bottom surface returned to its initial position and thus, the thermal load was not transmitted to the thin film leading to low residual stresses.

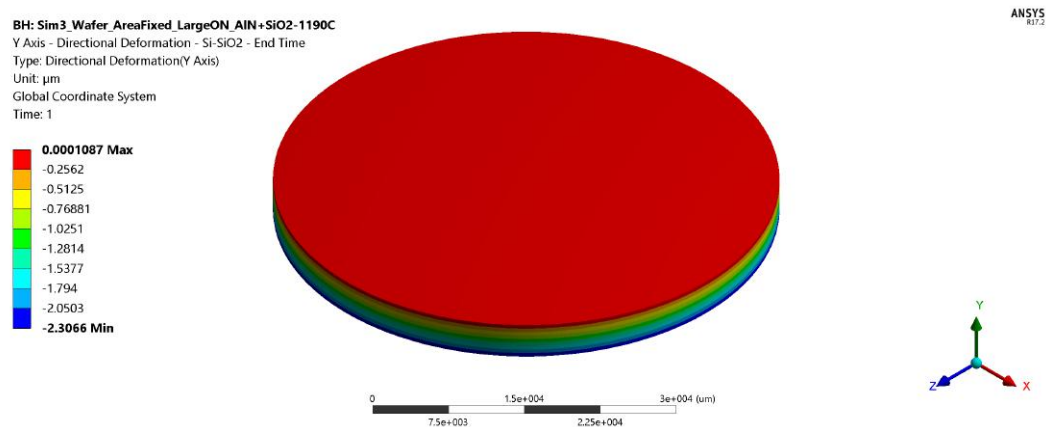


Figure 3.47.: Simulation 3 - Deformations along the y-axis of the substrate-SiO₂ body. Note that the plot scale was increased to visualize the deformation of the bottom surface.

3.8. Observations

3.8.1. Killing contact

Apart from the simulations exposed above, another with birth and death commands was carried out. Nevertheless, in this case, the commands were applied to deactivate not only the thin film but also the contact between the silicon dioxide and the thin film. The steps were based on simulation 2 (see subsection 3.6) as follows:

- Step 1: Heating the substrate and SiO₂ to the corresponding process temperature, while the thin film body was killed with the command `ekill`. Besides, the thin-film-SiO₂ contact was also killed. It was done by tagging the contact and target elements, named in ANSYS Workbench² as `cid` and `tid` respectively, with the commands `mycont=cid` and `mytarg=tid`. Then, both elements were selected with `esel,a,type,mycont` and `esel,a,type,mytarg` to be killed with `ekill,all`.

²<http://www.padtinc.com/blog/the-focus/utilizing-element-birth-and-death-for-contact-elements-in-workbench-mechanical> (visited on 15/03/17)

- Step 2: Bodies kept at the process temperature.
- Step 3: Thin film and contact were selected with the APDL commands `esel, s, mat,,part1, esel, a, type, mytarg` and `esel, a, type, mycont` and then activated with `ealive, all`.

The temperature of the three bodies dropped to room temperature.

- Step 4: Bodies kept at room temperature.

The meshing and body supports were the same in simulation 2. The results are shown in Figures 3.48 and 3.49 for the AlN.

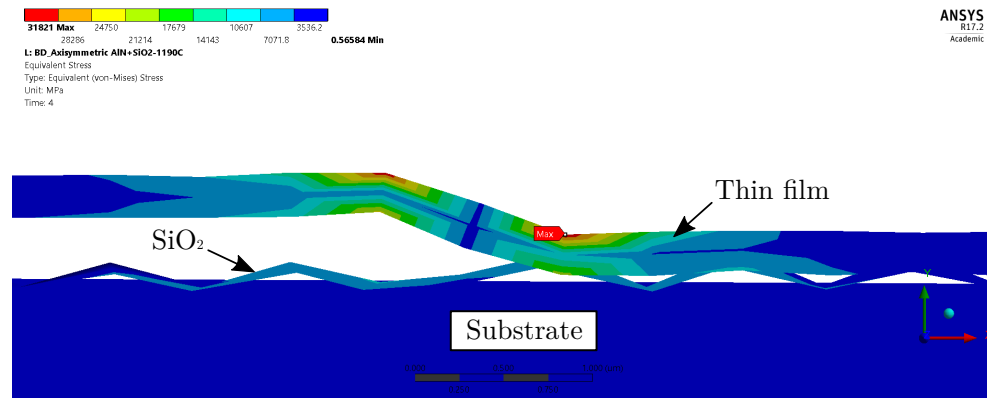


Figure 3.48.: Residual stresses generated when the contact between the thin film and SiO₂ layer was born. Zoomed view of the delamination zone.

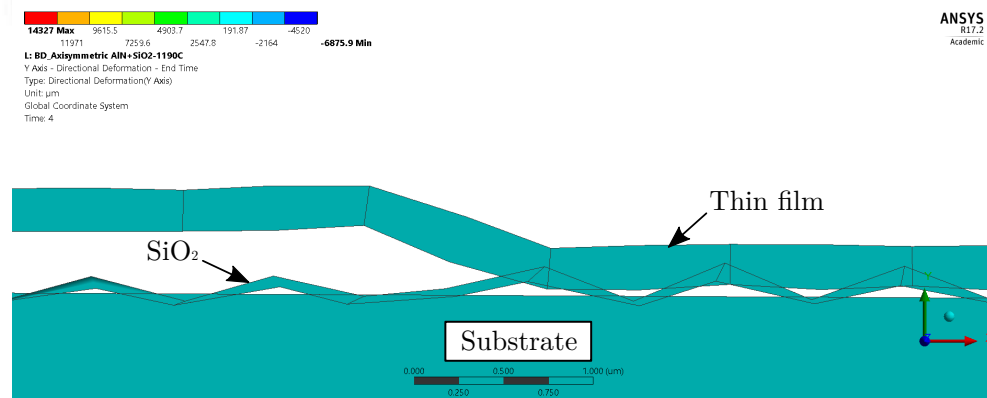


Figure 3.49.: Deformation in y-axis generated when the contact between the thin film and SiO₂ layer was born. Zoomed view of the delamination zone.

As can be seen in Figure 3.48 delaminations occurred in the silicon dioxide and thin film layers leading to high residual stresses, e.g. 31 821 MPa in AlN layer. Those detachments were caused mainly by the abrupt change of the contact status from step 2 to step 3, where the contact was activated. Since the birth and death technique reduces the stiffness matrix of the killed element (see subsection 3.6), that body remains geometrically in the model and thus, the contact that unites it with the entire model

must be active. Hence, the absence of that contact disrupted the simulation results as follows: generated a rough 0.5 μm gap between the thin film and silicon dioxide layer at step 2 (see Figure 3.50a), which was increased in the subsequent steps leading to a maximum deformation of 14 327 μm (see Figure 3.50b).

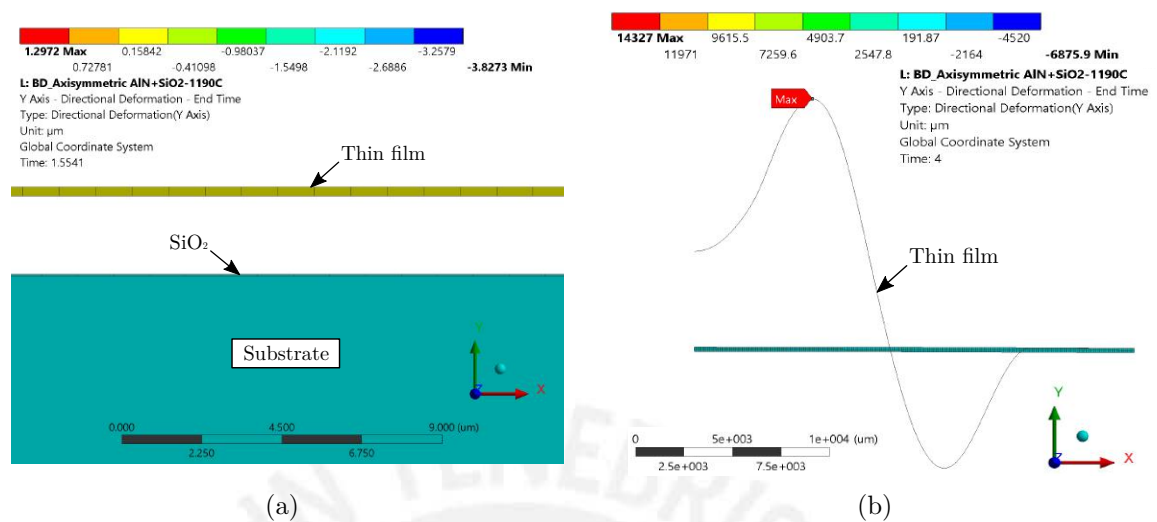


Figure 3.50.: Deformation in y-axis: (a) At step 2, i.e. with a non-active contact between SiO_2 and thin film, (b) At step 4.

Even though this approach could not simulate properly the residual stresses, since the reached values were very different from the ones obtained in 4.1, it allowed to visualize the layers behavior if the contact was lost during the manufacturing process. This can be caused, for instance, by a drop of the thin film deposition ratio, inter alia.

3.8.2. Simulation 3

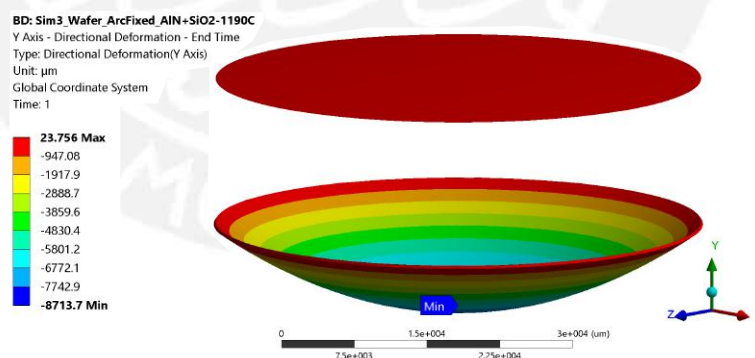


Figure 3.51.: Deformation along y-axis of the bilayer body after reaching the deposition temperature at 1190 $^{\circ}\text{C}$. Since the support was applied only to the perimeter edge of the bilayer body, a high deformation of 8713.7 μm was obtained.

In section 3.7, three faces of the bilayer body were fixed in simulation before the cooling step. Otherwise, due to the high temperature (1190 $^{\circ}\text{C}$), the circular plate would have

high deformations in its center (see Figure 3.51), if only the perimeter edges were limited. This occurred because the plate deforms due to the thermal load and a lack of displacement restriction.

On the other hand, simulation 3 were planned initially to have three steps with no supports at the third step. The process was the following:

1. Step 1: The surface in contact with the thin film and the lateral faces of the bilayer body (see Figure 3.52a) were fixed on *all axes*, i.e. $u_x = u_y = u_z = 0$ (see Table 3.10), unlike the first step shown in 3.7.2. The bilayer body was heated to the deposition temperature (see Figure 3.52b).

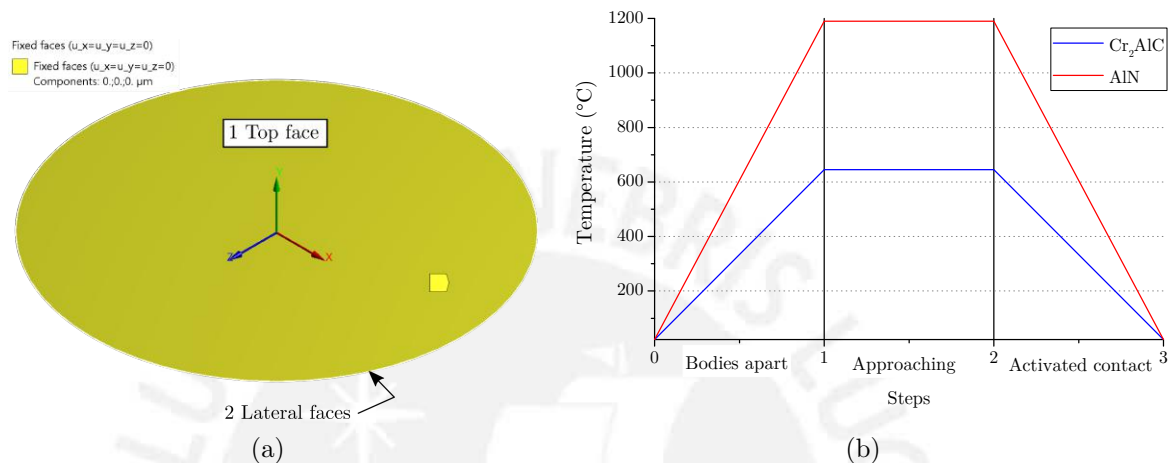


Figure 3.52.: Boundary conditions: (a) Faces fixed in the bilayer solid, (b) Temperature curve applied step by step.

2. Step 2: The thin film solid was brought together to the bilayer body in order to activate the contact between them. The bilayer body was kept at the deposition temperature.
3. Step 3: The limitation in displacement shown in step 1 was withdrawn with the aim of enabling the deformation of the plate.

Table 3.10.: Supports applied step by step.

Step	Areas			Thin film
	u_x (μm)	u_y (μm)	u_z (μm)	u_y (μm)
1	0	0	0	0
2	0	0	0	-2000
3	Inactive			

Nevertheless, ANSYS did not found a solution since the model had highly distorted elements at the third step. This could have been caused because the wafer deformed freely without any support at that step and thus, the iterations performed by the software could not converge.

On the other hand, as can be seen in Figure 3.22, the element size has a major influence on the solution. For that reason, the element size selected for the wafers ($700\ \mu\text{m}$) could not be the right for this simulation, e.g. it had a high aspect ratio of 3387.9 (see Table 3.8). However, in this case, that element size was selected by changing its value until the software could generate successfully the mesh of the wafer. Hence, the usage of a more computing power could lead to the generation of a finer mesh and thus, to find a solution.



Comparison with experimental values

4.1. Wafer curvature measurements

With the aim of applying this method, described in 2.5.2.1, wafers were fabricated under the preparation processes described in 3.2 with thin film thicknesses of 240 nm and 500 nm for the AlN and Cr₂AlC respectively (for other dimensions see Table 3.1). For estimating the curvature radius, wafer deflections scans after each layer deposition were performed along the x- and z-axis by a white-light interferometer. The results are shown in Figures 4.1a, 4.1b, 4.2a and 4.2b.

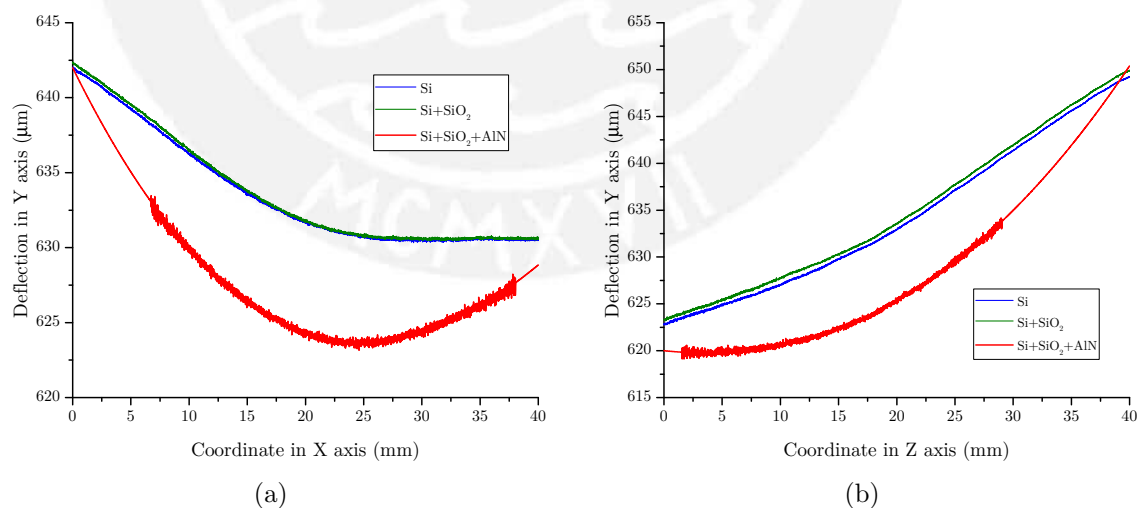


Figure 4.1.: Deflection scans of the AlN wafer with only the substrate (Si) layer, after the SiO₂ layer deposition (green marks) and after the AlN layer deposition (red marks): (a) Along the x-axis, (b) Along the z-axis.

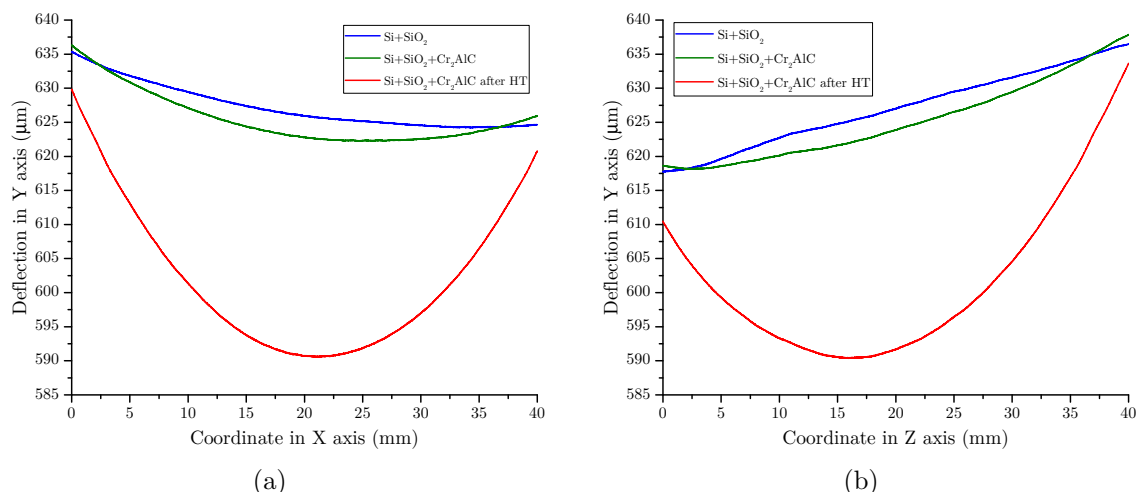


Figure 4.2.: Deflection scans of the Cr₂AlC wafer after the SiO₂ deposition (blue marks), after the Cr₂AlC layer deposition (green marks) and after the heat treatment (red marks): (a) Along the x-axis, (b) Along the z-axis.

Furthermore, the scans were performed only for 40 mm, despite the diameter of the wafer (50 mm), owing to limitations of the interferometer software. Besides, the continuous lines of the deflections after the AlN layer deposition in Figures 4.1a and 4.1b were estimated by a regression fitting procedure due to the presence of data located on the left and right (see Figures 4.3a and 4.3b) that could alter the curvature estimation. The procedure is explained in Appendix A.

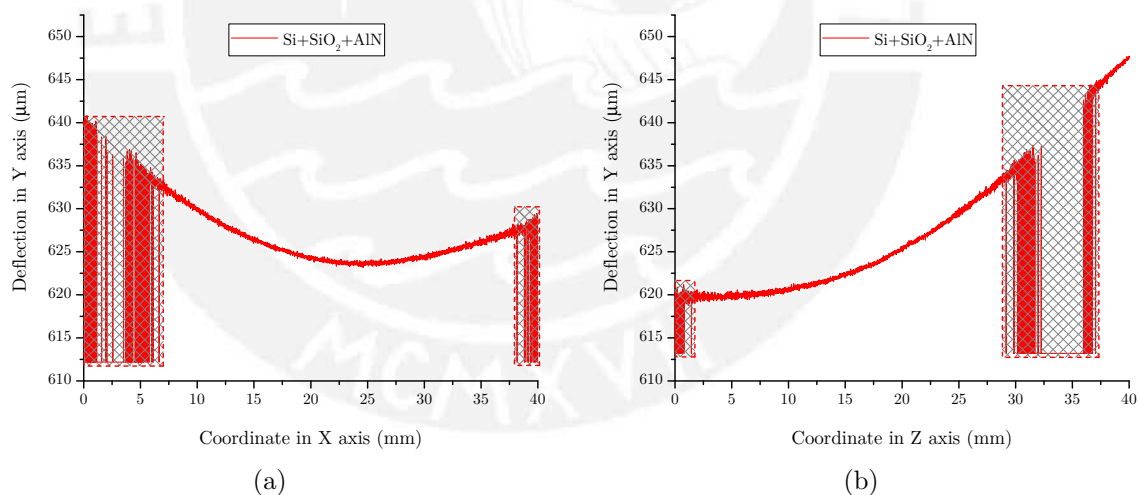


Figure 4.3.: Deflection scans with wrong data measured on the left and right, enclosed by two meshed rectangles. Data taken after AlN layer deposition: (a) Along x-axis, (b) Along z-axis.

$$\rho = \frac{(1 + (f'(x))^2)^{3/2}}{|f''(x)|} \quad (4.1)$$

Since the residual stress formulas require mainly the curvature radius, this parameter was calculated with Equation 4.1, where $f(x)$ is the equation of a plane curve [77]. For that purpose, the equations of each curve shown in the previous figures were estimated by regression fitting according to the following procedure:

- Match the units of measure of abscissa and ordinate. Since the stress unit in SI is MPa, the deflections in y-axis were converted in millimeters.
- Apply a polynomial fitting using the software OriginPro 2016. The polynomial order was varied until the regression values were close to the data. This was achieved by maintaining the R-square and the residual sum of squares higher to 0.998 and lower to 1.5×10^{-4} respectively. According to OriginLab¹, the R-squared parameter indicates how the fitted data explains the variability of the observed data around its mean, whereas the residual sum of squares is the sum of the square deviation between the fitted and the observed data. Hence, the higher the value of the R-squared, the closer the fitted data to the observed data, while the smaller the residual sum of squares, the better is the polynomial fitting.
- Calculate the curvature radius with Equation 4.1.

Figure 4.4 and 4.5 depict the data scan along x-axis after the AlN layer deposition and after the heat treatment of Cr₂AlC respectively with their fourth order fitting polynomials. For smaller orders, the parameters, i.e. R-squared and the residual sum of squares, were outside the limits set previously. On the other hand, even though for higher polynomial orders the parameters met the limits, it would hamper unnecessarily the radius curvature estimation and thus, the fourth order was chosen. The 4th order fitting polynomial for these curves are the following:

$$\delta_{y_AlN} = 0.642 - 0.002x + 3.532 \times 10^{-5}x^2 - 5.926 \times 10^{-8}x^3 - 1.497 \times 10^{-9}x^4 \quad (4.2)$$

$$\delta_{y_Cr_2AlC} = 0.630 - 0.004x + 1.06 \times 10^{-4}x^2 - 7.241 \times 10^{-7}x^3 + 8.373 \times 10^{-9}x^4 \quad (4.3)$$

Then the curvature radiuses were estimated with Equations 4.1, 4.2 and 4.3. The fitting polynomials for the other curves as well as their function δ_y are shown in Appendices B.1 and B.2. According to the residual stress formulas explained in 2.5.1, Hsueh's and Stoney's formulas permit to calculate the residual stress for multilayer deposition. Nevertheless, the Hsueh equation was not used because it requires the curvature radii of each layer at each step to calculate the corresponding residual stress, which for this work were not measured. Hence, the Stoney equation for multilayer structures according to Guo et al. [54] was employed. Since Equations 2.22 and 2.23 require isotropic mechanical properties, the anisotropic properties of the substrate, SiO₂, AlN and Cr₂AlC were converted into one value through the Voigt Equations 2.1, 2.2 and 2.3. The results are shown in Table 4.1.

¹http://www.originlab.com/doc/Origin-Help/Regression_Results (visited on 10/03/17)

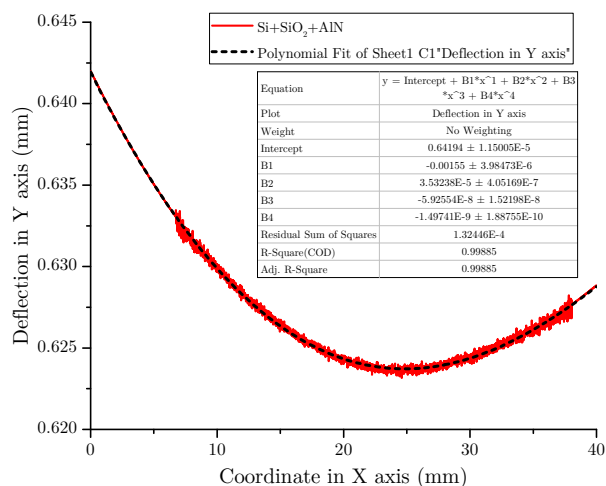


Figure 4.4.: Data scan along x-axis after the AlN layer deposition (red line) and fourth order fitting polynomial (black dash-line). Polynomial parameters, R-squared and residual sum of squares shown in embedded table.

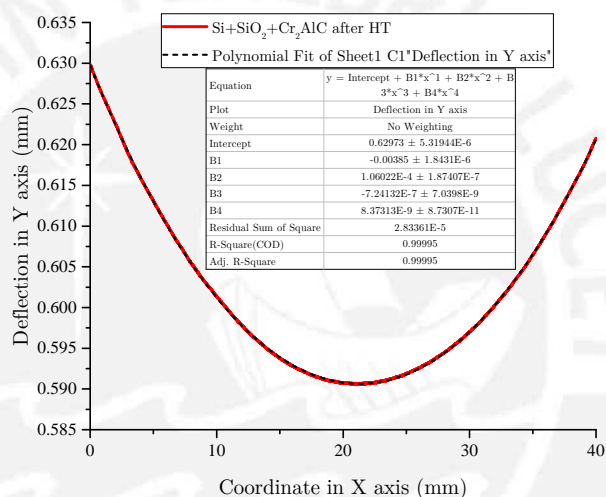


Figure 4.5.: Data scan along x-axis after the heat treatment once the Cr_2AlC was deposited (red line) and fourth order fitting polynomial (black dash-line). Polynomial parameters, R-squared and residual sum of squares shown in embedded table.

Table 4.1.: Mechanical properties obtained by the Voigt relations.

	Silicon	AlN	Cr_2AlC	SiO_2
E_V (MPa)	140490	294540	350580	80000
ν	0.2353	0.2566	0.1971	0.1850

According to the assumptions considered by Guo et al. [54], the Young's modulus and Poisson's ratio of the films are equal to that of substrate, which in this case was not met as it can be seen in Table 4.1. For that reason, those parameters were considered equal

to the mean value between the substrate and the thin film. Note that the mechanical properties of the silicon dioxide were disregarded due to their lower values compared to the other materials. Furthermore, the estimation of the curvature radius considered the scans along x axis (Figures 4.1a and 4.2a) because those data had a higher concavity unlike the scans in z axis (Figures 4.1b and 4.2b). Those parameters as well as the substrate and layer thicknesses were replaced in Equations 2.22 and 2.23 to calculate the residual stresses after each layer deposition. The results are shown in Figure 4.6 for the aluminum nitride and Figure 4.7 for the Cr_2AlC .

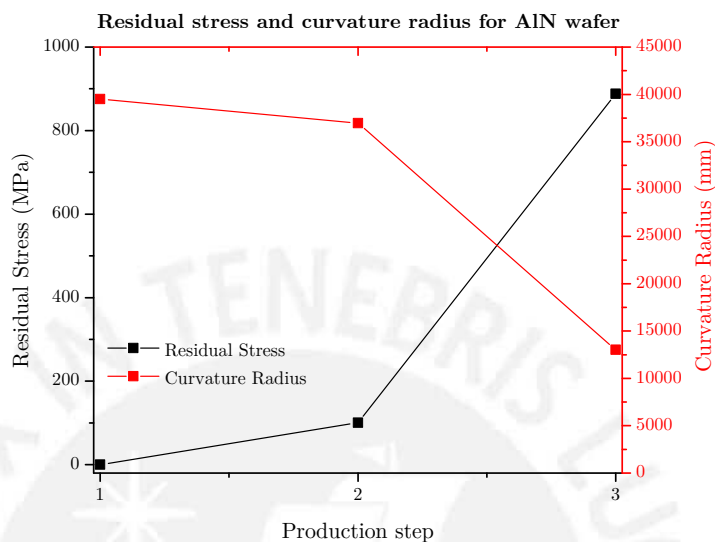


Figure 4.6.: Residual stress (black marks) and curvature radius (red marks) after each fabrication step for the AlN wafer. Note that the lines are not values, but are connecting lines among values.

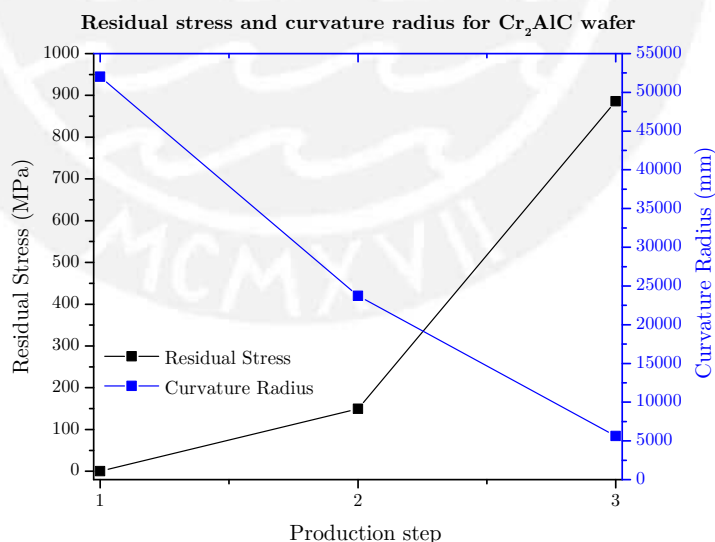


Figure 4.7.: Residual stress (black marks) and curvature radius (blue marks) after each fabrication step for the Cr_2AlC wafer. Note that the lines are not values, but are connecting lines among values.

4.2. XRD measurements

The measured diffractograms (black marks) are shown in Figures 4.8 and 4.9 for the AlN and Cr₂AlC wafers respectively. As can be seen in 2.5.2.2, the value of the Full Width at Half Maximum (FWHM) is required to calculate the residual stress with Equation 2.40 because its value is affected by the latter. Hence, the diffractograms were fitted by the Rietveld refinement (red marks), calculated by the software TOPAS, with the aim of measuring the FWHM, noted as β in Equation 2.40.

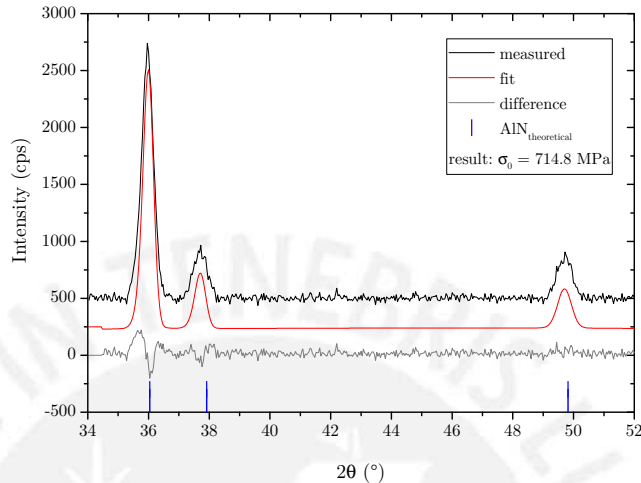


Figure 4.8.: Measured diffractogram of the AlN wafer. The average residual stress ($\sigma_0 = 714.8$ MPa) is calculated from the measured curve (black marks), Rietveld fitting curve (red marks) and theoretical position (blue marks).

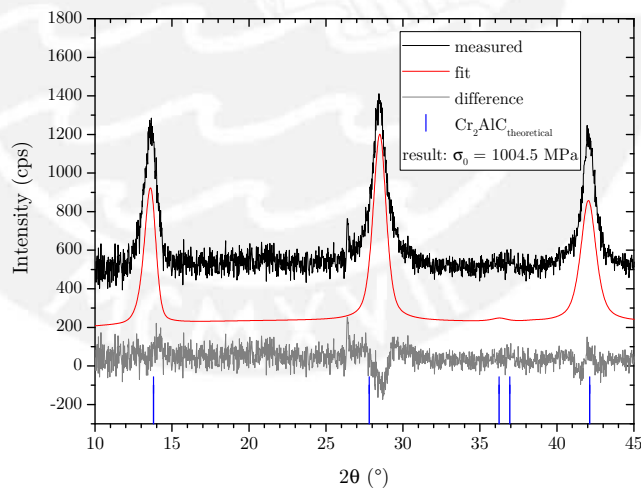


Figure 4.9.: Measured diffractogram of the Cr₂AlC wafer. The average residual stress ($\sigma_0 = 1004.5$ MPa) is calculated from the measured curve (black marks), Rietveld fitting curve (red marks) and theoretical position (blue marks).

As a result, the average residual stress is 714.8 MPa (AlN wafer) and 1004.5 MPa (Cr₂AlC wafer).

4.3. Discussion

4.3.1. Residual stresses

A visual comparison between the residual stresses obtained by the simulations, described in Chapter 3, and the experimental results is shown in Figure 4.10.

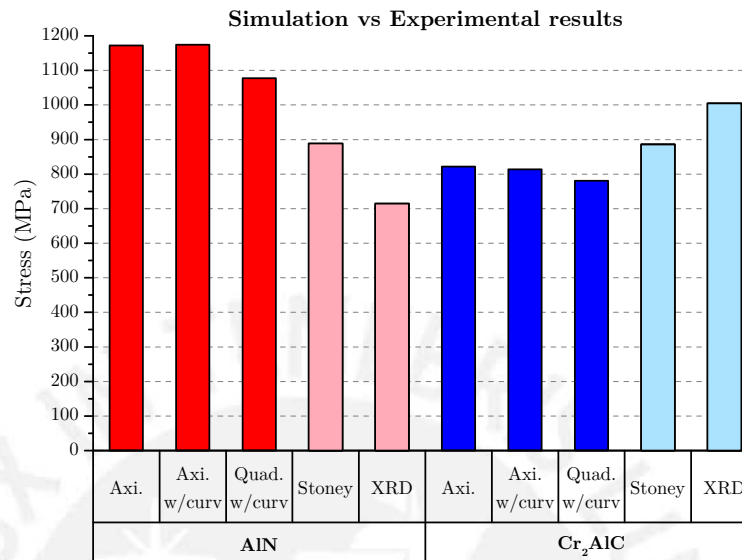


Figure 4.10.: Equivalent residual stresses obtained by simulations (blue and red columns), i.e. Axisymmetric (Axi.), Axisymmetric with initial curvature (Axi. w/curv), Quadrant with initial curvature (Quad. w/curv) compared with experimental results (pale blue and red columns), i.e. Stoney equation, according to Guo et al. [54], and XRD measurements.

Regarding the residual stresses in the AlN wafer, a descending trend from the axisymmetric model to the XRD measurement is observed. The simulated residual stresses (red columns) obtained by the flat and curved axisymmetric models were almost equal (1172.1 MPa and 1174.1 MPa respectively), which indicates a low influence of the curvature on the axisymmetric model results. This, in addition to their deviation from the experimental results, could have been caused by the geometric simplification, i.e. a two-dimensional section extracted from a three-dimensional solid. Since the section must be in the xy plane, the software disregarded the anisotropic properties of the materials oriented in z-axis during the processing stage.

On the contrary, the residual stress simulated considering a curved quadrant model reached a value (1077.5 MPa) closer to the experimental results (pale red columns). Even though the mesh of the quadrant has not high quality elements, and therefore a stress distribution cannot be displayed, this three-dimensional model enables the software to consider the anisotropic properties of each body. For that reason, it can be asserted that a simulation based on a three-dimensional wafer with high quality elements could provide better results.

Furthermore, the difference between the stress calculated by the Stoney equation (888.2 MPa) based on wafer curvature scannings, according to Guo et al. [54], and the XRD measurement (714.8 MPa) permits to see the extent of each technique. Since the Stoney equation estimates type I stresses, while the XRD technique permits to estimate the residual stress types I and II, that difference would show that the type II stresses reduces the macroscopic stresses.

Likewise, the residual stresses in the Cr_2AlC wafer show a trend, but in this case an ascending one. The stresses simulated (blue columns) with the flat and curved axisymmetric model are similar (813.5 MPa and 780.8 MPa respectively), which depicts the low impact of the initial curvature on the results obtained with an axisymmetric section by the reasons above mentioned.

Besides, the equivalent stresses simulated with a curved quadrant model reached a value of 780.8 MPa lower than that calculated with experimental results (pale blue columns). Since the annealing process of the Cr_2AlC wafer was deemed as a single cooling step, the microstructural stresses could not be represented in the simulation. Therefore, the simulation results do not include those stresses and thus, are lower than the XRD stress (1004.5 MPa).

For both materials, the proximity of the simulated values to that calculated by the Stoney equation describes that the simulations performed in this work allow representing mainly the type I.

4.3.2. Deflection of the wafer

Since the initial curvature added to the models was considered as the deflection from 0 mm to 20 mm along the x-axis (see Figure 3.33), the simulated results were compared with the wafers generated by the deflection measurements in that range. The considered data were that measured at room temperature after the deposition of the AlN thin film and after the heat treatment for the Cr_2AlC wafer. Note that the missing data were estimated by the corresponding regression equation. Besides, since the simulations based on the quadrant model enabled to include the anisotropic properties of the material, their results were chosen in this comparison.

The deflections of the AlN wafer are shown in Figure 4.11. As can be seen, the deflections occur along -y-axis and rise from the circumference to the center, where a maximum deflection of 61.2 μm was reached in the deflection measurements (Figure 4.11a), while a maximum value of 56.5 μm in the simulation (Figure 4.11b). From Figures 4.1 and 4.6, it can be observed that higher the deflection, lower the curvature radius is. Therefore, the difference between the maximum values indicates that the curvature radius of the wafer is higher than that of the simulations. Thus, the residual stress existing in the AlN wafer is less than the simulated ones because the residual stresses are inversely proportional to the curvature radius (see Equations in 2.5.1). The latter is consistent with the results shown in Figure 4.10, where the red columns (simulated stresses) are higher than the pale red columns (measured stresses).

On the other hand, the deflections of the Cr_2AlC wafer are shown in Figure 4.12. Alike the AlN wafers, the deflections occurred oriented in -y-axis reaching at the center a

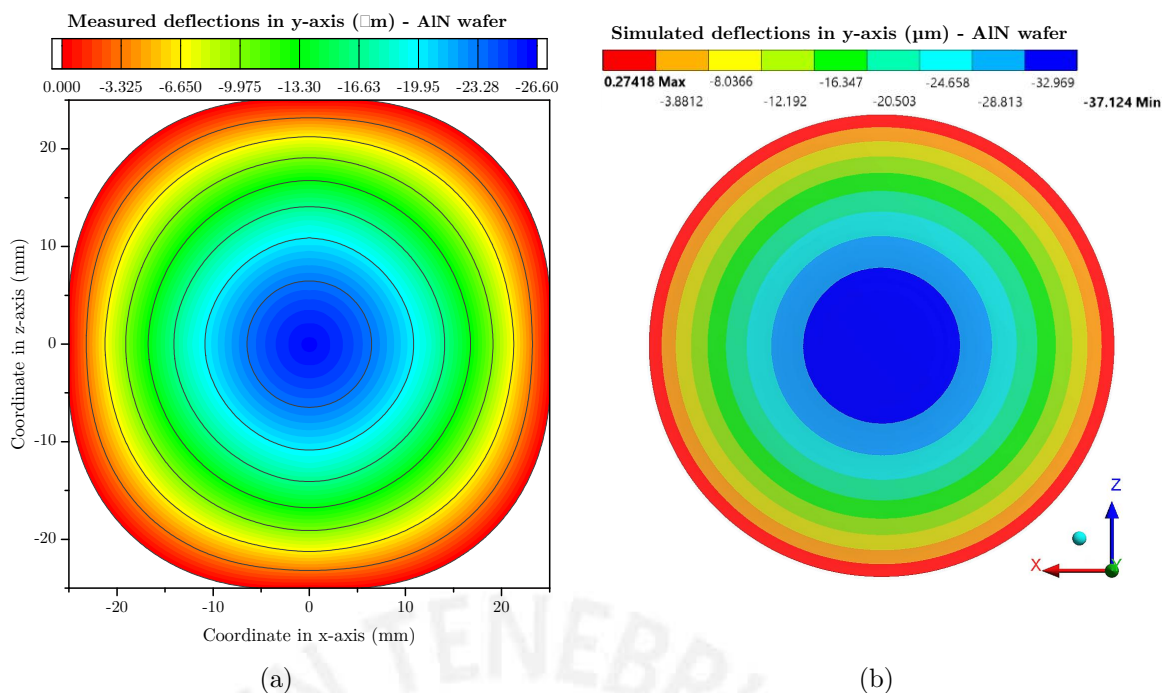


Figure 4.11.: Deflections in y-axis of the AlN wafers: (a) Measured data, (b) Simulated data.

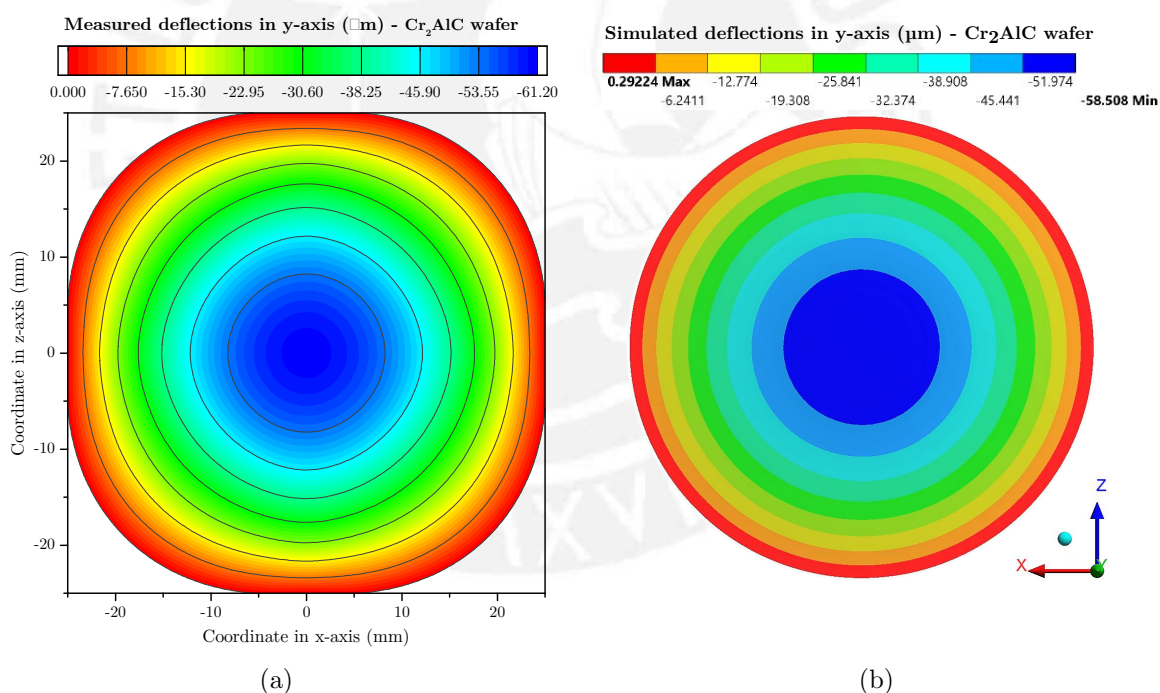


Figure 4.12.: Deflections in y-axis of the Cr_2AlC wafers: (a) Measured data, (b) Simulated data.

maximum value equal to $61.2\ \mu\text{m}$ in the deflection measurements (Figure 4.12a) and equal to $58.5\ \mu\text{m}$ in the simulation (Figure 4.12b). Based on the above mentioned, the

difference between the previous values indicates that the curvature radius of the wafer is lower than that of the simulations and therefore, the measured stresses in the Cr_2AlC wafer are higher than the simulated ones. This can also be seen in Figure 4.10, where the pale blue columns (measured stresses) are higher than the blue columns (simulated stresses).



Conclusions and Future Work

5.1. Conclusions

The simulation of the residual stresses in the AlN and Cr₂AlC wafers was accomplished. Three simulation types were developed in Ansys Workbench by including different features in each one. Simulation 1 represented mainly the thermal loads applied to the model as heating and cooling steps. Nevertheless, since the thin film body was active during the simulation, no residual stresses were generated once the model was cooled to room temperature. Therefore, simulation 2 included the birth and death technique with the aim of representing the thin film deposition by the activation of its model and thus, of its material properties.

On the other hand, the simulation 3 was based on a different approach by setting a pinball region as contact trigger. Even though the contact between the thin film and silicon dioxide layer was detected only when the bodies were brought together, the thermal load applied to the substrate was not transmitted to the thin film due the fixation of the contact surface during the heating process. As a result, low residual stress were generated in the thin film.

Furthermore, the simulation based on an axisymmetric geometric model enabled to visualize the residual stress distribution in the layers unlike the simulations based on quadrant solids. This can be used as a residual stress mapping, which permits to identify which layer is under a higher stress and to predict possible failure modes of the thin film. Besides, the simulations based on quadrant models generated outcomes close to the measurements and, especially, to that obtained with the Stoney equation. This was because unlike the axisymmetric simulations, the quadrant-based simulations included the anisotropic properties of the materials by considering a three-dimensional body.

Hence, the birth and death technique added to the simulations with the APDL commands permitted to activate or deactivate the thin film at the desired step according to the deposition process because the results were consistent with the measured values.

5.2. Future work

As has been mentioned in Chapter 3, the wafers are composed of multilayer thin films deposited over a substrate. Therefore, a simulation based on this multilayer structure represents a new challenge to face. For this case, a high computing power will be required in order to generate the mesh of these very thin bodies, with thicknesses around 2 nm, and thus, to simulate the residual stresses. Besides, the boundary conditions, meshing techniques as well as the birth and death commands considered in this work, can serve as input data for this simulation type.

Furthermore, with the aim of moving closer to the preparation processes, a transient simulation could be performed where the temperature curves over time, measured during the preparation of the wafers, can be included. This, in turn, enables to simulate over time and, as result, to have an enlarged view of the residual stresses generated during the entire preparation processes.

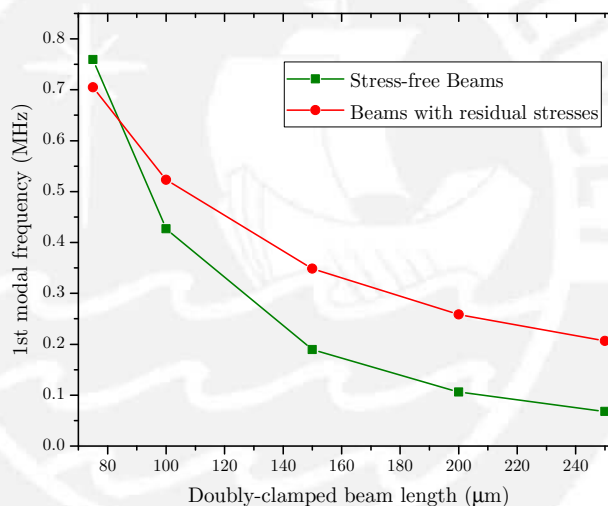


Figure 5.1.: Variation of the first modal frequency with regard to the doubly-clamped beam lengths. Green marks represent the results for stress-free beams, i.e. without residual stresses, while the red ones show the values for beams with residual stresses. The material of the beams were Cr_2AlC .

On the other hand, the impact of the residual stresses on the properties of the MEMS structures (cantilevers or doubly-clamped beams) could be obtained by applying the birth and death technique to a static or transient simulation based on the models of these structures. For instance, Figure 5.1 depicts the disruption of the first modal frequency of Cr_2AlC beams with residual stresses. These results were obtained with a simplified model, i.e. with a single-layer thin film and considering only the intermediate section without the lateral supports (see Figure 3.2). Hence, a more complex simulation would indicate whether a MEMS structure fits a specific application.

Aluminum nitride: Scans with altered data

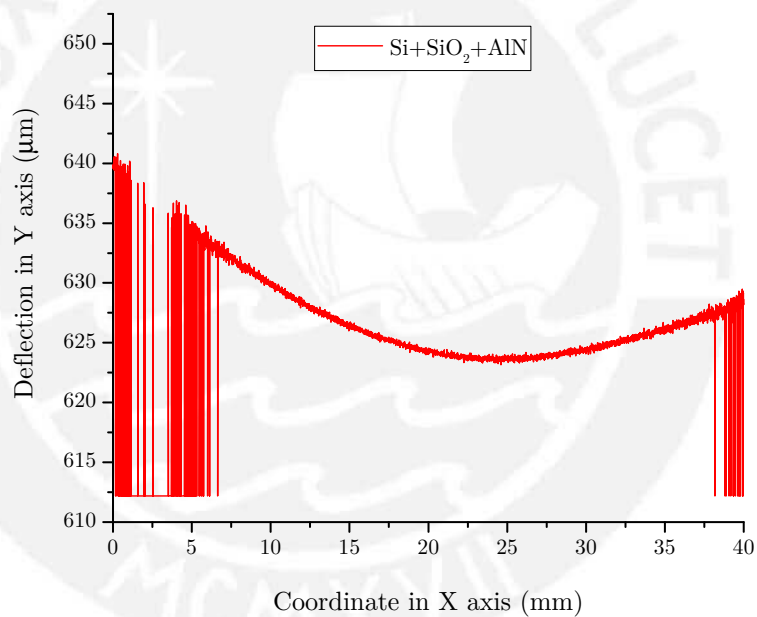


Figure A.1.: Deflection scans with wrong data. Data taken along x axis after AlN layer deposition.

As it can be seen in Figure A.1, the results presented two wrong data regions located on the left and the right. Hence, the data was split in order to capture the data without irregularities located in the middle. Then a regression fitting was applied to that data as follows:

$$\delta_y = -0.0001763x^3 + 0.03828x^2 - 1.578x + 642 \quad (\text{A.1})$$

where δ_y is the deflection in y axis (μm) and x is the coordinate in x axis (mm). The previous procedure was applied to the wrong data taken in the z axis scan, depicted in Figure A.2. The regression fitting for this data is the following:

$$\delta_y = 0.0001307z^3 + 0.01689z^2 - 0.125z + 620 \quad (\text{A.2})$$

where δ_y is the deflection in y axis (μm) and z is the coordinate in z axis (mm).

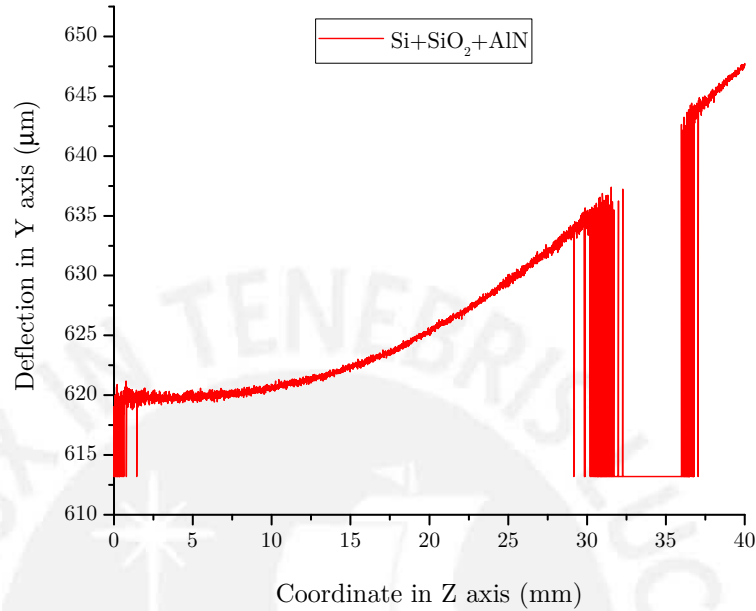


Figure A.2.: Deflection scans with wrong data. Data taken along z axis after AlN layer deposition.

Afterwards, the deflections corresponding to the coordinates in x and z axis of the wrong data were estimated by applying Equations A.1 and A.2. The results can be seen in Figures 4.1a and 4.1b.

Fitting equations

B.1. Aluminum nitride: Fitting equations

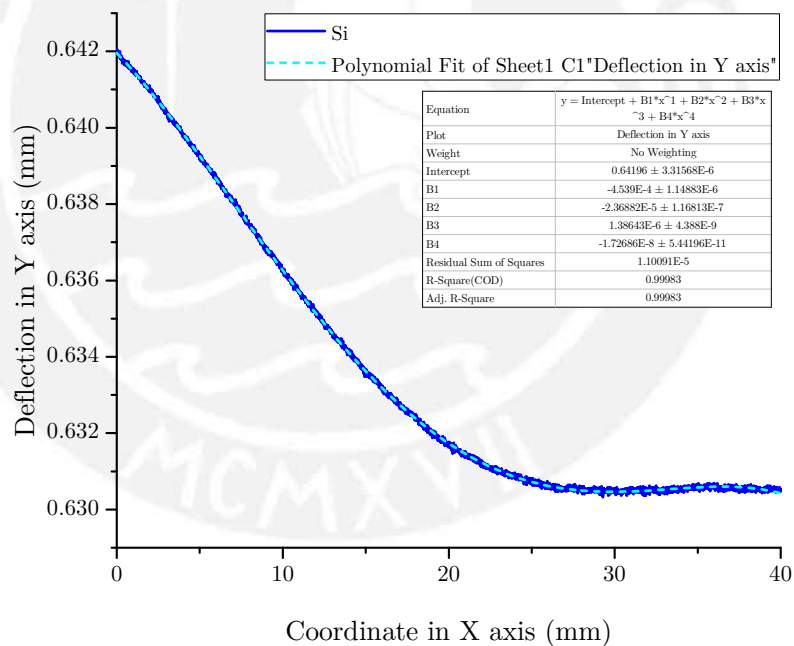


Figure B.1.: Data scan along x axis on the silicon substrate (blue line) and fourth order fitting polynomial (light blue dash-line). Polynomial parameters, R-squared and residual sum of squares shown in embedded table.

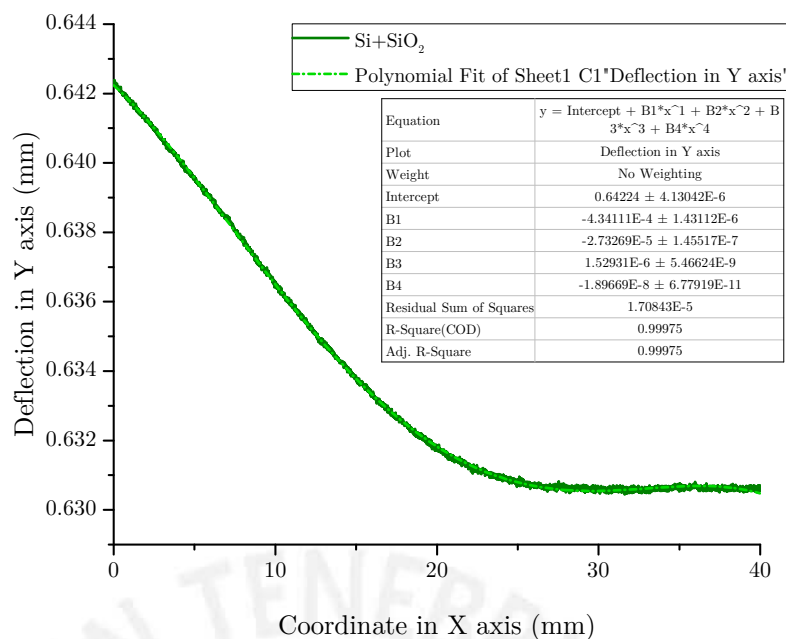


Figure B.2.: Data scan along x axis after the SiO₂ deposition (green line) and fourth order fitting polynomial (light blue dash-line). Polynomial parameters, R-squared and residual sum of squares shown in embedded table.

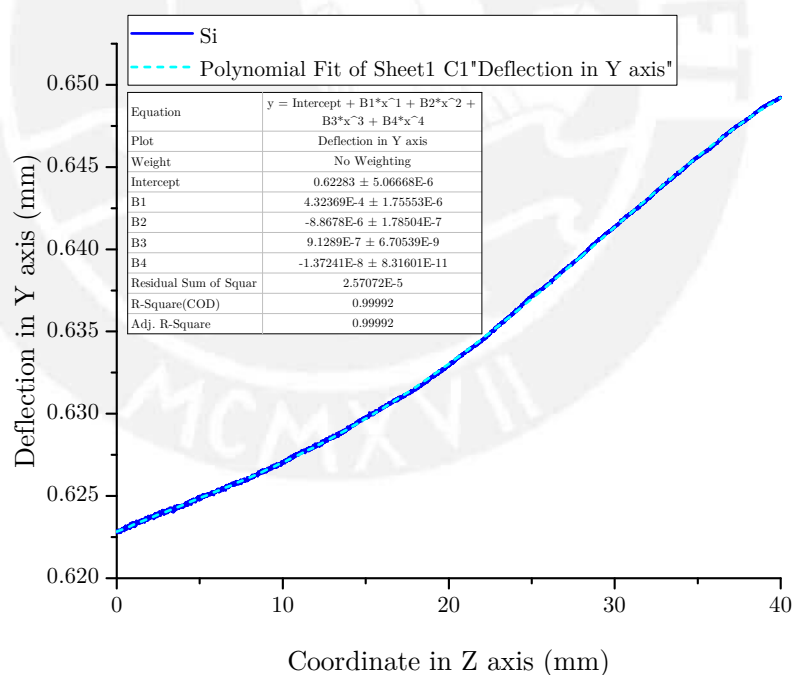


Figure B.3.: Data scan along z axis on the silicon substrate (blue line) and fourth order fitting polynomial (light blue dash-line). Polynomial parameters, R-squared and residual sum of squares shown in embedded table.

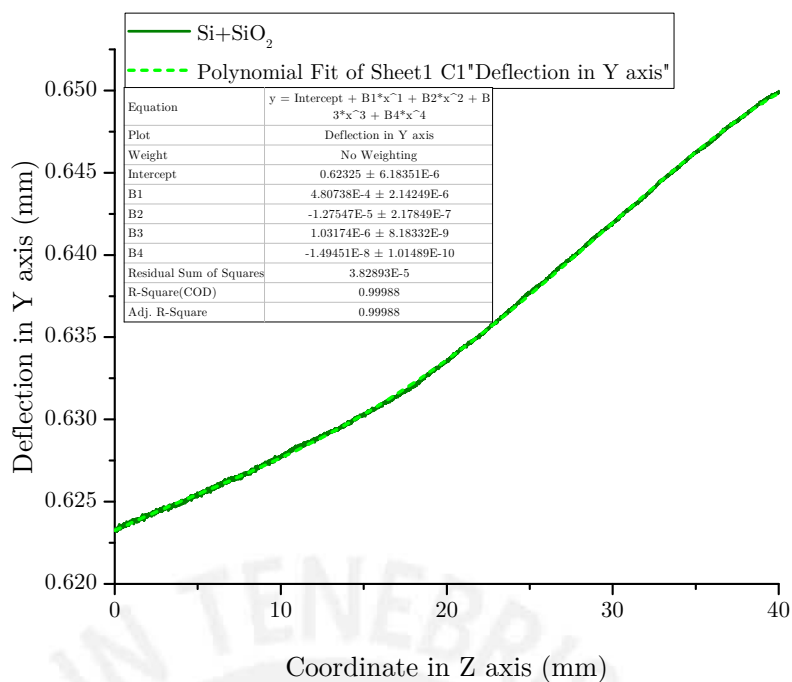


Figure B.4.: Data scan along z axis after the SiO₂ deposition (green line) and fourth order fitting polynomial (light blue dash-line). Polynomial parameters, R-squared and residual sum of squares shown in embedded table.

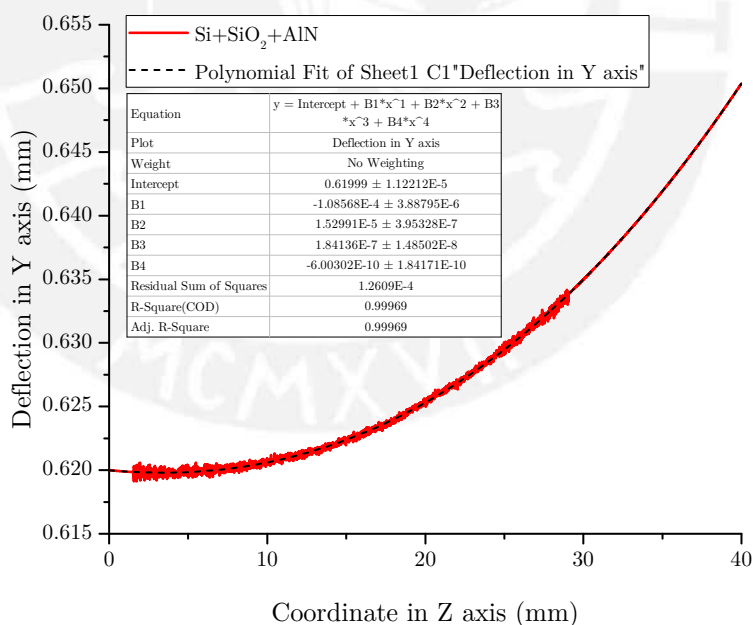


Figure B.5.: Data scan along z axis after the AlN deposition (red line) and fourth order fitting polynomial (black dash-line). Polynomial parameters, R-squared and residual sum of squares shown in embedded table.

B.2. Cr₂AlC phase: Fitting equations

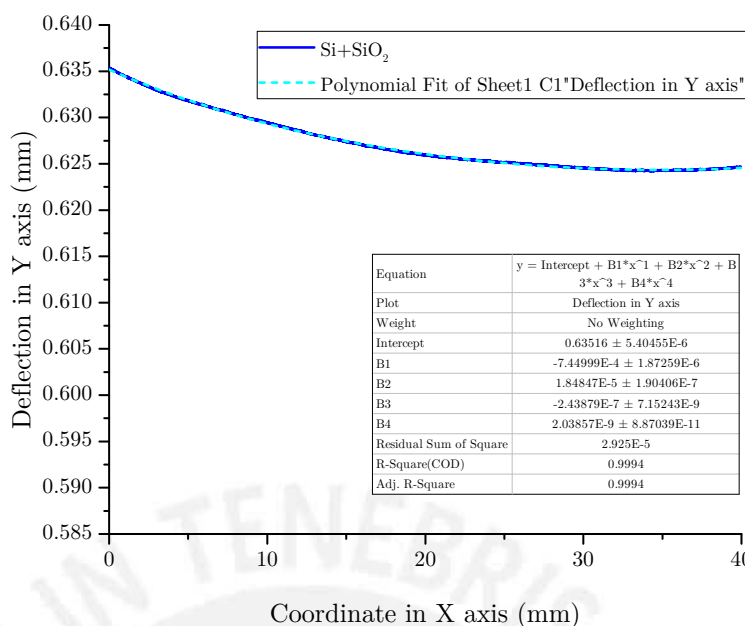


Figure B.6.: Data scan along x axis after the SiO₂ layer (blue line) and fourth order fitting polynomial (light blue dash-line). Polynomial parameters, R-squared and residual sum of squares shown in embedded table.

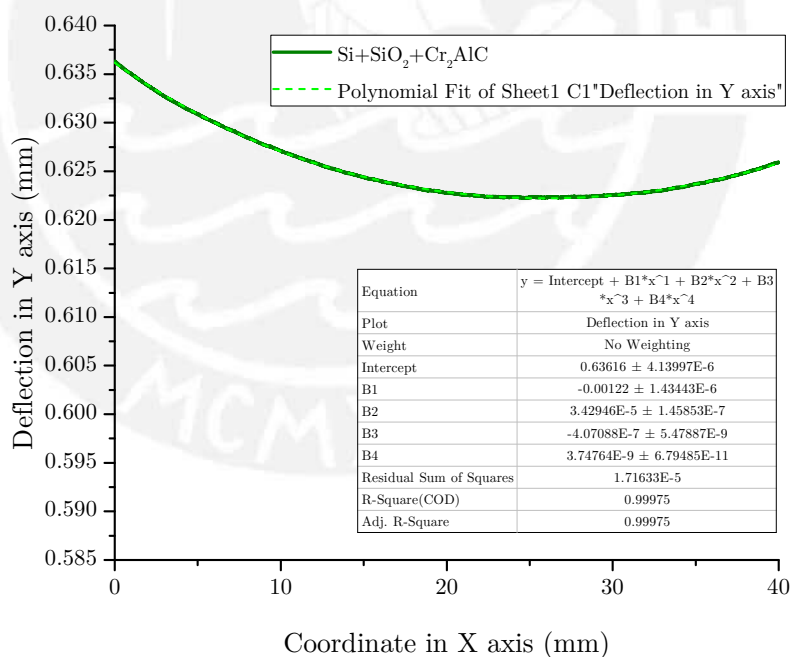


Figure B.7.: Data scan along x axis after the Cr₂AlC layer deposition (green line) and fourth order fitting polynomial (green blue dash-line). Polynomial parameters, R-squared and residual sum of squares shown in embedded table.

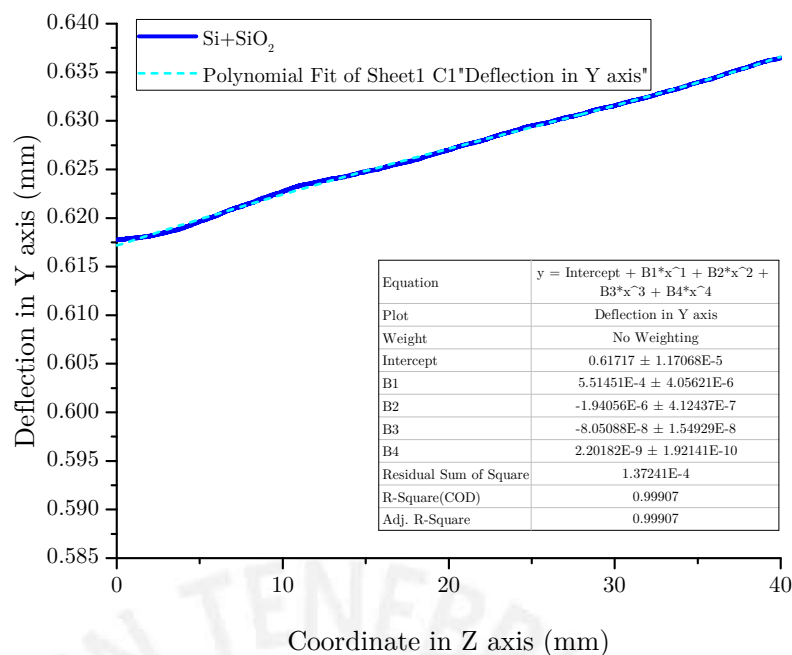


Figure B.8.: Data scan along z axis after the SiO₂ layer (blue line) and fourth order fitting polynomial (light blue dash-line). Polynomial parameters, R-squared and residual sum of squares shown in embedded table.

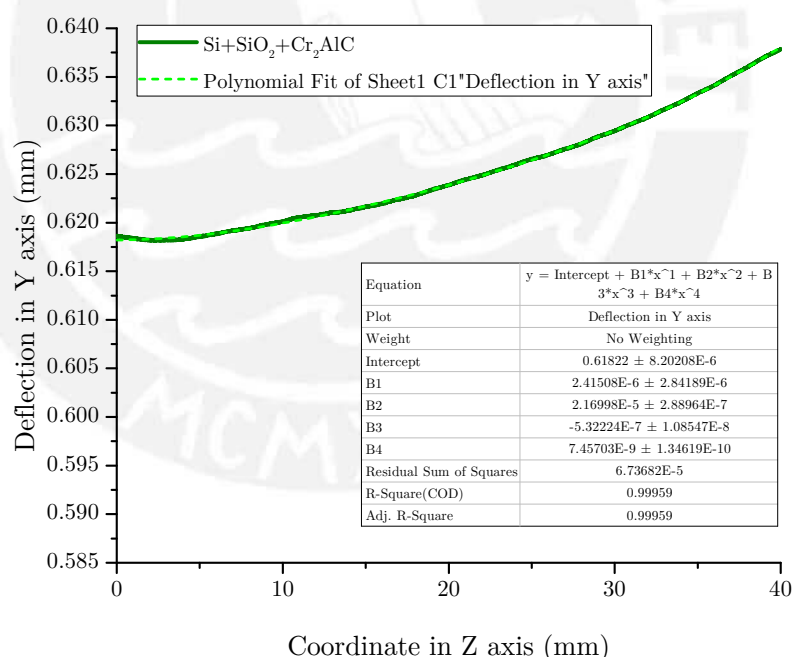


Figure B.9.: Data scan along z axis after the Cr₂AlC layer deposition (green line) and fourth order fitting polynomial (green blue dash-line). Polynomial parameters, R-squared and residual sum of squares shown in embedded table.

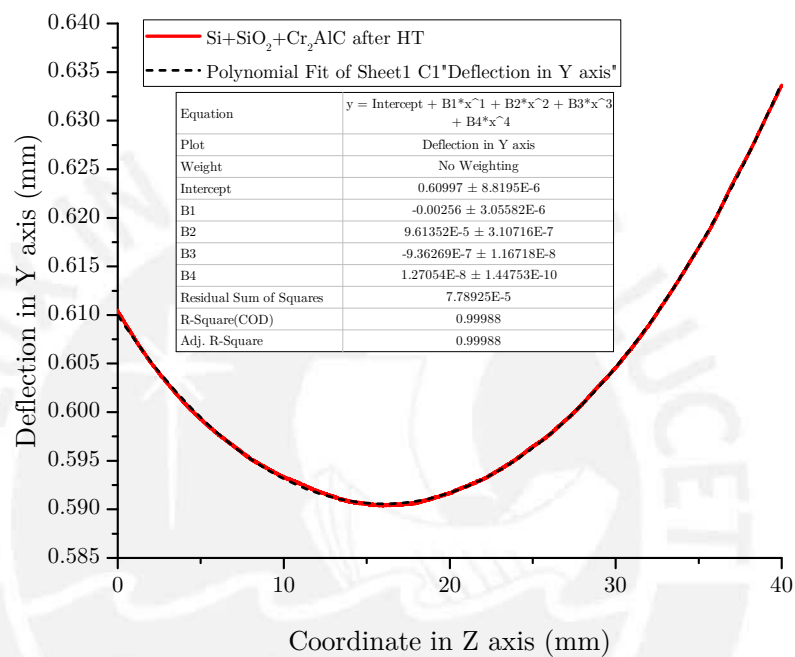


Figure B.10.: Data scan along z axis after the heat treatment once the Cr_2AlC layer was deposited (red line) and fourth order fitting polynomial (black dash-line). Polynomial parameters, R-squared and residual sum of squares shown in embedded table.

Bibliography

- [1] Loughborough University. *An Introduction to MEMS (Micro-electromechanical Systems)*. PRIME Faraday Partnership, 2002.
- [2] Carlos Báez, Mónico Linares, Alfonso Torres, and Wilfrido Calleja. Test structures for residual stress monitoring in the integrated CMOS-MEMS process development. *2016 13th International Conference on Synthesis, Modeling, Analysis and Simulation Methods and Applications to Circuit Design (SMACD)*, pages 1–4, 2016.
- [3] R. Anzalone, G. D’Arrigo, M. Camarda, C. Locke, S. E. Saddow, and F. La Via. Advanced residual stress analysis and FEM simulation on heteroepitaxial 3CSiC for MEMS application. *Journal of Microelectromechanical Systems*, 20(3):745–752, 2011.
- [4] Rolf Grieseler, Felix Theska, Thomas Stürzel, Bernd Hähnlein, Mike Stubenrauch, Marcus Hopfeld, Thomas Kups, Jörg Pezoldt, and Peter Schaaf. Elastic properties of nanolaminar Cr₂AlC films and beams determined by in-situ scanning electron microscope bending tests. *Thin Solid Films*, 604:85–89, 2016.
- [5] Neus Sabaté, Dietmar Vogel, Astrid Gollhardt, Jürgen Keller, Carles Cané, Isabel Gràcia, Joan R. Morante, and Bernd Michel. Residual stress measurement on a MEMS structure with high-spatial resolution. *Journal of Microelectromechanical Systems*, 16(2):365–372, 2007.
- [6] Per Eklund, Manfred Beckers, Ulf Jansson, Hans Högberg, and Lars Hultman. The MAX phases: Materials science and thin-film processing. *Thin Solid Films*, 518(8):1851–1878, 2010.
- [7] Michel W. Barsoum and Miladin Radovic. Elastic and Mechanical Properties of the MAX Phases. *Annual Review of Materials Research*, 41(1):195–227, 2011.
- [8] H. J. Yang, Y. T. Pei, G. M. Song, and J. Th. M. De Hosson. Healing performance of Ti₂AlC ceramic studied with in situ microcantilever bending. *Journal of the European Ceramic Society*, 33(2):383–391, 2013.

- [9] Michel W Barsoum and T El-Raghy. New Phases : Carbide and Nitride Materials Unique Ternary ceramics turn out to be surprisingly soft and machinable, yet also heat-tolerant, strong and lightweight. *American Scientist*, 89(4):334–343, 2001.
- [10] Michel W. Barsoum. *MAX Phases: Properties of Machinable Ternary Carbides and Nitrides*. Wiley-VCH Verlag GmbH & Co. KGaA, 2013.
- [11] M. Romero and R. Escamilla. First-principles calculations of structural, elastic and electronic properties of Nb₂SnC under pressure. *Computational Materials Science*, 55:142–146, 2012.
- [12] GuoZhu Jia and LiJun Yang. Ab initio calculations for properties of Ti₂AlN and Cr₂AlC. *Physica B: Condensed Matter*, 405(21):4561–4564, 2010.
- [13] M. F. Cover, O. Warschkow, M. M. M. Bilek, and D. R. McKenzie. A comprehensive survey of M₂AX phase elastic properties. *Journal of physics. Condensed matter : an Institute of Physics journal*, 21(30):305403, 2009.
- [14] T. H. Scabarozi, S. Amini, O. Leaffer, A. Ganguly, S. Gupta, W. Tambussi, S. Clipper, J. E. Spanier, M. W. Barsoum, J. D. Hettinger, and S. E. Lofland. Thermal expansion of select Mn+1AX_n(M=early transition metal, A=A group element, X=C or N) phases measured by high temperature x-ray diffraction and dilatometry. *Journal of Applied Physics*, 105(1):1–8, 2009.
- [15] A. G. Zhou, M. W. Barsoum, S. Basu, S. R. Kalidindi, and T. El-Raghy. Incipient and regular kink bands in fully dense and 10 vol.% porous Ti₂AlC. *Acta Materialia*, 54(6):1631–1639, 2006.
- [16] F. C. Frank and A. N. Stroh. On the Theory of Kinking. *Proceedings of the Physical Society. Section B*, 65(10):811, 1952.
- [17] William Callister and David Rethwisch. *Materials science and engineering: an introduction*, volume 94. John Wiley & Sons, Ltd, seventh edition, 2007.
- [18] Michel W. Barsoum. Physical Properties of the MAX Phases. *Encyclopedia of Materials: Science and Technology*, pages 1–11, 2004.
- [19] Wubian Tian, Peiling Wang, Guojun Zhang, Yanmei Kan, Yongxiang Li, and Dongsheng Yan. Synthesis and thermal and electrical properties of bulk Cr₂AlC. *Scripta Materialia*, 54(5):841–846, 2006.
- [20] Jiemin Wang, Jingyang Wang, Aijun Li, Jingjing Li, and Yanchun Zhou. Theoretical Study on the Mechanism of Anisotropic Thermal Properties of Ti₂AlC and Cr₂AlC. *J. Am. Ceram. Soc.*, 1208(33884):1202–1208, 2014.
- [21] W. B. Zhou, B. C. Mei, and J. Q. Zhu. On the synthesis and properties of bulk ternary Cr₂AlC ceramics. *Materials Science-Poland*, 27(4/1):973–981, 2009.
- [22] S. Saib and N. Bouarissa. Electronic properties and elastic constants of wurtzite, zinc-blende and rocksalt AlN. *Journal of Physics and Chemistry of Solids*, 67(8):1888–1892, 2006.
- [23] Hadis Morkoç. *Handbook of Nitride Semiconductors and Devices*, volume 1. Wiley-VCH Verlag GmbH & Co. KGaA, Weinheim, Germany, 2008.

- [24] Chin Yu Yeh, Z. W. Lu, S. Froyen, and Alex Zunger. Zinc-blende-wurtzite polytypism in semiconductors. *Physical Review B*, 46(16):10086–10097, 1992.
- [25] Fredrik Engelmark. *AlN and High-k Thin Films for IC and Electroacoustic Applications*. PhD thesis, Uppsala University, 2002.
- [26] Akhilesh Pandey, Shankar Dutta, Ravi Prakash, Sandeep Dalal, R. Raman, Ashok Kumar Kapoor, and Davinder Kaur. Growth and evolution of residual stress of AlN films on silicon (100) wafer. *Materials Science in Semiconductor Processing*, 52:16–23, 2016.
- [27] Alexandru Andrei, Katarzyna Krupa, Michal Jozwik, Patrick Delobelle, Laurent Hirsinger, Christophe Gorecki, Lukasz Nieradko, and Cathy Meunier. AlN as an actuation material for MEMS applications. The case of AlN driven multilayered cantilevers. *Sensors and Actuators, A: Physical*, 141(2):565–576, 2008.
- [28] Daithí de Faoite, David J. Browne, Franklin R. Chang-Díaz, and Kenneth T. Stanton. A review of the processing, composition, and temperature-dependent mechanical and thermal properties of dielectric technical ceramics. *Journal of Materials Science*, 47(10):4211–4235, 2012.
- [29] Nicolas C. Polfer, Philippe Dugourd, and Corey N. Stedwell. *Laser Photodissociation and Spectroscopy of Mass-separated Biomolecular Ions*, volume 83 of *Lecture Notes in Chemistry*. Springer International Publishing, Cham, 2013.
- [30] S. Maouhoub, Y. Aoura, and A. Mir. FEM simulation of AlN thin layers on diamond substrates for high frequency SAW devices. *Diamond and Related Materials*, 62:7–13, 2016.
- [31] Kazuo Tsubouchi and Nobuo Mikoshiba. Zero-Temperature-Coefficient SAW Devices on AlN Epitaxial Films. *1982 Ultrasonics Symposium*, pages 340–345, 1982.
- [32] Kyocera Corporation. Characteristics of Kyocera fine ceramics, 2016.
- [33] Robert R. Reeber and Kai Wang. Lattice Parameters and Thermal Expansion of Important Semiconductors and Their Substrates. *MRS Proceedings*, 622:T6.35.1, 2000.
- [34] Nadim Maluf and Kirt Williams. *An Introduction to Microelectromechanical Systems Engineering*. Artech House, Inc., second edition, 2004.
- [35] A. Goswami. *Thin Films Fundamentals*. New Age International, 1996.
- [36] Hans H. Gatzert, Volker Saile, and Jürg Leuthold. *Micro and Nano Fabrication*. Springer-Verlag Berlin Heidelberg, 2015.
- [37] Krishna Seshan. *Handbook of Thin Film Deposition Processes and Technologies*. Noyes Publications, Santa Clara, 2002.
- [38] Andrew H. Simon. *Sputter Processing*. Elsevier Inc., third edition, 2012.

- [39] Chun Zhao, Mohammad H Montaseri, Graham S. Wood, Suan Hui, Ashwin A. Seshia, and Michael Kraft. A review on coupled MEMS resonators for sensing applications utilizing mode localization. *Sensors and Actuators A: Physical*, 249:93–111, 2016.
- [40] Robin MH Islam. *Single and double clamped resonator sensors - Design , fabrication and testing*. Master's thesis, KTH Royal Institute of Technology, 2012.
- [41] Rolf Grieseler, Bernd Hähnlein, Mike Stubenrauch, Thomas Kups, Marcus Wilke, Marcus Hopfeld, Jörg Pezoldt, and Peter Schaaf. Nanostructured plasma etched, magnetron sputtered nanolaminar Cr₂AlC MAX phase thin films. *Applied Surface Science*, 292:997–1001, 2014.
- [42] Göran Stemme. Resonant silicon sensors. *Journal of Micromechanics and Microengineering*, 1(January 1999):113–125, 1999.
- [43] Jürgen Fritz. Cantilever biosensors. *Analyst*, 133(7):855–863, 2008.
- [44] O. A. Bauchau and J. I. Craig. *Structural Analysis*. Springer Netherlands, Dordrecht, 2009.
- [45] Bernd Hähnlein. *Resonatoren aus Gruppe III-Nitriden und ihren Mischkristallen*. Master thesis, Technische Universität Ilmenau, 2013.
- [46] Siebe Bouwstra and Bert Geijselaers. On the resonance frequencies of microbridges. *TRANSDUCERS '91: 1991 International Conference on Solid-State Sensors and Actuators. Digest of Technical Papers*, pages 538–542, 1991.
- [47] Klemens Brückner, Volker Cimalla, Florentina Niebelschütz, R. Stephan, Katja Tonisch, Oliver Ambacher, and Matthias A. Hein. Strain- and pressure-dependent RF response of microelectromechanical resonators for sensing applications. *Journal of Micromechanics and Microengineering*, 17(10):2016–2023, 2007.
- [48] Kuo-Shen Chen. Techniques in Residual Stress Measurement for MEMS and Their Applications. In Cornelius T. Leondes, editor, *MEMS/NEMS: Handbook Techniques and Applications*, pages 1252–1328. Springer US, Boston, MA, 2007.
- [49] L. Wang, Y. Wang, X. G. Sun, J. Q. He, Z. Y. Pan, and C. H. Wang. Finite element simulation of residual stress of double-ceramic-layer La₂Zr₂O₇/8YSZ thermal barrier coatings using birth and death element technique. *Computational Materials Science*, 53(1):117–127, 2012.
- [50] K. Malinauskas, V. Ostaševičius, R. Daukševičius, and V. Grigaliunas. Residual stress in a thin-film microoptoelectromechanical (MOEMS) membrane. *Mechanika*, 18(3):273–279, 2012.
- [51] H. J. Wang, H. A. Deng, S. Y. Chiang, Y. F. Su, and K. N. Chiang. Development of a process modeling for residual stress assessment of multilayer thin film structure. 584:146–153, 2015.
- [52] X. C. Zhang, B. S. Xu, H. D. Wang, and Y. X. Wu. An analytical model for predicting thermal residual stresses in multilayer coating systems. *Thin Solid Films*, 488(1-2):274–282, 2005.

- [53] Tsung Lin Chou, Shin Yueh Yang, and Kuo Ning Chiang. Overview and applicability of residual stress estimation of film-substrate structure. *Thin Solid Films*, 519(22):7883–7894, 2011.
- [54] C. Q. Guo, Z. L. Pei, D. Fan, R. D. Liu, J. Gong, and C. Sun. Predicting multilayer film's residual stress from its monolayers. *Materials and Design*, 110:858–864, 2016.
- [55] Chun Hway Hsueh. Modeling of elastic deformation of multilayers due to residual stresses and external bending. *Journal of Applied Physics*, 91(12):9652–9656, 2002.
- [56] Kuo-Shen Chen and Kuang-Shun Ou. MEMS Residual Stress Characterization. *Handbook of Silicon Based MEMS Materials and Technologies*, pages 398–412, 2015.
- [57] M.N. James. Residual Stress Influences in Mechanical Engineering. In *XVIII Congreso Nacional de Ingenieria Mecanica*, 2010.
- [58] P. Kesavan Nair and R. Vasudevan. Residual stresses of types II and III and their estimation. *Sadhana*, 20(1):39–52, feb 1995.
- [59] Lothar Spieß, Gerd Teichert, Robert Schwarzer, Herfried Behnken, and Christoph Genzel. *Moderne Röntgenbeugung*. Vieweg+Teubner, Wiesbaden, 2009.
- [60] Richard Budynas and J. Keith Nisbett. *Shigley's Mechanical Engineering Design*, volume New York. Mc Graw Hill, tenth edition, 2015.
- [61] Dimitrios G. Pavlou. *Essentials of the finite element method: for mechanical and structural engineers*. Academic Press, 2015.
- [62] Xiaolin Chen and Yijun Liu. *Finite element modeling and simulation with Ansys Workbench*. 2014.
- [63] ANSYS Inc. ANSYS Meshing User's Guide, 2013.
- [64] M. A. Nicolet. Diffusion barriers in thin films. *Thin Solid Films*, 52(3):415–443, 1978.
- [65] R. Grieseler, J. Klaus, M. Stubenrauch, K. Tonisch, S. Michael, J. Pezoldt, and P. Schaaf. Residual stress measurements and mechanical properties of AlN thin films as ultra-sensitive materials for nanoelectromechanical systems. *Philosophical Magazine*, 92(25-27):3392–3401, 2012.
- [66] Narottam P. Bansal and R. H. Doremus. *Handbook of Glass Properties*. Academic Press, Orlando, Florida, 1986.
- [67] ANSYS Inc. ANSYS Mechanical APDL Element Reference, 2013.
- [68] Y. X. Ou, J. Lin, S. Tong, W. D. Sproul, and M. K. Lei. Structure, adhesion and corrosion behavior of CrN/TiN superlattice coatings deposited by the combined deep oscillation magnetron sputtering and pulsed dc magnetron sputtering. *Surface and Coatings Technology*, 293:21–27, 2016.
- [69] Arun Augustin, K Rajendra Udupa, and Udaya Bhat K. Effect of Pre-Zinc Coating on the Properties and Structure of DC Magnetron Sputtered Copper Thin Film on Aluminium. *American Journal of Materials Science*, 5:58–61, 2015.

- [70] ANSYS Inc. ANSYS Mechanical User's Guide, 2013.
- [71] Milton Ohring. *Materials Science of Thin Films: Deposition and Structure*. Academic Press, second edition, 2002.
- [72] Mustafa Toparli, Faruk Sen, Osman Culha, and Erdal Celik. Thermal stress analysis of HVOF sprayed WC-Co/NiAl multilayer coatings on stainless steel substrate using finite element methods. *Journal of Materials Processing Technology*, 190(1-3):26–32, 2007.
- [73] Zhenghao Gan and Heong Wah Ng. Experiments and inelastic finite element analyses of plasma sprayed graded coatings under cyclic thermal shock. *Materials Science and Engineering A*, 385(1-2):314–324, 2004.
- [74] K.A Khor and Y.W Gu. Effects of residual stress on the performance of plasma sprayed functionally graded ZrO₂/NiCoCrAlY coatings. *Materials Science and Engineering: A*, 277(1-2):64–76, 2000.
- [75] Erdogan Madenci and Ibrahim Guven. *The Finite Element Method and Applications in Engineering Using ANSYS®*. Springer US, Boston, MA, second edition, 2015.
- [76] ANSYS Inc. Lecture 3 - Introduction to contact. ANSYS Mechanical structural nonlinearities, 2010.
- [77] James Stewart. *Calculus: Early transcendentals*. Cengage Learning, eighth edition, 2016.

